# PERFORMANCE OPTIMIZATION OF ORGANIC SOLAR CELLS BY SIMULATION AND CHARACTERIZATION

by

**Liming Liu**

B.S. in Physics, Wuhan University, 2002

M.S in Physics, University of Pittsburgh, 2007

Submitted to the Graduate Faculty of

Swanson School of Engineering in partial fulfillment

of the requirements for the degree of

Doctor of Philosophy

University of Pittsburgh

2011

UNIVERSITY OF PITTSBURGH

SWANSON SCHOOL OF ENGINEERING

This dissertation was presented

by

Liming Liu

It was defended on

March 28th, 2011

and approved by

William E Stanchina, Professor, Department of Electrical and Computer Engineering, University of Pittsburgh

Hong Koo Kim, Professor, Department of Electrical and Computer Engineering, University of Pittsburgh

Mahmoud EI Nokali, Associate Professor, Department of Electrical and Computer Engineering, University of Pittsburgh

Yi Luo, Assistant Professor, Department of Electrical and Computer Engineering, Carnegie Mellon University

Dissertation Director: Guangyong Li, Assistant Professor, Department of Electrical and Computer Engineering, University of Pittsburgh

**PERFORMANCE OPTIMIZATION OF ORGANIC SOLAR CELLS BY SIMULATION AND CHARACTERIZATION**

Liming Liu, PhD

University of Pittsburgh, 2011

Compared with silicon based solar cells, organic solar cells (OSCs) are less expensive alternatives because the thin and flexible OSCs can be easily fabricated onto the substrate by roll to roll painting. The current power conversion efficiency (PCE) of OSCs is about 8%. For commercialization of OSCs, a reasonable PCE (10%), at which those devices could generate electricity at a comparable cost to that of silicon based solar cells, is required. This requirement is the major driving force of this Ph.D. thesis to optimize OSCs with high PCE.

To optimize the performance of OSCs, guidance from theoretical and simulation studies will play a key role. After solving coupled Poisson and Continuity equations, we first developed a macroscopic simulation tool which can precisely describe the current-voltage (*J*-*V*) characteristics of organic solar cells under known conditions such as device physical dimension (device layer thickness), physical parameters (absorption, carrier mobility), carrier generation/recombination kinetics, and boundary conditions. With this macroscopic simulation tool, the loss mechanism in BHJ OSCs is first investigated by fitting the simulated intensity dependent current-voltage (*J*-*V*) curves to experimental measurements. It is found that monomolecular recombination is dominant. Then, we have used the simulation tool to investigate performance optimization regarding thickness optimization, lowering bandgap of conjugated polymer, and balancing carrier transport in OSCs.

For the characterization, single-walled carbon nanotubes (SWCNTs) were introduced in OSCs to increase the carrier mobility. It is observed that the performance of the device increased with small amount of SWCNTs but decreased if large amount of SWCNTs were introduced. The effects of semiconducting and metallic SWCNTs were explored by *J-V* characterization. It is found that semiconducting SWCNTs benefit the transport of photoexcited carrier while metallic SWCNTs introduce severe bimolecular recombination. Moreover, Kelvin Probe Force Microscopy is utilized to locally investigate the electrical role of SWCNTs in OSCs. The observation indicates that SWCNTs work as donor materials to transport holes.

The simulation and characterization studies not only provide fundamental understanding on the physics of OSCs but also offer a feasible way to further optimize their performance.

## TABLE OF CONTENTS

## LIST OF TABLES

## LIST OF FIGURES

# PREFACE

This thesis would not have been possible without the generous support, helpful guidance and constructive suggestions from many people. First and foremost, I would like to express my deepest gratitude to my mentor, Professor Guangyong Li, for his guidance which helped me becoming an electrical engineer. I am obliged to Dr. Li for his thoughtful guidance, encouragement and patience throughout my doctoral program. I sincerely appreciate Professor William. E. Stanchina, Professor Hong Koo Kim, Professor Mahmound EI.Nokali, and Professor Yi Luo for serving on my committee. The committee members' fruitful discussion and enormous efforts improve the quality of this dissertation a lot.

I thank my friends and colleagues for the help and companionship during both academic research and personal life. Special thanks go to Di Xu, Fei Yan, Yonggang Xi, Yue Ke, Baojun Liu, Yushi Hu, Dongxiao Li, Tong Chen, and Qingqing Wang. I really appreciate Yucai Wang, a master student in Dr.Li's group, for his generous training of atomic force microscopy. I wish all my friends would have a brilliant future.

Finally, I especially thank my wife, Zheng Li, who have always trusted and supported me during my doctoral period in USA. I am glad that I make you proud.

# 1.0 INTRODUCTION

As the global energy demand continues to increase every year, it is indispensable to explore renewable energy sources because of the limited supply of today's main energy sources (i.e. oil, coal, natural gas and uranium) and their long-term detrimental effects on the natural balance on our planet. Today's plants are unable to absorb the huge amount of extra carbon dioxide which is released in the atmosphere mainly by burning of fossil fuel. The increased concentration of carbon dioxide in the atmosphere adds to the greenhouse effect, which will increase the global average surface temperature. The consequence of these changes is already seen by an increase in the frequent and severe natural disasters [1]. Comparing with fossil fuel, solar energy is clean, renewable and sustainable, helping to protect our environment. Therefore, harvesting energy directly from the sunlight by photovoltaic (PV) technology is being widely recognized as an essential component of energy production in the future [2]. Figure 1.1 is schematic diagram of solar-electric system based on silicon solar cells.

A solar cell is a device that converts solar energy into electricity by the PV effect. The PV effect was first recognized in 1839 by French physicist A. E. Becquerel [3]. However, the PV cells have not been extensively studied until 1954 when Bell Laboratories, experimenting with semiconductors, accidentally found that silicon doped with certain impurities was very sensitive to the light. The first silicon based solar cell made in Bell Laboratories had a power

conversion efficiency (PCE) of 6% [4]. Since then, PCE has reached 24% for crystalline silicon solar cell [5], which is close to the theoretical upper limit of 30% [6]. Nowadays, people are trying to fabricate solar cell using amorphous silicon, which is much cheaper than crystal ones. However, crystalline silicon solar cells are still by far the most dominant PVs because of the poor PCE of amorphous silicon (below 10% [7]) and short life time.

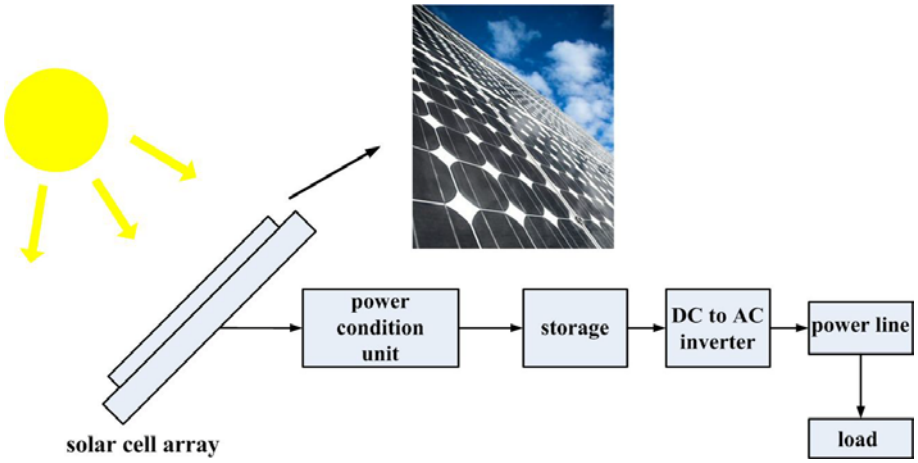


**Figure 1.1** The components of PV solar-electric system.

The inorganic solar cell material is not limited to silicon. For spacecraft application, Gallium arsenide (GaAs) is often used to achieve higher PCE (more than 30%) [8]. There are several advantages of GaAs solar cells compared with silicon-based ones: First, the absorption spectrum of GaAs matches solar spectrum better than that of silicon. Theoretical studies show that the optimal band gap to match the solar spectrum is 1.4eV [9] and the band gap for silicon and GaAs is 1.12eV and 1.42eV respectively at room temperature. Second, the carrier mobility in GaAs is much faster than in silicon. GaAs based solar cells are expected to exhibit low recombination loss. Moreover, GaAs is direct band gap material, which absorbs and emits light more efficiently than silicon, an indirect band gap material. However, the high

cost of the material and fabrication is the major disadvantage of GaAs PVs, which limits its application mainly in aerospace engineering and other fields with critical needs.

Although the production of PV modules is increased steadily by an annual average of 40%, the semiconductor PV still accounts for less than 1% of the total world energy production. One major obstacle for the market implementation is the expensive production costs for silicon based technology. The present cost of electricity from PV installations is about an order of magnitude higher than the current commercial price of electricity generated by fossil fuels or coals [10]. Therefore, the development of new materials and device structures, which can reduce the PV cost, are urgent in order to use the sustainable, environment-friendly energy source—solar energy.

## 1.1 ORGANIC SOLAR CELLS

Compared with inorganic materials such as silicon in the commercial market, organic solar cells (OSCs) are a less expensive alternative because they have extremely high optical absorption coefficients, offering the possibility for the production of very thin solar cells (for 600nm illumination wavelength, the absorption length of Si is ~10um, but for organic materials, the absorption length can be as short as several hundred nanometer [2]). Additional attractive features of OSCs are the possibilities for thin flexible devices which can be fabricated by high-throughput, low-cost approaches such as roll to roll painting, simple brush and ink jet method, compared with complicated procedures such as high vacuum CVD and

ion implantation for the fabrication of silicon based solar cells [11-13]. Silicon based solar cell with large area is always limited by the commercial available wafer size.

The first investigation of organic PVs dates back to 1959 when Kallman and Pope made an OSC using anthracene single crystal, which produced only 0.2 volts open circuit voltage ($V_{oc}$) with extremely low PCE about $2x10^{-4}$% [14]. Since then, twenty years of investigation on OSCs has shown that the typical PCE for single junction configuration is less than 0.1%, making it useless for commercial application. The major breakthrough in OSCs was achieved in 1986 by Tang, who increased PCE up to 1% by introducing donor-acceptor bi-layer configuration [15]. Although the built-in potential at the interface between donor and acceptor materials separates excitons more efficiently compared with the organic /metal interface in single layer devices, the exciton dissociation efficiency is still very low in bi-layer configuration, because the exciton diffusion length (10nm) is much shorter than the thickness of the film. The milestone in organic PVs came in 1995 with the introduction of bulk heterojunction (BHJ), where the donor and acceptor materials are blended together to maximize the interfacial area between them [16]. After some techniques to optimize the nanomorphology of the active layer, such as carefully choosing solvent, thermal annealing treatment, and slow drying of the active layer (solvent annealing) after it is spun on the substrate, the PCE has been increased up to 5% [17, 18]. Tandem configuration was utilized to increase light absorption, in which two solar cells with different absorption spectrum are stuck together by a transparent layer of titanium oxide ($TiO_x$). PCE of such tandem OSCs has increased up to 6% by Tim in 2007 [19]. Moreover, chemists also tried to synthesize novel organic materials with proper energy band structure, such as: 1. increase the difference

between Highest Occupied Molecular Orbital (HOMO) of donor and Lowest Unoccupied Molecular Orbital (LUMO) of acceptor to increase $V_{oc}$ [20]; 2. lower the band gap of conjugated polymer to enhance the light absorption and thus increase the short circuit current ($J_{sc}$) [21].

### 1.1.1 Conjugated Polymer

Since Shirakawa, MacDiarmid, and Heeger demonstrated in 1977 that the conductivity of conjugated polymers can be controlled by doping, a new field has emerged [22]. They were rewarded for their discovery with chemistry Nobel Prize in 2000. These conjugated polymers have been successfully used in organic light-emitting diodes (OLEDs) [23] and OSCs [15, 16]. Although the ordinary polymer is insulator, the conjugated polymer (also called conductive polymer) is electrical conducting. The electronic structure of organic semiconductors is based on conjugated π-electrons (sp2 hybridized). A conjugated organic system is made of an alternation between single and double carbon-carbon bonds as shown in Figure 1.2. Single bonds are known as σ-bonds and are associated with localized electrons, and double bonds contain a σ-bond and a π-bond. The π-electrons are much more mobile than the σ-electrons; they can jump from site to site between carbon atoms due to the mutual overlap of π-orbital along the conjugation path. The π-bands are either filled with electrons (HOMO, similar to the valence band in solid state semiconductor) or empty (LUMO, similar to the conduction band). This π-electron system has all the essential electronic features of organic materials: light absorption and emission, charge generation and transport. Figure 1.3 shows several examples of conjugated organic materials.

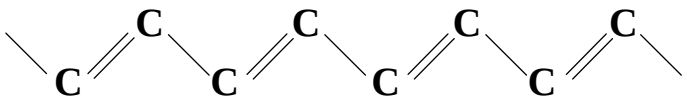

**Figure 1.2** In the conjugated polymer, the bonds between adjacent carbon atoms are alternatively single (σ-bonds) and double (π-bond).

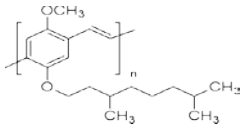

**MDMO-PPV**

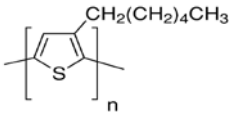

**P3HT**

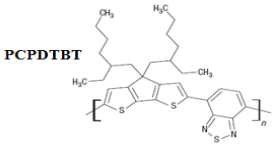


**PCPDTBT**

**Figure 1.3** The chemical structures of three conjugated polymers: Poly[2-methoxy-5-(3',7'-dimethyloctyloxy)-1,4-phenylenevinylene] (MDMO-PPV), Poly(3-hexylthiophene-2,5-diyl) (P3HT), and Poly[2,6-(4,4-bis-(2-ethylhexyl)-4H-cyclopenta[2,1-b;3,4-b']-dithiophene)-alt-4,7-(2,1,3-benzothiadiazole)] (PCPDTBT).

### 1.1.2 Bulk Heterojunction Configuration

The donor/acceptor bi-layer configuration of silicon based PV only has single junction between p doping and n doping materials. The configuration of single junction in OSCs leads to low PCE (no more than 1%) [15]. Instead of free electron and holes as in the solid state materials, tightly bound electron-hole pairs (exciton) present in the organic material due to its low dielectric constant [24]. The properties of the exciton in the inorganic and organic materials are compared in Table 1.1.

**Table 1.1** Exciton binding energy in the inorganic and organic materials.

| | Dielectric constant | Binding energy | Separation method | configuration |
|---|---|---|---|---|
| **Inorganic** | **High**<br>Si---11<br>GaAs--13 | **Low**<br>Si---10mev<br>GaAs--4mev | Thermal energy<br>26mev@RT | **Bi-layer** |
| **Organic** | **Low**<br>~2 to 3 | **High**<br>0.2 to 0.6ev | Thermal energy is **not** enough!<br>Built-in potential | **BHJ** |

In order to convert the solar energy to electricity, exciton must be separated to free carriers (electrons and holes) before they can be extracted by the external circuit. The exciton can only be separated to free electron and hole at the interface between the donor and acceptor materials by the built-in potential, arising from the offset of Fermi level between donor and acceptor materials. Unfortunately, the diffusion length of the exciton (after traveling the diffusion length, excitons will recombine or decay very quickly) is only about 10nm, which makes the exciton dissociation very inefficient in bi-layer configuration. As shown in Figure 1.4, the distance between the exciton excited by photon 1 and the interface of donor/acceptor is less than 10nm [2] and hence this exciton is able to be dissociated to free electron and hole with the help of built-in potential at the interface. But for the exciton excited by photon 2, it is too far to reach the interface before it recombined. Instead of converting photon energy to electric ones, the recombination of excitons transfers the photon energy to phonon or heating(as shown by a symbol of crossing), which is useless for the application of solar cells [25]. Considering the absorption length of the ordinary organic materials is about several hundred nanometers, the thickness of OSCs is also about several hundred nanometers to sufficiently absorb the light. In the single junction configuration, no

more than 5% exciton will be dissociated [25]. In another word, only 5% absorbed energy will contribute to the electric energy assuming all the free carriers are extracted by the external circuit. Therefore, the single junction configuration is not proper for OSCs due to the inefficient exciton dissociation.

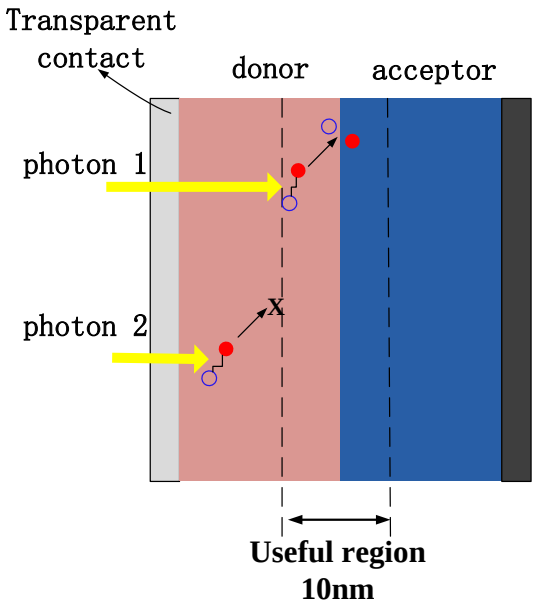


**Figure 1.4** Schematic diagram to show the inefficient exciton separation for bi-layer configuration in OSCs.

The revolutionary improvement in organic PVs came in the mid 1990s with the introduction of bulk heterojunction [16], where donor and acceptor materials are blended together. If the length scale of the blend is similar to the exciton diffusion length, the exciton decay process (as indicated by photon 2 in Figure 1.4) is significantly reduced because there exists enough interface in the proximity of every generated exciton, which facilitates the separation of the exciton. The BHJ configuration improved PCE up to 5% by some post-product treatment to improve the morphology of the thin film [17, 18]. In the following, BHJ configuration is used for all the OSCs.

### 1.1.3 Carrier Transport in BHJ OSCs

In order to optimize the performance of OSCs, it is imperative to investigate the work principle and factors limiting the performance of OSCs. For example, recombination loss plays a very important role in OSCs because the carrier mobility is so slow that photoexcited carriers can not be fully extracted by the external circuit. Up to now, to our knowledge, the fully exact understanding of how OSCs work is not clear.

However, there are several main procedures in the operation of OSCs as in Figure 1.5. The light passed through the transparent electrode (ITO) and excited the electron in conjugated polymer from HOMO to LUMO, leaving a hole in the LUMO as indicated in Figure 1.5a. For the light absorption, the more overlap between absorption spectrum of the conjugated polymer and solar spectrum, the more solar energy will be absorbed. The optimal band gap for the solar cell materials is about 1.4V. Unfortunately, the band gap of the ordinary conjugated polymer is about 2 V [21], which limits the efficiency of OSCs. Therefore, some research groups in material science tried to lower the band gap of conjugated polymer to increase the light absorption in OSCs [20, 21]. Theoretically, semiconductor materials with smaller band gap will absorb more solar energy considering all the photon with the energy bigger than the band gap will excite the electron from valence band (or HOMO) to conductive band (or LUMO). The reason for the optimal band (~1.4eV) is that there is a tradeoff between the absorption energy and $V_{oc}$. To be specified, the semiconductor material I with band gap of 0.5eV will absorb more energy than the material II with 1.5eV band gap because the photon with the energy range from 0.5eV to 1.5eV will be absorbed by

material I but not by II. On the other hand, materials II will have higher $V_{oc}$ due to its higher band gap. It is well known that PCE depends not only on $J_{sc}$ (higher absorption of photon results in higher $J_{sc}$), but also on $V_{oc}$ (generally, higher band gap results in higher $V_{oc}$). For the same material, the thicker the active layer, the more energy will be absorbed given the thickness of active layer is smaller than the absorption length and recombination (loss) is same for the thin and thick devices. But it is not always true that the device with thicker active layer results in high PCE. This issue will be discussed later.

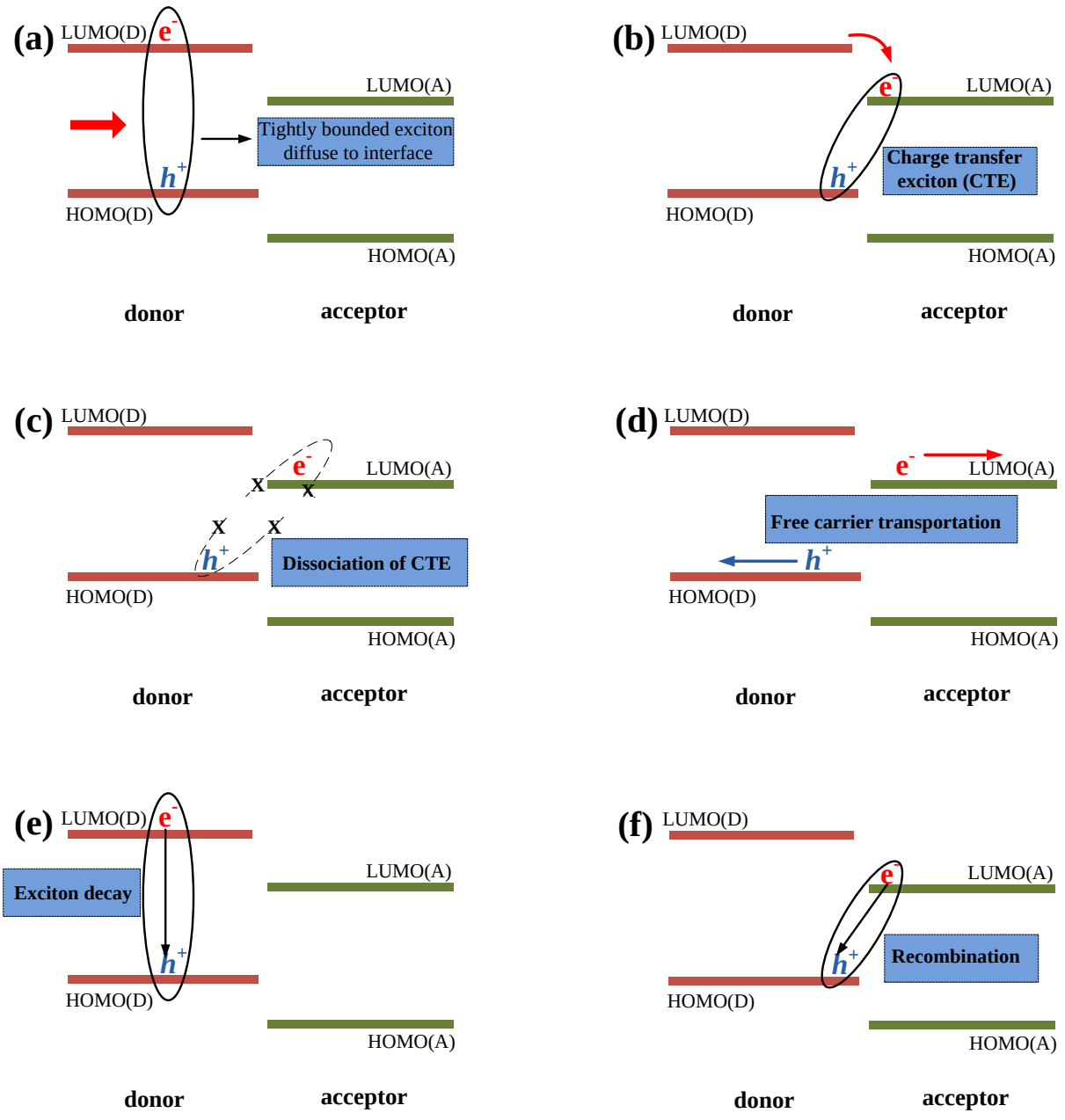


**Figure 1.5** Schematic diagram to show the basic work principle of OSCs (a-d) and the possible recombination mechanisms (e-f).

Figure 1.5b-c shows free charge carrier generation. After light absorption in the active layer (photoexcitation), instead of free electron and hole, tightly bounded exciton is created as shown in Figure 1.5a. Free charge carriers must be created by splitting the exciton into free electron and hole in order to be extracted by external circuit. The diffusion length of exciton

is about 10nm. In bipolar heterojunction configuration, splitting of exciton is inefficient because only the exciton near the interface can be separated. This problem has been tackled by BHJ configuration in which the donor and acceptor materials are blended together to increase the interface area.

Figure 1.5d shows that free carriers are transported through their respective phases to the electrodes in order to be extracted.

Figure 1.5e-f shows two possible loss mechanisms. Figure 1.5e demonstrates exciton decay which has been overcome by the concept of BHJ. Figure 1.5f describes recombination loss during free carrier extraction. The recombination of free charge carriers arise from the low mobility of carriers in OSCs, especially in the configuration of BHJ. For solid state materials with the symmetric structure, by Bloch theorem and Schrödinger equation, it is found that the electron is delocalized which means it is not able to tell which electron is belong to some certain atom. Therefore, the mobility is relatively high in solid state materials. But for organic materials, due to its disordered structure, instead of delocalized state, localized states are formed and charge carriers can only “jump” from one state to another, which is called hopping. The mobility of hopping mechanism is much lower because “jump” is much more difficult compared with “swimming” in the “electron sea” for solid state materials. For example, the carrier mobility in silicon is on the order of $10^{2}$ $cm^{2}$ $V^{-1}s^{-1}$ depending on the doping; while for the organic conjugated polymer, the mobility is on the order of $10^{-3}$ $cm^{2}$ $V^{-1}s^{-1}$ [26]. Due to the low mobility, free carriers can not totally be extracted by the external circuit, which increases the possibility of carrier recombination.

Configuration of BHJ increased the degree of disorder in the organic materials and it makes the carrier transport more difficult even compared with OSCs of single junction.

The recombination mechanism is strongly related to the basic processes of the carrier transport in OSCs as discussed above. There are primarily two kinds of recombination during transport of free electrons and holes: bimolecular recombination due to intermixing of donor/acceptor in nanometer scale for BHJ configuration and monomolecular recombination caused by defects and trapping in disordered organic materials. Determination of dominant recombination in BHJ OSCs is crucial to simulate the performance and further optimize the performance of OSCs. This issue will be discussed in Chapter 3.

## 1.2 MOTIVATION

Although promising progress has been seen in the last decade, OSCs are still not commercially viable due to the low efficiency. OSCs can only be widely used if reasonable PCE (more than 10%) is achieved such that those devices could generate electricity at a lower cost compared with crystalline silicon solar cells [27]. A recent study reported an internal quantum efficiency approaching 100% in OSCs under optimal conditions [28]. This observation implies that there is no fundamental limit to prevent the carrier collection and there is still plenty of room to optimize the performance of OSCs.

However, it is not easy to experimentally optimize the performance of OSCs. Because of their unique properties, parameters of OSCs are always correlated to each other. Therefore,

there are many parameters/factors need to be balanced and optimized to get the best performance as discussed below.

- The thickness of active layer: Because of the slow carrier mobility in the disordered organic materials, the thickness of active layer should be as thin as possible to prevent significant recombination loss. However, the device with the thin layer will result in insufficient light absorption. Therefore, the thickness of the active layer needs to be carefully optimized.
- Nanomorphology of BHJ configuration: The nanoscale morphology of the active layer has to be optimized such that there is enough interface area to separate the tightly bounded excitons while at the same time, enough interconnection pathways should be guaranteed to extract charge carriers.
- Weight ratio between donor (absorber) and acceptor materials: Too little donor material leads to insufficient light absorption. On the other hand, too little acceptor material will result in reduced interface area and hence the inefficient exciton dissociation.
- Electron and hole mobility: The electron and hole mobility also need to be balanced to prevent charge space limitation, where one kind of carriers has much higher mobility than the others.

Because of the complexity of OSCs as discussed above, it is not possible to simply tune one or a few parameters to achieve optimal performance. Instead, the optimization of OSCs is a fine balancing art. Therefore, in this Ph.D dissertation, we are trying to optimize the performance of OSCs by simulation and characterization. It is expected that the

simulation and characterization are able to provide the feasible method to improve the performance of OSCs and eventually to make them commercialized in the near future.

## 1.3 THESIS OUTLINE

In Chapter 2, we have discussed the modeling and simulation method for BHJ OSCs by numerically solving the coupled Poisson and continuity equations, which can precisely describe the performance of OSCs.

The recombination loss mechanism is investigated in Chapter 3 by simulating the intensity dependent *J-V* curves of OSCs. It is found that Langevin bimolecular recombination rate is **not** proper to describe BHJ OSCs and monomolecular recombination dominates their performance.

After developing the simulation tool (Chapter 2) and determining the dominant loss mechanism (Chapter 3), we have investigated several possible methods to optimize the performance of OSCs by the simulation in Chapter 4. Because of slow carrier mobility in the disordered organic materials, there exists a balance between light absorption and extraction of photoexcited carriers. Therefore, the thickness of active layer needs to be optimized considering the interference effect in the thin-film devices. Due to the relatively high bandgap of conjugated polymer and consequently the insufficient light absorption, lowering bandgap of the absorber is another effective way to improve the performance of OSCs. The simulation also indicates that unbalanced carrier transport is detrimental to the extraction of carriers and need to be further optimized.

To optimize unbalanced transport of electrons and holes in BHJ OSCs, experiments on SWCNTs enhanced P3HT/PCBM solar cells are discussed in Chapter 5. *J*-*V* characteristic shows that by introducing small portion of SWCNTs in the active layer, PCE does increase due to the ballistic pathway provided by semiconducting SWCNTs. However, further increasing the concentration of SWCNTs degrades performance because of the detrimental effect of metallic SWCNTs in the active layer.

Microscopically, the electrical role of SWCNTs is explored in Chapter 6. By scanning Kelvin Probe Force Microscopy (KPFM) of SWCNTs on top of P3HT/PCBM, we have concluded that SWCNTs is a donor material to transport holes and hence the unbalanced transport of electrons and holes in OSCs is alleviated by the introduction of SWCNTs.

The conclusion and future work are discussed in Chapter 7.

# 2.0 MODELING AND SIMULATION METHOD FOR BHJ OSCS

It is well known that theoretical and simulation studies will give insight and guidance to optimize the performance of OSCs. The theoretical part of this Ph.D dissertation is to explore the modeling of OSCs from both the fundamental understandings on the device physics and experimental evidences. The modeling and simulation method for BHJ OSCs will be first developed in this chapter. Then, this simulation tool will be used to investigate the loss mechanism in Chapter 3 and also to optimize the performance of BHJ OSCs in Chapter 4.

## 2.1 BASIC EQUATIONS

The basic operation of BHJ OSCs can be summarized as follows: Tightly bound excitons are initially created in the conjugated polymer after photoexcitation because of the low dielectric constant of organic materials. Subsequently, excitons diffuse to the donor/acceptor interface and dissociate to charge-transfer excitons (CTEs), which can either undergo geminate recombination or be separated to free electrons and holes. Then, free carriers are transported through segregated phases and are eventually collected by electrodes.

It is necessary to mention that one-dimension simulation is enough to describe the performance of OSCs because they are thin film devices (thickness is around 100nm) [29]. Therefore, only one-dimension simulation is considered for clarity.

The electrical behavior of semiconductor devices is described by Poisson's equation

$$\frac{\partial^2}{\partial x^2}\varphi(x) = \frac{q}{\varepsilon}[n(x) - p(x)], \quad \textbf{2.1}$$

and continuity equations for electrons and holes as [30]:

$$\frac{\partial n}{\partial t} = G - R_n + \frac{1}{q}\frac{\partial J_n(x)}{\partial x}, \quad \textbf{2.2}$$

$$\frac{\partial p}{\partial t} = G - R_p - \frac{1}{q}\frac{\partial J_p(x)}{\partial x}, \quad \textbf{2.3}$$

in which, $\varphi$ represents electric potential, $q$ is unit charge, $\varepsilon$ is dielectric constant of the semiconductor, $n$ and $p$ are electron and hole density respectively, $J_n$ ($J_p$) is electron (hole) current density, $G$ is generation rate and $R_{n(p)}$ is recombination rate. For the steady state analysis ($\partial n/\partial t = \partial p/\partial t = 0$), Eq. 2.2-2.3 can be simplified as:

$$\frac{\partial J_n(x)}{\partial x} = q(-G + R_n), \quad \textbf{2.4}$$

$$\frac{\partial J_p(x)}{\partial x} = q(G - R_p). \quad \textbf{2.5}$$

$J_n$ ($J_p$) can be written as functions of $\varphi$, $n$ and $p$, consisting of drift and diffusion components:

$$J_n = -qn(x)\mu_n\frac{\partial}{\partial x}\varphi(x) + qD_n\frac{\partial}{\partial x}n(x), \quad \textbf{2.6}$$

$$J_p = -qp(x)\mu_p\frac{\partial}{\partial x}\varphi(x) - qD_p\frac{\partial}{\partial x}p(x), \quad \textbf{2.7}$$

where $\mu_{n(p)}$ is electron (hole) mobility and $D_{n(p)}$ is electron (hole) diffusion coefficients. The mobility and diffusion coefficient are governed by classical Einstein relation as

$$\frac{D_{n(p)}}{\mu_{n(p)}} = \frac{kT}{q}. \quad \textbf{2.8}$$

Our goal is to obtain carrier density $n(x)$, $p(x)$ as well as electric potential $\varphi(x)$ in the semiconductor. Therefore, put Eq. 2.6-2.7 back to Eq. 2.4-2.5 to eliminate $J_n$ and $J_p$. Then, we can obtain three differential equations (one is Poisson Equation and other two are carrier continuity equation) as follows:

$$\frac{\partial^2}{\partial x^2}\varphi(x) = \frac{q}{\varepsilon}[n(x) - p(x)], \tag{2.9}$$

$$-n(x)\mu_n \frac{\partial^2 \varphi}{\partial x^2} - \frac{\partial n}{\partial x}\mu_n \frac{\partial \varphi}{\partial x} + D_n \frac{\partial^2 n}{\partial x^2} = -G + R_n, \tag{2.10}$$

$$-p(x)\mu_p \frac{\partial^2 \varphi}{\partial x^2} - \frac{\partial p}{\partial x}\mu_p \frac{\partial \varphi}{\partial x} - D_p \frac{\partial^2 p}{\partial x^2} = G - R_p. \tag{2.11}$$

Ohmic contacts are always implemented as simple Dirichlet boundary conditions, where the surface potential, electron and hole densities ($\varphi(0), \varphi(L), n(0), n(L), p(0), p(L)$) are fixed at both ends. The assumption of ohmic contact is a kind of approximation, which simplifies the modeling of BHJ OSCs. We will further discuss this issue in Section 7.2.

To simulate BHJ OSCs by the physics model above, several issues need to be addressed because of their unique properties. First, $\varepsilon$ is spatially averaged dielectric constant of donor/acceptor blending and depends on the weight ratio between donor and acceptor materials [31]. Second, apparent carrier mobility ($\mu_e$ in the acceptor and $\mu_h$ in the donor) in BHJ configuration is different from the value in their pristine phase, and strongly related to the nano-morphology in the blending [32, 33]. Third, it has been experimentally verified that $V_{oc}$ was mainly determined by the potential difference between HOMO of the donor ($E^d_{HOMO}$) and LUMO of the acceptor ($E^a_{LUMO}$) [34]. Therefore, the effective bandgap ($E_g$) in the simulation was expressed as $E_g = E^a_{LUMO} - E^d_{HOMO}$ [29]. Although Einstein relation ($D/\mu = kT/q$) might not hold well in disordered materials [35], it was still assumed in the

simulation for simplicity without causing significant deviation [29, 36]. This issue will be further discussed in the next chapter.

## 2.2 ALGORITHM TO SOLVE COUPLED DIFFERENTIAL EQUATIONS

To solve coupled differential equations (Eq 2.9-2.11) is not trivial because the change of electric potential in the semiconductor is gradual but the change of carrier density is very fast. The general calculation method will always result in non-converge situation. Therefore, finite difference (FD) method and special iteration technique (Gummel method and Newton method) will be used to solve the coupled nonlinear differential equations.

### 2.2.1 Normalization

It is well known that normalization is an important technique to simplify the calculation in the numerical simulation, especially for Poisson and continuity equations ($\varphi$, $n$, $p$) in which there are some constant parameters. The other reason for normalization is that the values of $n$, $p$ , $\varphi$ have large difference which need reduce the order of $n$, $p$ $\varphi$ in the calculation to make the numerical simulation feasible and accurate. The normalization parameters [37] are Debye length ( $L_D = \sqrt{\varepsilon kT / q^2 n_i}$ ), intrinsic carrier density ($n_i$), and thermal energy ($kT/q$) as shown in the Table 2.1.

After normalization, Eq. 2.1, 2.4, 2.5-2.7 change to:

Poisson Equation: $\frac{\partial^2}{\partial x^2}\varphi(x) = \frac{q}{\varepsilon}[n(x) - p(x)] \Rightarrow \frac{\partial^2}{\partial x^2}\varphi(x) = n(x) - p(x)$ **2.1'**

Electron Continuity Equation: $\frac{\partial J_n(x)}{\partial x} = q(-G + R_n) \Rightarrow \frac{\partial J_n(x)}{\partial x} = -G + R_n$ **2.4'**

Hole Continuity Equation: $\frac{\partial J_p(x)}{\partial x} = q(G - R_p) \Rightarrow \frac{\partial J_p(x)}{\partial x} = G - R_p$ **2.5'**

Electron current: $J_n = -qn(x)\mu_n \frac{\partial}{\partial x}\varphi(x) + qD_n \frac{\partial}{\partial x} n(x) \Rightarrow J_n = -n(x)\mu_n \frac{\partial}{\partial x}\varphi(x) + D_n \frac{\partial}{\partial x} n(x)$ **2.6'**

Hole current: $J_p = -qp(x)\mu_p \frac{\partial}{\partial x}\varphi(x) - qD_p \frac{\partial}{\partial x} p(x) \Rightarrow J_p = -p(x)\mu_p \frac{\partial}{\partial x}\varphi(x) - D_p \frac{\partial}{\partial x} p(x)$ **2.7'**

**Table 2.1** Parameter normalization.

| Parameter | Normalization parameter | unit | After normalization |
|---|---|---|---|
| **Position (*x*)** | $L_D = \sqrt{\varepsilon kT / q^2 n_i}$ | *cm* | $X=X/L_D$ |
| **Potential ($\varphi$)** | $V_{kT} = kT/q$ | V | $\varphi = \varphi / V_{kT}$ |
| **Carrier density (*n*, *p*)** | $n_i$ | $cm^{-3}$ | $n=n/n_i$ |
| **Diffusion ($D_{n,p}$)** | $D_0$ | $cm^2/s$ | $D_{n,p}= D_{n,p}/D_0$ |
| **Mobility ($\mu_{n,p}$)** | $\mu_0 = qD_0 / kT$ | $cm^2/V*s$ | $\mu_{n,p} = \mu_{n,p} / \mu_0$ |
| **Time (*t*)** | $t_0 = L_D^2 / D_0$ | *s* | $t = t / t_0$ |
| **Recombination rate (*R*)** | $R_0 = D_0 n_i / L_D^2$ | $1/cm^3*s$ | $R = R / R_0$ |
| **Current density ($J_{n,p}$)** | $J_0 = qD_0 n_i / L_D$ | $A/cm^2$ | $J = J / J_0$ |

### 2.2.2 Discretization

To solve the differential equations on a computer, they much be discretized on a simulation grid so that the continuous functions are represented by vectors values at the nodes and the differential function are replaced by suitable difference operators.

One dimensional ununiform grid is shown in Figure 2.1. The region considered here ($x=0$ to $x=W$) has been discretized to $N_w$ nodes, which were numbered as 1, 2, …, N, …, $N_w$. The discretization is flexible and is dependent on different situations. For example,

considering p-n junction, node separation near the charge depletion region should be denser because electric potential changes much faster in the charge depletion region. The middle point between N node and N+1 node was named M. Therefore, there are totally $N_w$-1 middle points between the nearest nodes, named 1, 2, …, M, …, $M_w$ ($M_w$=$N_w$-1).

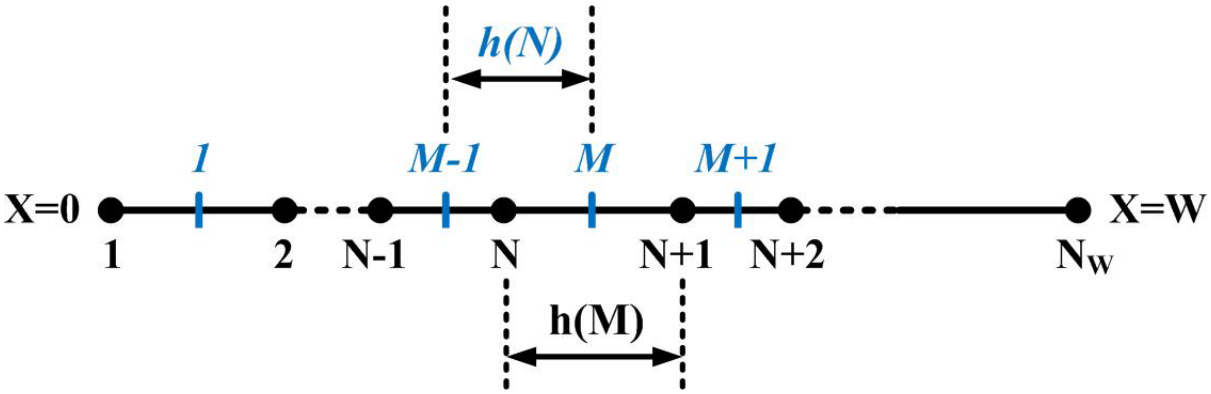


**Figure 2.1** Schematic of one dimensional discretization.

Assuming the distance between N node and N+1 node is h(M) and the distance between middle point M-1 and M is h(N), it is clear that:

$$h(N)=\frac{1}{2}[h(M-1)+h(M)]. \qquad \textbf{2.12}$$

For Poisson equation, using central difference formula, it is obtained that

$$\frac{\partial\varphi(N)}{\partial x}=\frac{\varphi(M)-\varphi(M-1)}{h(N)}+O(h)*\frac{\partial^2\varphi(N)}{\partial x^2}. \qquad \textbf{2.13}$$

Neglecting higher orders, it is

$$\frac{\partial\varphi(N)}{\partial x}=\frac{\varphi(M)-\varphi(M-1)}{h(N)}. \qquad \textbf{2.14}$$

Considering Eq 2.14, the second derivative of $\varphi$ respect to $x$ can be expressed as:

$$\frac{\partial^2\varphi(N)}{\partial x^2}=\frac{\partial}{\partial x}[\frac{\partial\varphi(N)}{\partial x}]=\frac{\partial}{\partial x}[\frac{\varphi(M)-\varphi(M-1)}{h(N)}]$$
$$=\frac{1}{h(N)}[\frac{\varphi(N+1)-\varphi(N)}{h(M)}-\frac{\varphi(N)-\varphi(N-1)}{h(M-1)}] \quad . \qquad \textbf{2.15}$$

Therefore, the discretization of normalized Poisson Equation (Eq 2.1') can be expressed as:

$$r_1(N)\varphi(N-1)+r_2(N)\varphi(N)+r_3(N)\varphi(N+1)=[n(N)-p(N)]$$
$$r_1(N)=\frac{1}{h(N)h(M-1)}$$
$$r_2(N)=-[\frac{1}{h(M)h(N)}+\frac{1}{h(M-1)h(N)}] \quad . \qquad \textbf{2.16}$$
$$r_3(N)=\frac{1}{h(N)h(M)}$$

The next step is to discretize the normalized continuity equations (Eq. 2.4'-2.5'), which requires more care since it is necessary to approximate the carrier densities between two grid points in order to get a finite difference equation. The technique used above for surface potential, which is simply approximating the surface potential by averaging between grid points, will lead to serious instabilities as the carrier concentrations can change very rapidly between grid points [29, 37, 38]. For example, it is very common that the carrier density in silicon p-n junction can change from $10^8/cm^3$ to $10^{18}/cm^3$. Therefore, Scharfetter and Gummel method [38] was applied to discretize the continuity equations. In the following, only electron continuity equation is considered and discretization of hole continuity equation has similar formation.

$$\frac{\partial J_n(N)}{\partial x}=\frac{J_n(M)-J_n(M-1)}{h(N)} \quad . \qquad \textbf{2.17}$$

In order to derive the relation between $J_n$ and $n$ in the middle points ($M_i$) of grids ($N_i$), electron current ($J_n$) near the middle point (M+1) will be expressed as:

$$J_n(x)=J_n(M+1)+(x-x_{M+1})\frac{\partial J_n(M+1)}{\partial x} \quad . \qquad \textbf{2.18}$$

Eq 2.6 can be modified as:

$$-qn(x)\mu_n\frac{\partial\varphi(x)}{\partial x}+qD_n\frac{\partial n(x)}{\partial x}=J_n(M+1)+(x-x_{M+1})\frac{\partial J_n(M+1)}{\partial x}. \qquad \textbf{2.19}$$

Assuming $\frac{\partial\varphi}{\partial x}$, $J_n(M+1)$, $\frac{\partial J_n(M+1)}{\partial x}$ are all constant, we can express $n(x)$ as the function of $J_n(M+1)$:

$$\begin{aligned} n(x) &= c_n\exp\frac{[\varphi(N+1)-\varphi(N)]x}{h_i\beta_T} \\ &+\frac{h_i\beta_T J_n(M+1)}{D_n[\varphi(N+1)-\varphi(N)]}*\{\exp\frac{[\varphi(N+1)-\varphi(N)]x}{h_i\beta_T}-1\} \\ &+\frac{h_i\beta_T\frac{\partial J_n(M+1)}{\partial x}}{D_n[\varphi(N+1)-\varphi(N)]}*\{[\exp\frac{[\varphi(N+1)-\varphi(N)]x}{h_i\beta_T}-1]*[\frac{h_i\beta_T}{\varphi(N+1)-\varphi(N)}-(x_i+\frac{h_i}{2})]-x\} \end{aligned} \quad , \quad \textbf{2.20}$$

in which $c_n$ and $c_p$ are constant to be determined. $\frac{\beta_T}{k_BT/q}=\frac{D_n}{\mu_n}$. Consider Einstein relation, $\beta_T=1$. Using boundary condition:

$$\begin{cases} n(x)=n(N) \\ p(x)=p(N) \end{cases} \quad at\ x=N. \qquad \textbf{2.21}$$

And neglect $\frac{\partial J_{n(p)}}{\partial x}$, $c_n$ and $c_p$ can be obtained. Then consider boundary condition at N+1, which is

$$\begin{cases} n(x)=n(N+1) \\ p(x)=p(N+1) \end{cases} \quad at\ x=N+1. \qquad \textbf{2.22}$$

After eliminating $J_n$ and $J_p$, it is obtained that:

$$n(x)=n(N)[1-f_N(x,\varphi)]+n(N+1)f_N(x,\varphi), \qquad \textbf{2.23}$$

in which,

$$f_N(x,\varphi)=\frac{1}{\exp\frac{\varphi(N+1)-\varphi(N)}{\beta_T}-1}*[\exp\frac{[\varphi(N+1)-\varphi(N)](x-x_i)}{h_i\beta_T}-1]. \qquad \textbf{2.24}$$

Based on Eq 2.23-2.24, set x=M and we can get the relation between $J_n$ and $n$ in the middle points ($M_i$) of grids ($N_i$) as:

$$n(M)=\frac{\beta_T}{\varphi(N+1)-\varphi(N)}*Ber[\frac{\varphi(N+1)-\varphi(N)}{\beta_T}]*[\exp\frac{\varphi(N+1)-\varphi(N)}{2\beta_T}-1]* \\ [n(N)\exp\frac{\varphi(N+1)-\varphi(N)}{2\beta_T}+n(N+1)] \quad \textbf{2.25}$$

$$\frac{\partial n(M)}{\partial x}=Ber[\frac{\varphi(N+1)-\varphi(N)}{\beta_T}]*[\exp\frac{\varphi(N+1)-\varphi(N)}{2\beta_T}-1]*\frac{n(N+1)-n(N)}{h_i}, \quad \textbf{2.26}$$

in which, Ber(x) is Bernoulli function as

$$Ber(x)=\frac{x}{e^x-1}. \quad \textbf{2.27}$$

From Eq 2.25, it is clear that at middle between nearest grid points, the carrier density has nonlinear relation versus the distance. Therefore, the simple central difference formula can not be used to express the derivative of carrier density. From Eq 3.25-3.26, we can get the express of $J_{n(p)}$ as a function of carrier density:

$$J_n(M)=\frac{D_n(M)}{h_i}\{Ber[\Delta\varphi(N)]*n(N+1)-Ber[-\Delta\varphi(N)]*n(N)\}, \quad \textbf{2.28}$$

$$J_p(M)=\frac{D_p(M)}{h_i}\{Ber[\Delta\varphi(N)]*p(N)-Ber[-\Delta\varphi(N)]*p(N+1)\}, \quad \textbf{2.29}$$

in which, $\Delta\varphi(N)=\varphi(N+1)-\varphi(N)$. At this stage, we have finished the discretization of potential $\varphi(x)$ as well as carrier density $J_{n(p)}(x)$.

### 2.2.3 Linearization

Discretized equations (Eq 2.16, 28, 29) need to be linearized in order to use computer to get the numerical solutions of $\varphi(x)$, $n(x)$ and $p(x)$. The discretized Poisson equation (Eq 2.16) can be linearized as:

$$\begin{aligned}&\delta p(N)-\delta n(N)+r_1(N)\delta\varphi(N-1)+r_2(N)\delta\varphi(N)+r_3(N)\delta\varphi(N+1)=\\&-r_1(N)\varphi^0(N-1)-r_2(N)\varphi^0(N)-r_3(N)\varphi^0(N+1)+n^0-p^0\end{aligned}, \qquad \textbf{2.30}$$

and $r_i$ are defined in Eq 2.16. For linearization of carrier continuity equation, we can write:

$$\begin{aligned}J_n(M)=J_n^0(M)+\delta J_n(M)=J_n^0(M)+\frac{\partial J_n^0(M)}{\partial n(N)}\delta n(N)+\frac{\partial J_n^0(M)}{\partial n(N+1)}\delta n(N+1)\\+\frac{\partial J_n^0(M)}{\partial\varphi(N)}\delta\varphi(N)+\frac{\partial J_n^0(M)}{\partial\varphi(N+1)}\delta\varphi(N+1)\end{aligned}, \qquad \textbf{2.31}$$

$$\begin{aligned}J_p(M)=J_p^0(M)+\delta J_p(M)=J_p^0(M)+\frac{\partial J_p^0(M)}{\partial p(N)}\delta p(N)+\frac{\partial J_p^0(M)}{\partial p(N+1)}\delta p(N+1)\\+\frac{\partial J_p^0(M)}{\partial\varphi(N)}\delta\varphi(N)+\frac{\partial J_p^0(M)}{\partial\varphi(N+1)}\delta\varphi(N+1)\end{aligned}. \qquad \textbf{2.32}$$

Recombination (R) can be expressed as:

$$R(N)=R^0(N)+\frac{\partial R^0(N)}{\partial p(N)}\delta p(N)+\frac{\partial R^0(N)}{\partial n(N)}\delta n(N). \qquad \textbf{2.33}$$

Put Eq 2.31-2.33 back to continuity equations of electrons and holes (Eq 2.4-2.5), we can get the linearization of continuity equations as followed:

$$\begin{aligned}&\frac{\partial R^0(N)}{\partial p(N)}*\delta p(N)+\frac{1}{h(N)}\frac{\partial J_n^0(M-1)}{\partial n(N-1)}*\delta n(N-1)-[\frac{1}{h(N)}(\frac{\partial J_n^0(M)}{\partial n(N)}-\frac{\partial J_n^0(M-1)}{\partial n(N)})-\frac{\partial R^0(N)}{\partial n(N)}]*\delta n(N)\\&-\frac{1}{h(N)}\frac{\partial J_n^0(M)}{\partial n(N+1)}*\delta n(N+1)+\frac{1}{h(N)}\frac{\partial J_n^0(M-1)}{\partial\varphi(N-1)}*\delta\varphi(N-1)-\frac{1}{h(N)}(\frac{\partial J_n^0(M)}{\partial\varphi(N)}-\frac{\partial J_n^0(M-1)}{\partial\varphi(N)})*\delta\varphi(N)\\&-\frac{1}{h(N)}\frac{\partial J_n^0(M)}{\partial\varphi(N+1)}*\delta\varphi(N+1)=\frac{1}{h(N)}[J_n^0(M)-J_n^0(M-1)]-R^0(N)\end{aligned}$$

**2.34**

$$\frac{1}{h(N)}\frac{\partial J_p^0(M-1)}{\partial p(N-1)}*\delta p(N-1)+[\frac{1}{h(N)}(\frac{\partial J_p^0(M)}{\partial p(N)}-\frac{\partial J_p^0(M-1)}{\partial p(N)})-\frac{\partial R^0(N)}{\partial p(N)}]*\delta p(N)$$
$$-\frac{1}{h(N)}\frac{\partial J_p^0(M)}{\partial p(N+1)}*\delta p(N+1)-\frac{\partial R^0(N)}{\partial n(N)}*\delta n(N)+\frac{1}{h(N)}\frac{\partial J_p^0(M-1)}{\partial \varphi(N-1)}*\delta\varphi(N-1) \quad . \quad \textbf{2.35}$$
$$-\frac{1}{h(N)}(\frac{\partial J_p^0(M)}{\partial \varphi(N)}-\frac{\partial J_p^0(M-1)}{\partial \varphi(N)})*\delta\varphi(N)-\frac{1}{h(N)}\frac{\partial J_p^0(M)}{\partial \varphi(N+1)}*\delta\varphi(N+1)$$
$$=\frac{1}{h(N)}[J_p^0(M)-J_p^0(M-1)]+R^0(N)$$

### 2.2.4 Iteration Method

Basically, two methods (Figure 2.2) are available to solve the discretized and linearized Poisson and continuity equations numerically: decoupled method (Gummel's method) [37] and coupled method (Newton method)[39].

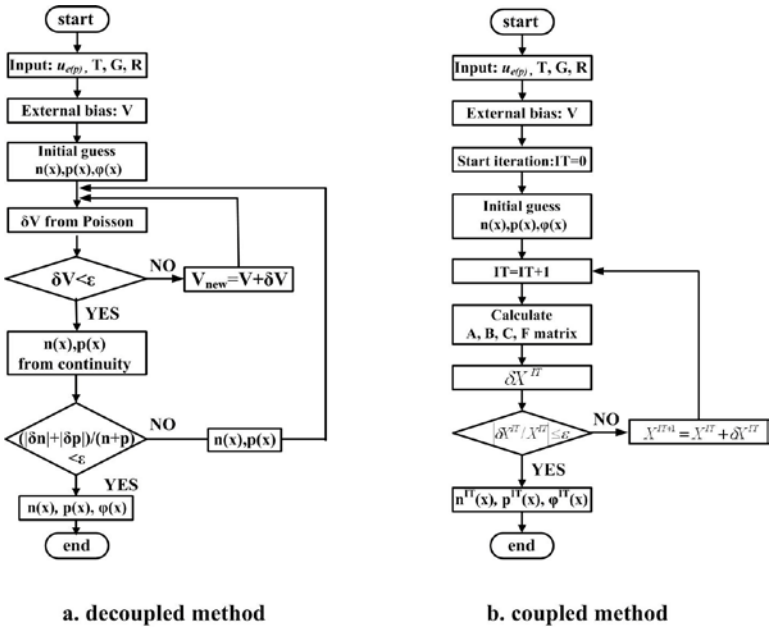


**Figure 2.2** Simulation flow diagram of decoupled method (a) and coupled method (b).

Equations are solved sequentially if decoupled method is applied. Assuming fixed quasi-Fermi levels, Poisson equation is solved by an inner Newton loop. Then new potential is substituted into continuity equations to solve the electron and hole density. The new carrier concentrations are substituted back into the charge term of Poisson equation and another iteration begins. The flow diagram of decoupled simulation is shown in Figure 2.2a [29, 37, 40]. The advantage of decoupled method is for each time, the dimension of the calculation matrix is *N*N*, which is smaller than coupled method (*3N*3N*) discussed below. Therefore, the memory occupation is smaller and calculation time is shorter than coupled method. However, the success of the decoupled method depends on the degree of coupling between electric potential and carrier densities, and therefore sometimes the converge of the decoupled method is very slow.

As shown in the flow diagram of coupled method in Figure 2.2b, all variables ( $n(x), p(x), \varphi(x)$ ) are allowed to change during each iteration and all of the coupling effects between these variables is taken into account, which makes the Newton algorithm is very stable and the solution time is nearly independent of initial guess. The basic idea of Newton iteration is as followed.

Express Eq 2.30, 34, 35 in matrix form as:

$$\begin{bmatrix} a_{11} & a_{12} & a_{13} \\ a_{21} & a_{22} & a_{23} \\ a_{31} & a_{32} & a_{33} \end{bmatrix} * \begin{bmatrix} \delta n(N-1) \\ \delta p(N-1) \\ \delta \varphi(N-1) \end{bmatrix} + \begin{bmatrix} b_{11} & b_{12} & b_{13} \\ b_{21} & b_{22} & b_{23} \\ b_{31} & b_{32} & b_{33} \end{bmatrix} * \begin{bmatrix} \delta n(N) \\ \delta p(N) \\ \delta \varphi(N) \end{bmatrix} + \begin{bmatrix} c_{11} & c_{12} & c_{13} \\ c_{21} & c_{22} & c_{23} \\ c_{31} & c_{32} & c_{33} \end{bmatrix} * \begin{bmatrix} \delta n(N+1) \\ \delta p(N+1) \\ \delta \varphi(N+1) \end{bmatrix} = \begin{bmatrix} f_1(N) \\ f_2(N) \\ f_3(N) \end{bmatrix} \quad \textbf{2.36}$$

If we define: $A(N) = \begin{bmatrix} a_{11} & a_{12} & a_{13} \\ a_{21} & a_{22} & a_{23} \\ a_{31} & a_{32} & a_{33} \end{bmatrix}$, $B(N) = \begin{bmatrix} b_{11} & b_{12} & b_{13} \\ b_{21} & b_{22} & b_{23} \\ b_{31} & b_{32} & b_{33} \end{bmatrix}$, $c(N) = \begin{bmatrix} c_{11} & c_{12} & c_{13} \\ c_{21} & c_{22} & c_{23} \\ c_{31} & c_{32} & c_{33} \end{bmatrix}$, $\delta X(N) = \begin{bmatrix} \delta n(N) \\ \delta p(N) \\ \delta \varphi(N) \end{bmatrix}$

and $F(N) = \begin{bmatrix} f_1(N) \\ f_2(N) \\ f_3(N) \end{bmatrix}$. Eq 2.45 can be simplified as:

$$A(N)\delta X(N-1) + B(N)\delta X(N) + C(N)\delta X(N+1) = F(N) \quad \textbf{2.37}$$

Because there are N nodes, N equations of the form Eq 2.36 need to be solved numerically. The disadvantage of Newton's method is that for large grids, the time and computer memory consuming to invert the big Jacobian matrix is excessive. However, for Jacobian matrix, it is clear that most elements are zero. Therefore, sparse matrix can be used to reduce the memory consumption and accelerate the computing.

Decoupled method was applied in our simulation of BHJ OSCs considering two reasons: 1. For OSCs, the mobility is much lower than inorganic materials and therefore, the coupling between drift current and built-in potential ( $J_d \propto \mu * \partial\varphi / \partial x$ ) is small and converge is fast. 2. The computation time is fast (N*N matrix) compared with coupled method (3N*3N matrix).

## 2.3 SIMULATION OF *J-V* CURVES

After successfully solving Poisson and continuity equations in Section 2.2, we are able to obtain the current density (*J*) at fixed bias voltage (*V*). In order to predict the behavior of OSCs, Gummel iteration was repeated at different applied voltage *V* to simulate *J-V* curves.

The typical *J-V* curves of the PV device in the dark (black, dashed-dot) and under illumination (red, solid line) are simulated as shown in Figure 2.3. It is obvious that the curve shows typical diode behavior in the dark as we expect. When the cell is illuminated, *J-V* curve is shifted down by the amount of photocurrent $J_{ph}$ (blue, dashed line). The open circuit voltage $V_{oc}$ is the maximum voltage that can be generated in the cell and corresponds to the voltage where current under illumination is zero. The current density that can run through the

cell at zero applied voltage is called short circuit current $J_{sc}$. $V_{FB}$ is called flat band voltage, where the extraction of photocurrent is absolutely zero. $V_{FB}$ is bigger compared with $V_{oc}$, because there should be non-zero electric field at $V_{oc}$ so that the drift current (proportional to electric field) can absolutely cancel the diffusion current.

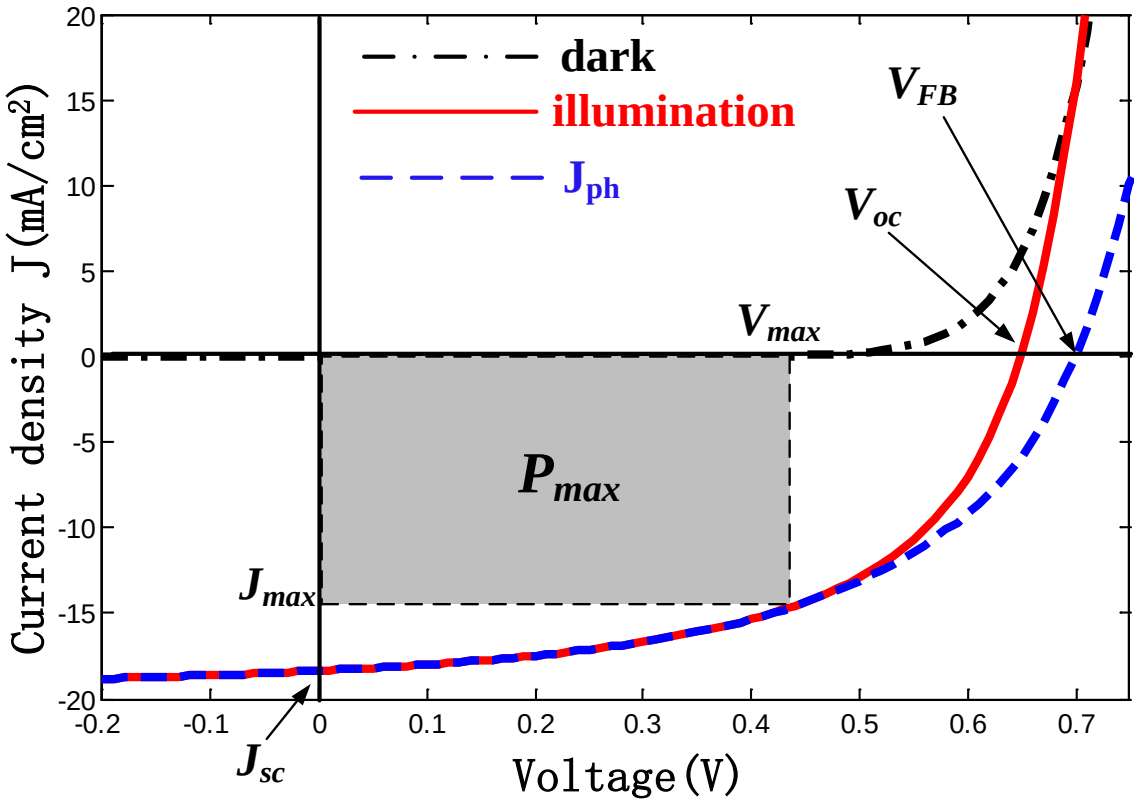


**Figure 2.3** *J-V* characteristic curves of the typical PV device in the dark (black dashed-dot) and under illumination (red solid line). The blue dashed line represents the extracted photocurrent $J_{ph}$ under illumination.

The maximum electrical power $P_{max}$ is located in the fourth quadrant where the product of current density $J$ and voltage $V$ reached its maximum value. It is obvious from Figure 2.3 that $P_{max}$ is bigger when the *J-V* curve resembles a rectangular with the area

$V_{oc} \times J_{sc}$. The ratio between $P_{\max}$ and $V_{oc} \times J_{sc}$ resembles the quality of *J-V* curve shape and is defined as the fill factor (*FF*)

$$FF = \frac{V_{\max} \times J_{\max}}{V_{oc} \times J_{sc}}.$$

The PCE of a solar cell is the ratio between the maximum output power $P_{\max}$ and the power of the incident light $P_{light}$

$$PCE = \frac{P_{\max}}{P_{light}} = \frac{V_{oc} \times J_{sc} \times FF}{P_{light}}.$$

In order to increase the efficiency, either $V_{oc}$, $J_{sc}$ or *FF* need to be increased. The simulation indicates that $V_{oc}$ is strongly related to the bandgap of semiconductor; the light absorption in solar cells mainly determines $J_{sc}$; and fill factor is affected by the recombination loss in the solar cell devices.

## 2.4 SUMMARY

Under certain condition and simplification, *J-V* characteristics of OSCs can be simulated by the physics models for classical semiconductor devices. In this chapter, we have successfully developed the numerical tools by Gummel iteration to simulate the behavior of OSCs (*J-V* curves). The simulation indicates that increasing bandgap of semiconductors, enhancing the light absorption, and reducing recombination loss are the effective way to increase PCE.

## 3.0 INVESTIGATION ON RECOMBINATION LOSS IN BHJ OSCS

Determining the mechanism of recombination loss is crucial for the accurate modeling and simulation of OSCs [41]. However, this loss mechanism is still under hot debate. Although some research groups insist that bimolecular recombination is the dominant loss mechanism [42], more and more researchers are convinced that monomolecular recombination dictates the performance of OSCs [43-45].

The complexity of interpenetrating bicontinuous networks in BHJ configuration limits theoretical analysis of recombination in OSCs. Experimental studies using transient luminescence with ultrafast lasers is considered a powerful tool for exploring recombination dynamics in semiconductor materials. Unfortunately, luminescence quenching is dominant in OSCs because photoexcited electrons transfer rapidly from donor materials to acceptors (50 fs) [25]. Given the inherent difficulty in investigating the loss mechanism either by theoretical analysis or by experimental observation, numerical simulation offers a feasible alternative for identifying recombination kinetics in OSCs.

## 3.1 LANGEVIN TYPE BIMOLECULAR RECOMBINATION

Modeling studies of BHJ OSCs, which incorporated Onsager theory [46] and charge transport (CT) state proposed by Braun [47], have been relatively limited. Koster *et al.* provided most of these using Langevin type bimolecular recombination [29]. However, we point out that the Langevin type bimolecular recombination is not proper to describe BHJ OSCs and will lead counterintuitive simulation results.

As schematic diagram in Figure 3.1, bimolecular recombination rate is related to two steps: Step 1. finding each other; Step 2. direct recombination rate. In semiconductors with high mobility such as crystal silicon, carriers move very fast to find their counterpart (step 1) and hence direct recombination (step 2) is dominant. However, in materials with low mobility the time to find each other (step 1) is dominant for recombination. Langevin recombination is always used to describe the materials with low mobility, only considering the time for carriers to find counterpart (step 1) and ignoring the direct recombination (step 2).

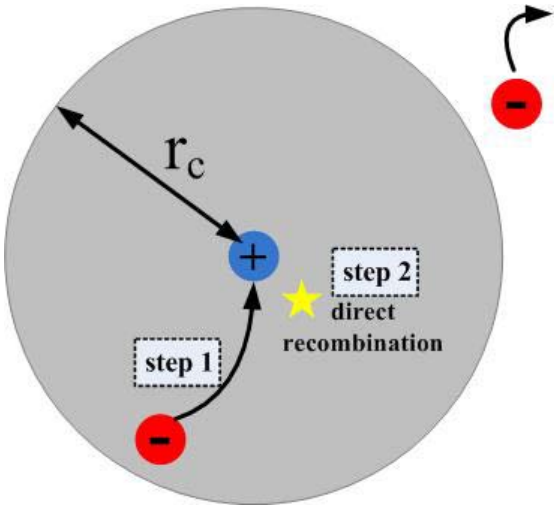


**Figure 3.1** Schematic diagram to explain Coulomb radius $r_c$ and Langevin-type bimolecular recombination rate.

For Langevin recombination, Coulomb radius $r_c$ is defined as:

$$E_{coulomb} = E_{thermal} \Rightarrow \frac{q^2}{4\pi\varepsilon r_c} = kT \Rightarrow r_c = \frac{q^2}{4\pi\varepsilon kT}, \quad \textbf{3.1}$$

in which $q$ is unit charge, $\varepsilon$ is dielectric constant, $r_c$ is Coulomb radius and $kT$ is thermal energy. The drift current density for the mobile electron (relatively fixed hole) is:

$$j_e = qn(\mu_e + \mu_h)E = \frac{q^2}{4\pi\varepsilon r_c^2} n(\mu_e + \mu_h). \quad \textbf{3.2}$$

Considering bimolecular recombination can only take place if they find each other in low-mobility materials, which is the electron current density flowing into the sphere of radius $r_c$ around the hole.

$$I_e = j_e * 4\pi r_c^2 = \frac{q^2}{\varepsilon} n(\mu_e + \mu_h) = rqn, \quad \textbf{3.3}$$

in which $r$ is called Langevin recombination rate as:

$$r = \frac{q}{\varepsilon}(\mu_e + \mu_h). \quad \textbf{3.4}$$

The recombination loss in pristine semiconductor with low carrier mobility can be described by Langevin recombination rate, in which step 2 is ignored. However, besides the low mobility, there is another unique property for BHJ OSCs: two kinds of materials blending together instead of the pristine material and hence photoexcited electrons and holes are not only energy separated but also spatially confined in different phases within nanometer scale, *i.e.*, electrons in the acceptor phase and holes in donor phases. This scenario can not be fully described by Langevin-type bimolecular recombination rate [42, 43, 48].

As shown in Figure 3.2, for pristine materials with low mobility (a), step 1 is the dominant factor to determine recombination, which can be described by Langevin

recombination rate as $r = \frac{q}{\varepsilon}(\mu_e + \mu_h)$. For BHJ OSCs (b), Koster et. al. [42] modified Langevin recombination rate as $r = \frac{q}{\varepsilon}\min(\mu_e, \mu_h)$ considering that electrons in acceptor arriving first at interface have to wait for the slow holes in donor to reach the interface to recombine. However, the value of bimolecular recombination rate proposed by Koster is still too larger compared with the value acquired directly by experiments in BHJ OSCs [49, 50]. The fundamental assumption to determine the bimolecular recombination in Figure 3.2 is: for low mobility materials, step 1 (to find each other) dominate the recombination, which is true for pristine material as shown in Figure 3.2a. However, for BHJ OSCs (Figure 3.2b), when Koster proposed recombination rate as $r = \frac{q}{\varepsilon}\min(\mu_e, \mu_h)$, it implicitly assumed that step 2 (direct recombination rate) is much faster compared with step 1 (to find each other). This might not be true because for BHJ OSCs, instead of bulk recombination in pristine materials, the recombination occurred at the nanoscale interface between donors and acceptors [50]. In order to properly simulate the performance of OSCs, the recombination at the interface should be carefully investigated.

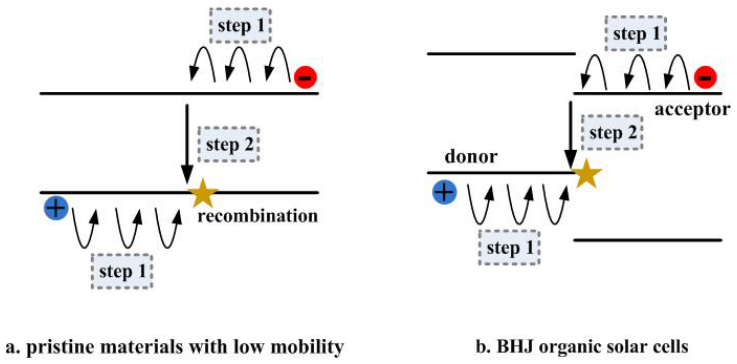


**Figure 3.2** Bimolecular recombination in low-mobility materials. (a) pristine materials. (b) BHJ OSCs.

Theoretically, it has been discussed that Langevin-type bimolecular recombination is not proper to describe the recombination in organic BHJ solar cells above. In the following, we will show the counterintuitive simulation results based on Langevin-type bimolecular recombination. *J-V* curves for different mobility by considering Langevin type bimolecular recombination is simulated in Figure 3.3 and Table 3.1. The y axis in the inset is logarithm scale to clearly see the change of $V_{oc}$. The mobility ratio between electron and hole is fixed at $\mu_h / \mu_e = 0.1$, which is always true for conjugated polymer/fullerene solar cells. It is obvious that with the increase of mobility, fill factor increases a little bit. However, $V_{oc}$ decreases dramatically with increasing carrier mobility. The simulation, based on Langevin type bimolecular recombination, indicates that there is an optimal carrier mobility [51]. If the carrier mobility increased beyond this value, the performance will decrease due to decreased $V_{oc}$. Koster explained that the decreased $V_{oc}$ for high mobility situation as: the difference between the quasi Fermi level of electrons and holes decreased, due to the efficient carrier extraction. However, this statement is questionable as discussed by R. A. Street [43]. At $V_{oc}$, the extraction of electron and hole is almost zero and therefore, instead of carrier extraction, the recombination loss determines $V_{oc}$. Our opinion is coincident with R. A. Street that: the counterintuitive simulation results in Figure 3.3 (high carrier mobility results in low open circuit voltage as well as efficiency) arise from the improper recombination mechanism (Langevin type bimolecular recombination) assumed in the simulation.

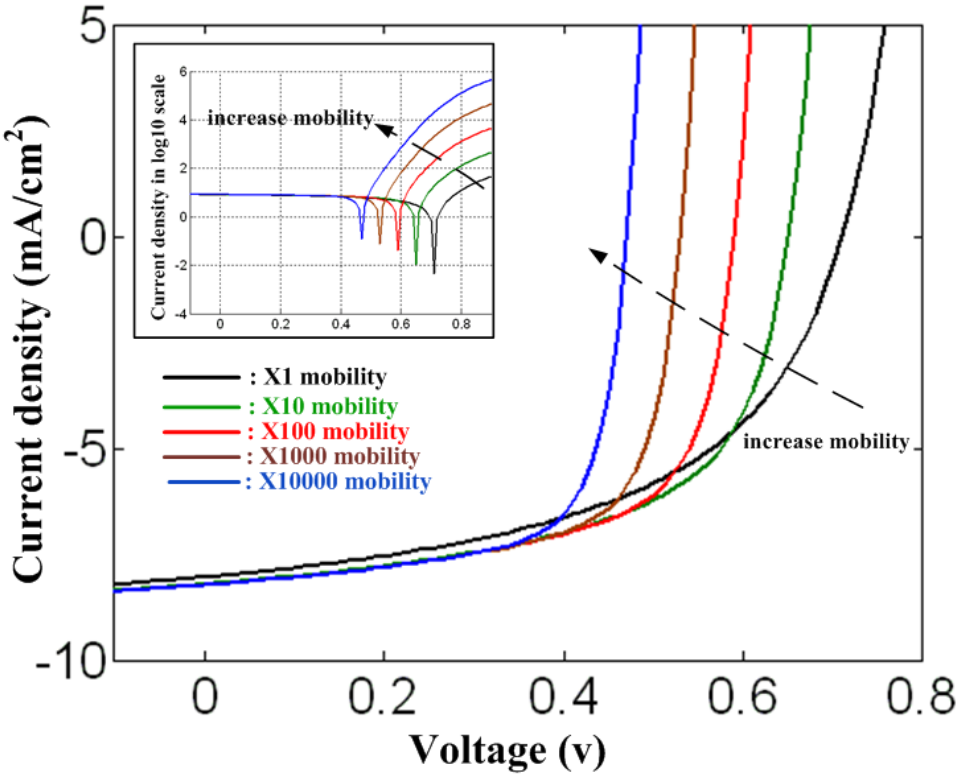


**Figure 3.3** Simulation of mobility dependent *J-V* curves using Langevin bimolecular recombination.

**Table 3.1** Simulation results based on Langevin type recombination.

| | $I_{sc}$(mA/cm$^2$) | $V_{oc}$(V) | FF | efficiency |
|---|---|---|---|---|
| 1X mobility | 8.047 | 0.71 | 0.51 | 2.91% |
| 10X | 8.216 | 0.65 | 0.584 | 3.1% |
| 100X | 8.237 | 0.59 | 0.63 | 3.0% |
| 1000X | 8.239 | 0.53 | 0.66 | 2.8% |
| 10000X | 8.24 | 0.47 | 0.68 | 2.55% |

R. A. Street debates Koster's statement ($V_{oc}$ is determined by extraction of carrier) from theoretical aspect [43]. In the following, we validate Street's argument by simulation (Figure 3.4). Instead of using Langevin type bimolecular recombination rate, the recombination rate was fixed for different carrier mobility in the following simulation. If

Koster's statement was true, $V_{oc}$ should have decreased with increasing mobility because extraction of carrier was efficient for high mobility materials, even though the recombination is not Langevin type. But the following simulations show that if the recombination was fixed, $V_{oc}$ is almost fixed for different carrier mobility (inset of Figure 3.4). Combining the simulation results by Langevin type recombination (Figure 3.3) and by fixed recombination (Figure 3.4), it is concluded that $V_{oc}$ is determined by carrier recombination instead of carrier extraction as suggested by R. A. Street.

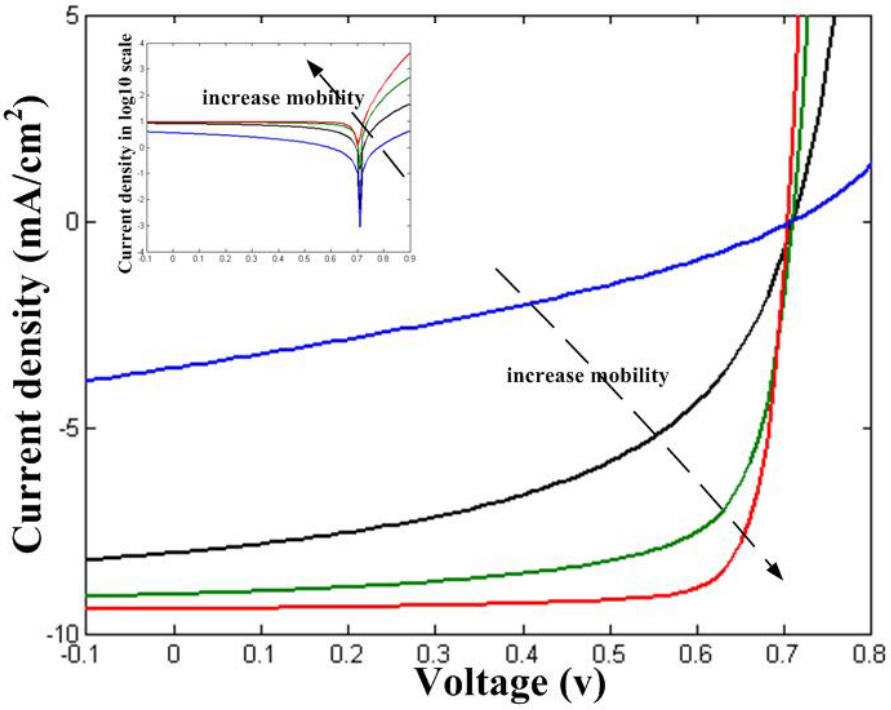


**Figure 3.4** Simulation of mobility dependent *J-V* curves using fixed recombination rate.

## 3.2 INTENSITY DEPENDENT PHOTOCURRENT

The relationship between photocurrent density ($J_{ph}$) of OSCs and illumination intensity ($I$) can be expressed as $J_{ph} \propto I^{\alpha}$. $J_{ph}$ is obtained by subtracting dark current from $J$-$V$ curves at different light intensity. The theoretical analysis including ours suggests that when monomolecular recombination is dominant, α equals one, and α decreases monotonically from the unit with increasing bimolecular recombination [52-54]. However, C. Deibel argued that intensity-dependent photocurrent is not strongly related to the loss mechanism [55]. Therefore, we carried out the rigorous numerical simulation to study intensity-dependent photocurrent.

The simulation parameters of intensity-dependent photocurrent ($J_{ph} \propto I^{\alpha}$) can be found in Table 3.2 and simulation results are shown in Figure 3.5a for monomolecular recombination and in Figure 3.5b for bimolecular recombination. The light intensity investigated here is around one sun intensity ($I_0$), varying from $0.4I_0$ to $1.2I_0$ with step of $0.2I_0$, because the loss mechanism under ordinary operation condition (one sun intensity) is most important for the optimization of OSCs. As shown in Figure 3.5a, $J$-$V$ curves under different light intensity were first calculated at fixed recombination rate ($1us^{-1}$ in the inset of Figure 3.5a); then the value of $\alpha$ in $J_{ph} \propto I^{\alpha}$ was derived by fitting $\log_{10}(J_{ph})$ as a linear function of $\log_{10}(I)$ at different bias voltage (0V, 0.2V and 0.3V). This procedure was repeated at different recombination rate and thus we derived the value of $\alpha$ as a function of recombination rate as shown in Figure 3.5. For easy comparison, the bimolecular recombination rate (Figure 3.5b) is normalized against Langevin type recombination rate

defined as $r_0 = (q/\varepsilon) * (\mu_n + u_p)$. It should be pointed out that the bimolecular recombination in BHJ OSCs is not assumed as Langevin type, which has been discussed in the previous section.

**Table 3.2** Parameters used in the simulation on intensity-dependent photocurrent [55].

| Parameter | Symbol | Value |
|---|---|---|
| Dielectric constant | $<\varepsilon>$ | $3*10^{-13}$ F/cm |
| Effective band gap | $E_g$ | 1.05 eV |
| Effective density of state | $N_c$, $N_v$ | $1*10^{20}$ cm$^{-3}$ |
| Carrier mobility | $\mu_n$, $\mu_p$ | $1*10^{-4}$ cm$^2$/Vs |
| Thickness of active layer | $L$ | 100 nm |
| Generation rate (1 Sun) | $G_0$ | $6*10^{21}$ cm$^{-3}$s$^{-1}$ |
| Temperature | $T$ | 300 K |

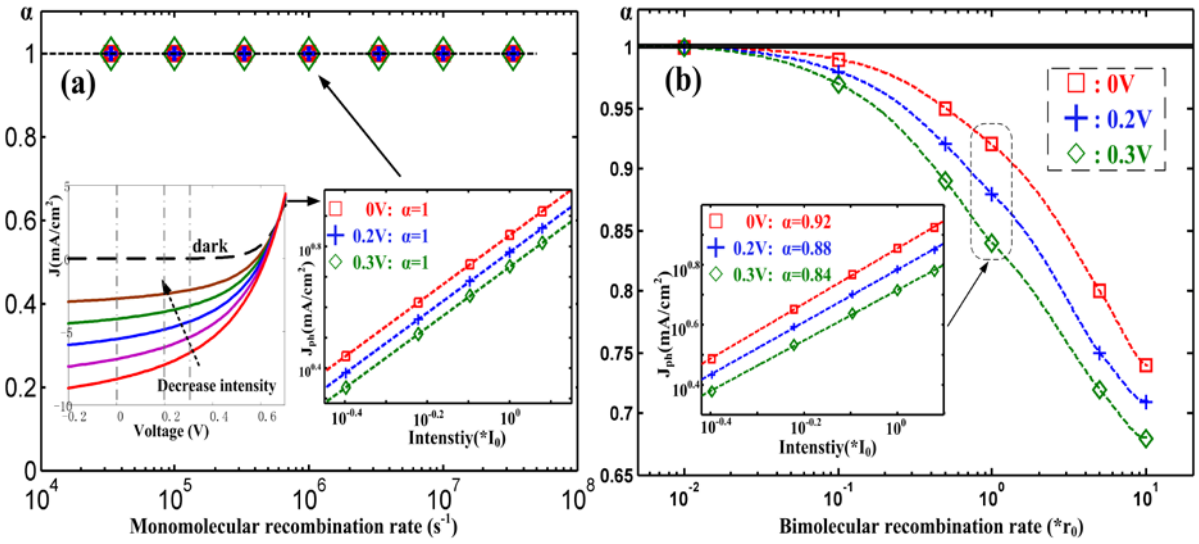


**Figure 3.5** Investigation on intensity-dependent photocurrent ($J_{ph} \propto I^{\alpha}$) for the case of monomolecular recombination loss (a) and of bimolecular recombination loss (b). The symbols are the calculated value of $\alpha$ at different recombination rate (connected by dotted line as a guide).

From the simulation, it can be seen that α equals one in $J_{ph} \propto I^{\alpha}$ when monomolecular recombination ($R = r_m * n$) dominates. Such relation remains unchanged irrespective of the recombination rate ($r_m$) as well as the applied voltage (Figure 3.5a) [55]. However, for the case that bimolecular recombination dominates ($R = r_b * n * p$), different behaviors are observed as shown in Figure 3.5b. When the bimolecular recombination rate is less than $0.01 * r_0$, $\alpha$ is close to one at all applied voltage investigated (0V, 0.2V, 0.3V). When the bimolecular recombination rate is larger than $0.01 * r_0$, the deviation of $\alpha$ from the unit becomes greater and greater as the bimolecular recombination rate becomes larger and larger.

To corroborate our observation, theoretical analysis has been also applied to investigate intensity-dependent photocurrent in addition to the simulation study above. Because carrier extraction by the electrodes is in the monomolecular form [53, 56], change rate of carrier density can be expressed as:

$$dn/dt = G - r_b \cdot n^2 - r_m \cdot n - P(V) \cdot n , \qquad \textbf{3.5}$$

in which $n$ is carrier density, $G$ is generation rate, $r_b$ is bimolecular recombination rate, $r_m$ is monomolecular recombination rate and $P$ is extraction efficiency, which is related to the electric field in the device [56]. For the steady state analysis ($dn/dt = 0$),

$$G - r_b \cdot n^2 - r_m \cdot n - P(V) \cdot n = 0 . \qquad \textbf{3.6}$$

If bimolecular recombination is negligible ($r_b \cdot n^2 << r_m \cdot n$),

$$G - r_m \cdot n - P(V) \cdot n = 0 . \qquad \textbf{3.7}$$

$J_{ph}$ is proportional to the carrier extraction as:

$$J_{ph} \propto P(V) \cdot n = P \cdot G / (r_m + P) . \qquad \textbf{3.8}$$

Because $G$ is proportional to the light intensity $I$, $J_{ph} \propto I^{\alpha}$ with $\alpha$=1, irrespective of recombination magnitude $r_m$. However, this behavior changes if bimolecular recombination loss dominates ($r_b \cdot n^2 >> r_m \cdot n$),

$$G - r_b \cdot n^2 - P(V) \cdot n = 0 . \qquad \textbf{3.9}$$

Based on Eq 3.9, $\alpha$ is less than one for general situation; while for special case in which bimolecular recombination is much smaller compared with carrier extraction ($r_b \cdot n^2 << P(V) \cdot n$), $J_{ph} \propto P(V) \cdot n \propto I$. The detailed mathematical deviation is attached in Appendix A. This theoretical analysis is in coincidence with simulation results in Figure 3.5: the loss mechanism (bimolecular or monomolecular recombination) can not be inferred from intensity dependent photocurrent if recombination is negligible, because carrier extraction has monomolecular form and $\alpha$ always equals one.

From both simulation study and theoretical analysis, we can find that two situations could lead to α=1: First, small bimolecular recombination rate such as $R$=0.01*$r_0$ in Figure 3.5b. Second, monomolecular recombination, irrespective of its magnitude. As suggested by C. Deibel [55], the observation that α equals one may not absolutely lead to a conclusion of monomolecular recombination as under low recombination condition. However, when the recombination is not negligible, bimolecular recombination always suggests the deviation of $\alpha$ from unit while the observation that $\alpha$ equals one suggests a monomolecular recombination. Therefore, it is safe to make a conclusion that monomolecular is dominant when $\alpha$ close to unit if the recombination is non-negligible.

## 3.3 INVESTIGATION OF RECOBMINATION BY SIMULATING INTENSITY DEPENDENT J-V MEASUREMENTS

The intensity-dependent *J-V* curves were chosen to investigate the recombination loss in BHJ OSCs because the simulation on a set of experiments (intensity-dependent *J-V* curves) can provide more reliable results compared with data from a single experiment, which can be easily simulated by manipulating fitting parameters. Before exploring intensity dependent *J-V* curves by the simulation tool developed in Chapter 2, we first investigated intensity-dependent photocurrent ( $J_{ph} \propto I^{\alpha}$ ) by experiments as shown in Figure 3.6. It is shown that $\alpha$ equals one for both annealed and non-annealed devices at all bias voltages. As clarified in Section 3.2, two different situations could result that $\alpha$ equals one: First, bimolecular recombination dominates but the bimolecular recombination rate must be very small ($r_b$<0.01*$r_0$); Second, monomolecular recombination dominates, irrespective of its magnitude. Therefore, in the following, both bimolecular and monomolecular recombination loss will be applied to simulate intensity dependent *J-V* curves.

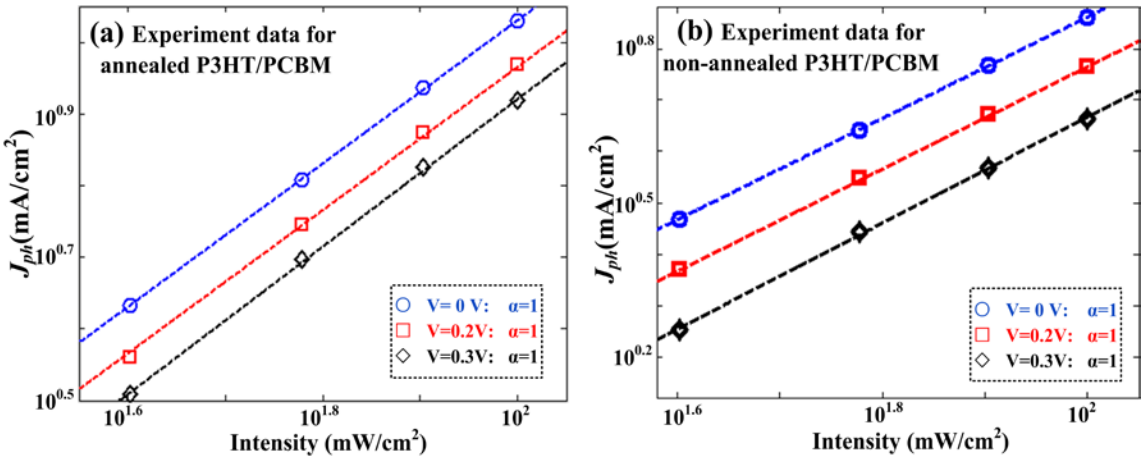


**Figure 3.6** Experimental data for intensity-dependent photocurrents ($J_{ph}$ vs. $I$) in both annealed (a) and non-annealed (b) P3HT/PCBM BHJ OSCs.

Bimolecular recombination ($R_n = R_p = r_b * n * p$) was first applied to simulate intensity dependent *J-V* curves of the annealed P3HT/PCBM devices as shown in Figure 3.7. The symbols represent the experimental data and solid lines are simulation results. We first derived the bimolecular recombination rate ($r_b$) as well as other parameters in Table 3.3 by fitting *J-V* curve of 100mW/cm$^2$ illumination intensity (red square in Figure 3.7). The derived parameters are similar to the reported values by others [32, 57]. Then all other parameters were fixed except generation rate ($G$) to simulate intensity dependent *J-V* curves at other illumination intensity. It is clear that simulation results in Figure 3.7 fit experiments in Region 1 and 3. However, in Region 2, the discrepancies between simulation and experimental values become more and more pronounced as light intensity decreases. It is well known that the extraction of photoexcited carriers is efficient in Region 1 due to the strong electric field at large reversed bias and hence the current in Region 1 is primarily determined by the generation rate $G$; In Region 2 where the internal electric field is moderate, the

extraction of photoexcited carriers is not efficient as in Region 1 and thus the current in Region 2 is strongly reduced by the loss mechanism ($R$); while in Region 3, carrier mobility ($\mu$) determines the current at forward bias. Therefore, deviation of the simulation from the experiment in Region 2 implies that the loss mechanism (bimolecular recombination) assumed in the simulation is unsuitable.

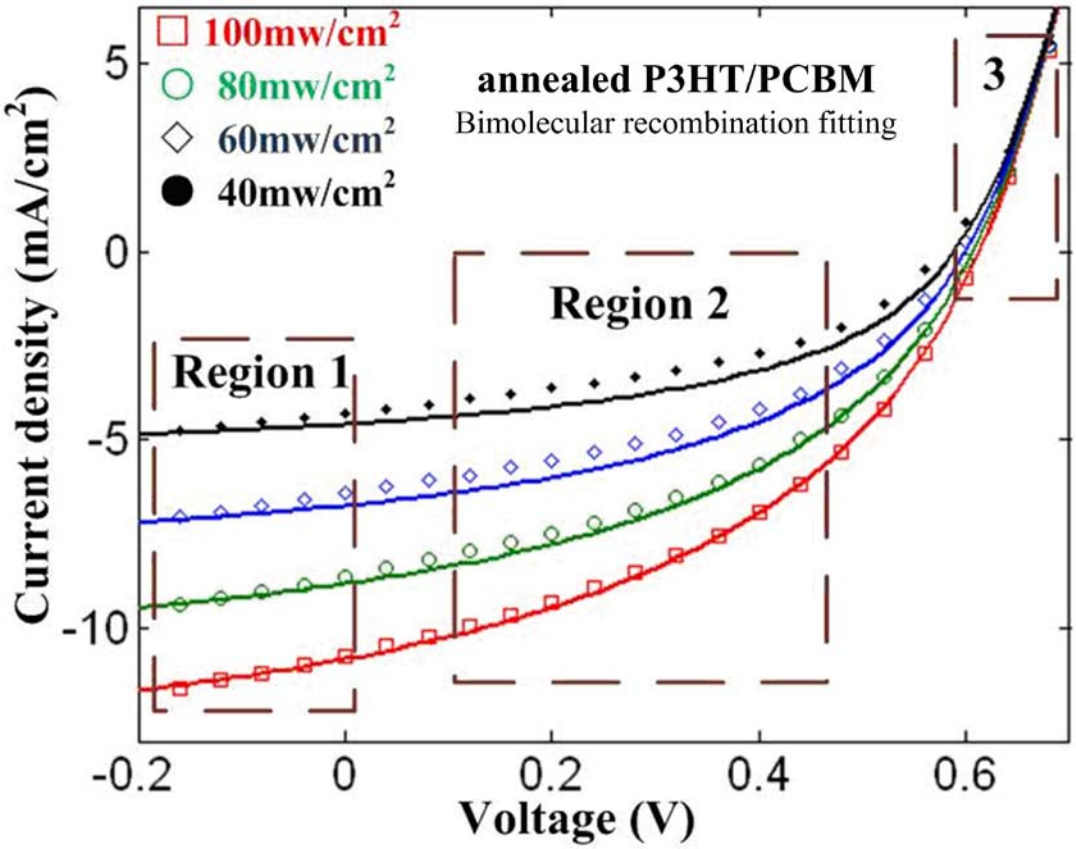


**Figure 3.7** Simulation of intensity-dependent current-voltage ($J$-$V$) curves (symbols) in annealed P3HT/PCBM devices using bimolecular recombination (solid lines).

**Table 3.3** Simulation parameters on intensity dependent *J-V* curves of annealed P3HT/PCBM devices.

| Quantity | Symbol | Value |
|---|---|---|
| Dielectric constant | $\varepsilon$ | $3*10^{-13}$ F/cm |
| Effective band gap | $E_g$ | 1.05eV |
| Effective density of state | $N_c$, $N_v$ | $1*10^{20}cm^{-3}$ |
| Electron mobility | $\mu_n$, | $1*10^{-3}cm^2/Vs$ |
| Hole mobility | $\mu_p$ | $8*10^{-5}cm^2/Vs$ |
| $100mW/cm^2$ absorption rate | G | $8.2*10^{21}cm^{-3}s^{-1}$ |
| Thickness of active layer | $L$ | 100nm |

The bimolecular recombination rate used for the above simulation is $r_b = 1.14 * r_0$, in which $r_0$ is Langevin type bimolecular recombination rate as defined previously. Based on the simulation results in Figure 3.5, $\alpha$ should be smaller than one if bimolecular recombination rate was so large ($r_b$=1.14 $r_0$>>0.01$r_0$). Unfortunately, this phenomenon is not observed in our experimental study of intensity-dependent photocurrent in Figure 3.6.

Moreover, lots of fundamental studies such as time-of-flight [50] and transient absorption spectroscopy [58] revealed that the bimolecular recombination rate in BHJ OSCs is not Langevin-type but significantly suppressed ($10^{-2}$~$10^{-3}$ smaller) due to their specific configuration [43, 50]. Therefore, the large discrepancy between bimolecular recombination rate derived from the simulation and the value determined directly by the experiment also indicates that bimolecular recombination should not dominate in BHJ OSCs.

As discussed in Section 3.2, if bimolecular recombination dominates, the situation that $\alpha$ equals one can only occur at small recombination rate, which is corresponding to a high fill factor (FF>65% for all light intensities at 0.01*$r_0$ in Figure 3.5b, as indicated in Table 3.4). However, the fill factor of the annealed device (Figure 3.7) is no more than 50%,

which means that the recombination in our devices is not negligible. Therefore, for the annealed devices investigated herein, the fact that $\alpha$ equals one can imply that monomolecular recombination loss dominates. To verify this statement, we applied monomolecular recombination ($R_n = r_m * n$) to simulate *J-V* curves of the annealed P3HT/PCBM device as shown in Figure 3.8. The exact match between the simulations (solid lines) and experimental measurements (symbols) at all intensities verifies that monomolecular recombination is the primary loss mechanism in OSCs. In annealed devices, the carrier lifetime derived from the simulation is about $\tau = 1/r_m = 201$ ns. Based on the simulation results in Figure 3.7 and 3.8, the maximum deviation of the simulation results from experimental measurements is presented in Figure 3.9. A good fitting at one sun intensity for both recombination mechanisms is expected because all the parameters are extracted from this experimental curve. However, the deviation of simulation on bimolecular recombination becomes larger and larger as the intensity decreased; while the simulation based on monomolecular recombination matches the experiments with negligible deviation and the fitting error does not change significantly with variation of light intensity.

**Table 3.4** Fill factor at different light intensity for the simulated device with bimolecular recombination rate of $0.01r_0$ in Figure 3.5, annealed device in Figure 3.7, and non-annealed device in Figure 3.10.

| | $0.4I_0$ | $0.6I_0$ | $0.8I_0$ | $I_0$ | $1.2I_0$ |
|---|---|---|---|---|---|
| Simulation device ($0.01r_0$) | 83.4% | 72.8% | 71.5% | 70.4% | 69.5% |
| Annealed device | 45.1% | 44.2% | 43.6% | 42.3% | --- |
| Non-annealed device | 34.9% | 34.2% | 33.5% | 32.9% | --- |

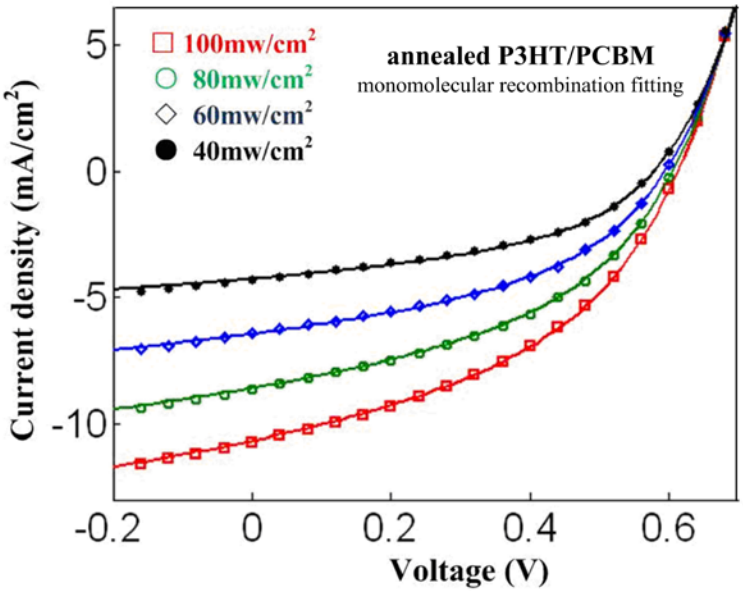


**Figure 3.8** Simulation of intensity-dependent current-voltage (*J*-*V*) curves (symbols) in annealed P3HT/PCBM devices using monomolecular recombination (solid lines).

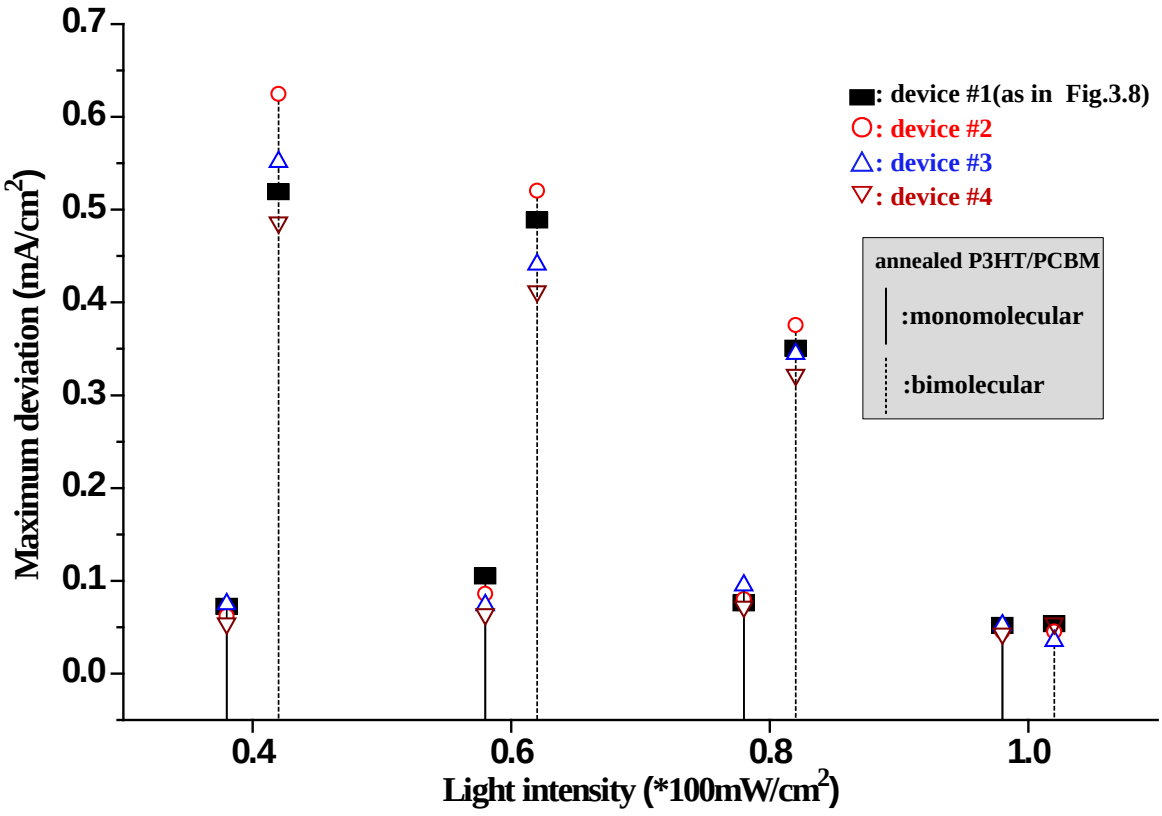


**Figure 3.9** The maximum deviation of the simulation results from experimental measurements of the annealed P3HT/PCBM devices. The solid black rectangle represents the device in Figure 3.8 and three other annealed devices are shown by hollow symbols.

To further verify the conclusion that monomolecular recombination dominates the performance of OSCs, similar studies on non-annealed devices also show that simulation results with monomolecular recombination (solid lines in Figure 3.10) fit experimental data well, but those using bimolecular recombination do not (dashed lines in Figure 3.10). The maximum deviation of the simulation from experimental results of the non-annealed devices is shown in Figure 3.11. The fitting parameters for the non-annealed devices are shown in Table 3.5. The thermal annealing of P3HT/PCBM devices not only increases carrier mobility but also enhances light absorption [32], which can be clearly seen by comparing Table 3.3

and 3.5. The carrier lifetime in the non-annealed device derived from the simulation is approximately $\tau = 1/r_m = 126$ ns, indicating that the monomolecular recombination rate in non-annealed devices is higher than that in annealed devices.

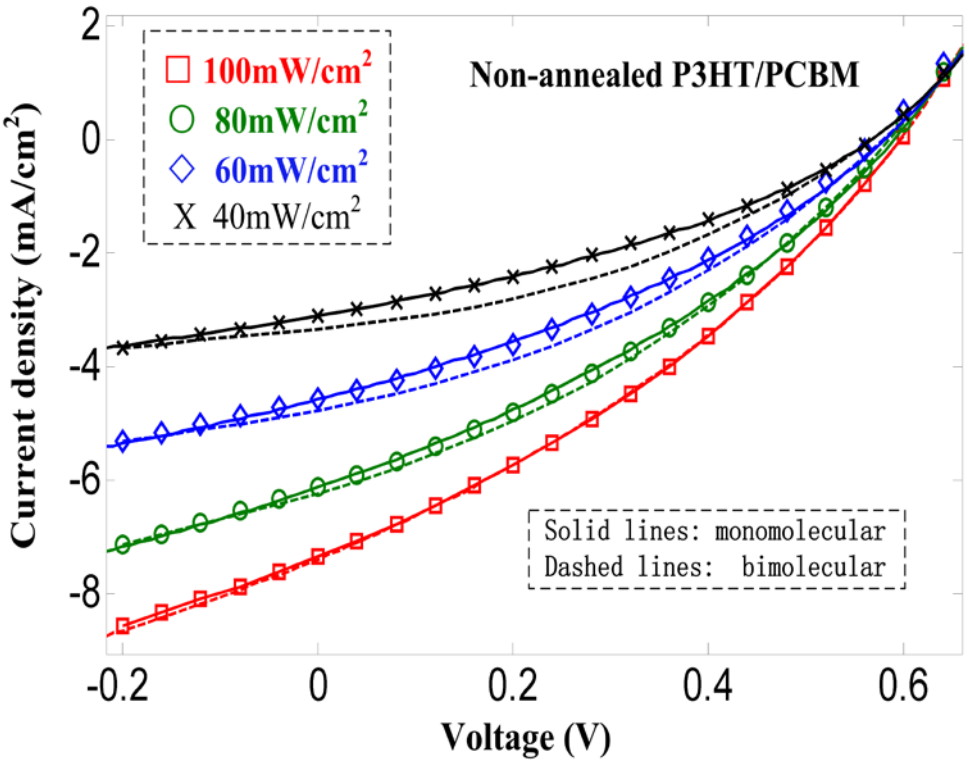


**Figure 3.10** Simulation of intensity-dependent current-voltage (*J-V*) curves (symbols) in non-annealed devices using monomolecular recombination (solid lines) and bimolecular recombination (dashed lines).

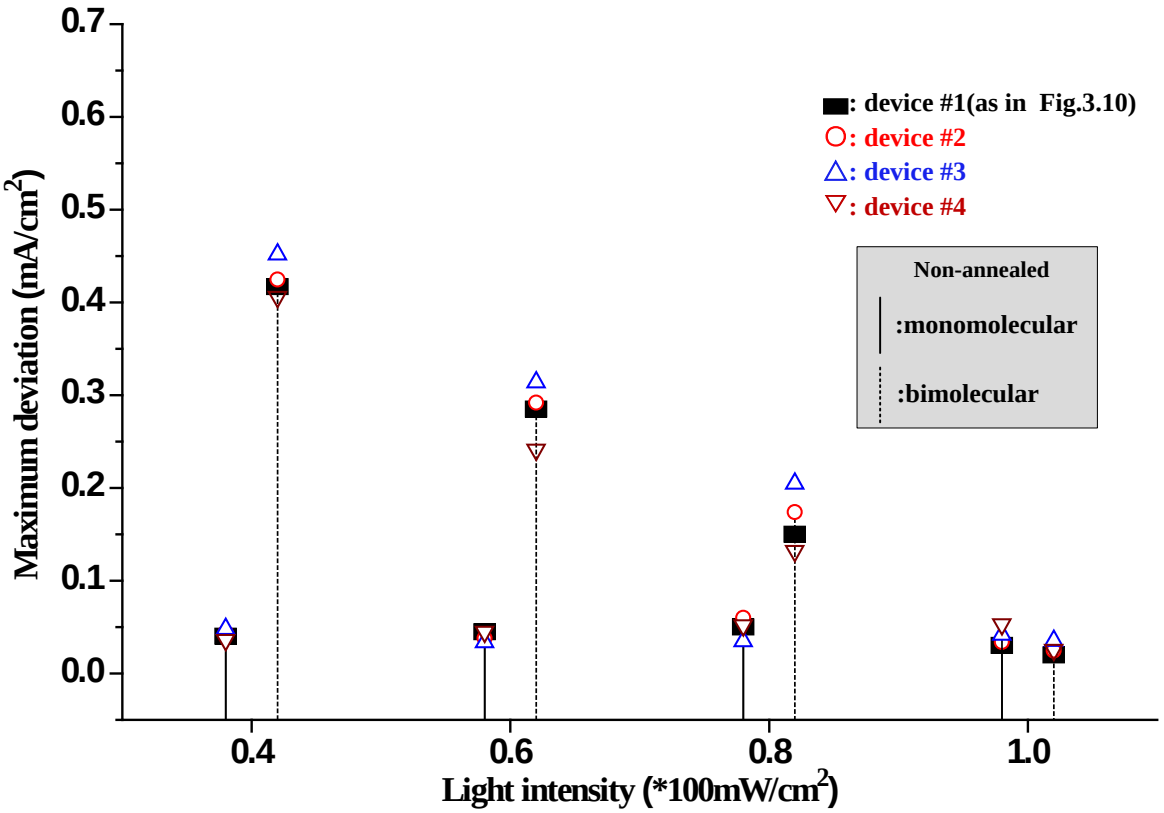


**Figure 3.11** The maximum deviation of the simulation from experimental results of the non-annealed P3HT/PCBM devices. The solid black rectangle represents the device in Figure 3.10 and three other non-annealed devices are shown by hollow symbols.

**Table 3.5** Simulation parameters on intensity dependent *J-V* curves of non-annealed P3HT/PCBM devices.

| Quantity | Symbol | Value |
|---|---|---|
| Dielectric constant | $\varepsilon_r$ | $3*10^{-13}$ F/cm |
| Effective band gap | $E_g$ | 1.05 eV |
| Effective density of state | $N_c$, $N_v$ | $1*10^{20}$ $cm^{-3}$ |
| Electron mobility | $\mu_n$, | $2.2*10^{-4}$ $cm^2/Vs$ |
| Hole mobility | $\mu_p$ | $1.2*10^{-6}$ $cm^2/Vs$ |
| $100mW/cm^2$ absorption rate | G | $6.5*10^{21}$ $cm^{-3}s^{-1}$ |
| Thickness of active layer | $L$ | 100 nm |

As mentioned in Chapter 2, classic Einstein relation ($D/\mu = kT/q$) might not be accurate for the disordered organic materials. The deviation of classical Einstein relation is owing to the property of disorder, which has been investigated by both experiment [59] and theoretical analysis [35]. In the generalized Einstein relation ($D/\mu = \beta * kT/q$) for OSCs, $\beta$ is a parameter related to the disorder and high value of $\beta$ implies high degree of disorder (in the case of solid-state materials, $\beta = 1$) [35]**.** For detailed mathematical derivation, refer to Appendix B. Simulations by $\beta = 1$ and $\beta = 2$ (disordered materials) are both performed to check the validity of using $\beta = 1$ in our simulation. It is found that with the change of $\beta$ from 1 to 2, if carrier mobility ($\mu$) and effective bandgap ($E_g$) are simultaneously tuned, the simulation still fits intensity dependent *J-V* experiments for both annealed and non-annealed devices, without changing the monomolecular recombination rate. It is well known that the intrinsic property of disorder in OSCs not only related to $\beta$ in the generalized Einstein relation, but also affects the carrier mobility [60] and effective bandgap [61]. Therefore, carrier mobility, effective bandgap ($E_g$) and degree of disorder are all correlated, which indicates that nano-morphology is very critical to the performance of OSCs. Herein, we only focus on the recombination mechanism. The nano-morphology is neglected for simplicity and will be further discussed in Section 7.2.

The simulation of intensity-dependent *J-V* curves demonstrates that instead of bimolecular recombination, monomolecular recombination dominates the performance of P3HT/PCBM OSCs. However, the fundamental physics mechanism to cause monomolecular recombination is still not clear at present and need to be further investigated in the future to improve the performance of OSCs. Currently, researchers think that there are two possible

reasons for the monomolecular recombination: First, geminate recombination of charge transfer excitons (CTEs); Second, interface state recombination due to the defects and trapping in the disordered organic materials.

If CTEs recombination accounts for the monomolecular loss, the reduced geminate recombination of CTEs through thermal annealing can be explained by the reduced interface area between donor and acceptor after thermal annealing, which decreases the possibility of CTEs' recombination at the interface. An alternative explanation, based on the Monte-Carlo simulation, is that the increased local carrier mobility within ordered domains after annealing facilitates the escape of carriers from CTEs and hence reduces the geminate recombination [62]**.** On the other hand, if interface state recombination dominates, the annealing of P3HT/PCBM OSCs improves the crystallization and nanoscale morphology of solar cells, which is proved by TEM and XRD [17]. Therefore, the ameliorated defects and trapping reduce the interface recombination in the annealed device. Whichever explanation is correct, the nanoscale morphology of donor/acceptor is clearly crucial to the performance of BHJ OSCs.

## 3.4 SUMMARY

By simulation, we have first proved that Langevin type bimolecular recombination is not proper to describe the loss mechanism in BHJ OSCs due to their unique properties. Then, intensity-dependent photocurrent is investigated by both simulation and theoretical analysis. It is concluded that the fact $\alpha$ =1 can not absolutely role out the situation that bimolecular

recombination dominate in BHJ OSCs. However, if the recombination is non-negligible, the fact that $\alpha$ =1 can guarantee that monomolecular recombination is the dominant loss. Finally, we have investigated the recombination mechanism in P3HT/PCBM BHJ OSCs by simulating intensity-dependent *J-V* curves for both annealed and non-annealed devices. By comparing simulation results with experimental data, we have found that monomolecular recombination loss dominates in BHJ OSCs. This finding is consistent with experimental results, which demonstrates that bimolecular recombination is significantly suppressed in BHJ OSCs. Further investigation of the physical mechanism to cause the monomolecular loss is indispensable and imperative to understanding BHJ OSCs more thoroughly and hence improving their performance.

# 4.0 PERFORMANCE OPTIMIZATION OF OSCS BY SIMULATION

By fitting simulation results to experimental *J-V* measurements, we have concluded that the dominant loss mechanism in BHJ OSCs is monomolecular recombination. The determination of recombination loss in BHJ OSCs improves the accuracy of simulation, and therefore it is feasible to find the optimal parameters for the best performance of OSCs through simulation study. In the following discussions, the developed simulation tools are applied to provide the guideline to optimize the performance of OSCs.

## 4.1 THICKNESS OPTIMIZATION

The thickness-dependent performance of OSCs has been experimentally investigated as shown in Figure 4.1. Five devices with active layer (P3HT/PCBM of 1:1 ratio by weight) of different thickness are fabricated by changing the spin speed. The thickness of active layer is acquired by AFM scanning in tapping mode. All other parameters remain the same for these five devices. It is observed that $V_{oc}$ remains almost the same for these five devices but $J_{sc}$ varies corresponding to the thickness of the active layer. It is obvious that there exists an optimal thickness around 85nm.

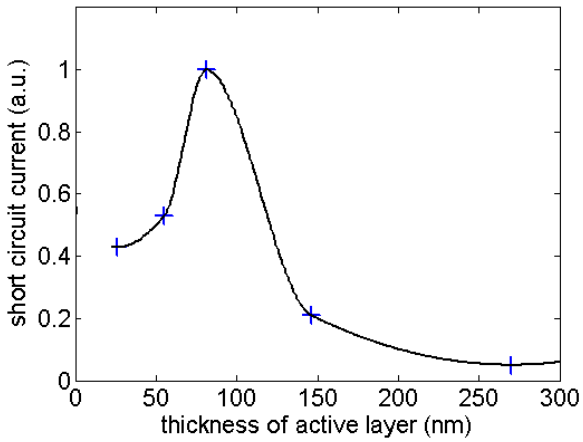


**Figure 4.1** Normalized $J_{SC}$ of P3HT/PCBM device as a function of the thickness of active layers.

PCE of solar cells can be represented as $\eta = \eta_A \eta_G \eta_C$ [63], in which $\eta_A$ is the absorption efficiency; $\eta_G$ is the exciton dissociation efficiency to describe how many absorbed photons can be separated to free carriers; $\eta_C$ is the charge collection efficiency, relating to the carrier mobility and recombination loss. For BHJ OSCs, the exciton dissociation is so sufficient that $\eta_G$ is close to 100% [25]. Therefore, PCE is mainly limited by the insufficient light absorption due to the thin active layer (low $\eta_A$) and the recombination loss due to the intrinsic properties in the disordered OSCs (low $\eta_C$). The absorption efficiency can be expressed by Beer-Lambert theory as:

$$\eta_A = I_a / I_0 = 1 - \exp(-d / L_A), \qquad \textbf{4.1}$$

where $I_a$ is the light absorbed by the active layer, $I_0$ is the illumination intensity, $d$ is the thickness of the active layer and $L_A$ is a constant named absorption length. It is necessary to point out that, for the first order approximation, the interference effect in the thin film device is not considered, which will be discussed later. When the thickness decreases from the optimal value, the decreased performance is due to the insufficient light absorption as the

light absorption decreased exponentially with respect to the thickness of the active layer. The charge collection efficiency $\eta_C$ is related to the carrier mobility. Carrier drift length is determined by the carrier mobility, life time and the electric field as

$$L = \mu\tau E . \qquad \textbf{4.2}$$

In order to obtain high collection efficiency $\eta_C$, the thickness of the active layer $d$ should be shorter than carrier drift length $L$ in order to prevent significant recombination loss [16]. For the thickness dependent measurement, if the thickness of the active layer is increased beyond the optimal situation, $\eta_A$ increases according to Eq.4.1. However, the increased thickness also makes $d < L$ not valid and thus $\eta_C$ decreases dramatically due to the insufficient extraction of the free carriers, which accounts for the decreased performance.

As discussed above, there exists a tradeoff between light absorption and carrier extraction in OSCs because of the slow carrier mobility (hopping and tunneling) in the disordered organic materials. Therefore, the thickness of active layer should be carefully optimized to improve the performance of OSCs.

### 4.1.1 Optical Transfer Matrix

To optimize the thickness of active layer, it is indispensable to precisely determine the light distribution as well as light absorption in the active layer. In general, Beer-Lambert Law type absorption is used to describe the light intensity in bulk materials, assuming exponential decay as $I(x)=I_0*\exp(-\alpha*x)$. $I(x)$ is the light intensity at position $x$, $I_0$ is the incident light intensity, $\alpha$ is absorption coefficient. However, light absorption in thin-film devices will be greatly affected by optical interference effect given that the thickness of each layer is

comparable with the light wavelength. Thus, optical transfer matrix theory will be applied to rigorously determine the optical electric field distribution in the thin-film device as a function of depth and light wavelength.

For the theory of optical transfer matrix, only light at normal incidence to the substrate is considered in the thin-film device. As the schematic in Figure 4.2, a plane wave was incident from left at a *m*-layers structure (layer 1 to layer *m*) between a semi-infinite transparent ambient and a semi-infinite substrate. Due to the optical interference in the thin-film device, the optical electric field at any point *x* in layer *j* is a complex quantity and consists of a positive component $E_j^+(x)$ and a negative component $E_j^-(x)$. The optical properties of each layer (*j*) are described by the complex index of refraction as $\tilde{n}_j = n_j + i\kappa_j$ and thickness $d_j$.

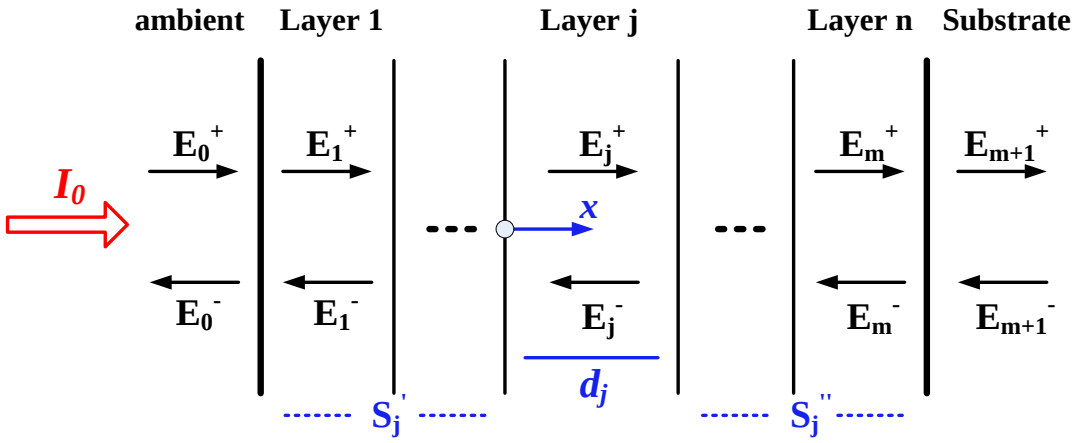


**Figure 4.2** Schematic of m-layers structure between ambient and substrate. The light is incident from the left, with intensity $I_0(\lambda)$ for different wavelength λ in the solar spectrum. Each layer j (j=1,2,…m) has a thickness $d_j$ and its optical properties are described by its complex index of refraction as $\tilde{n}_j = n_j + i\kappa_j$. The optical electric field at any point (*x*) in layer *j* is represented by two components: one propagating in the positive direction ($E_j^+$, left to right) and one in the negative direction ($E_j^-$, right to left).

Two special cases need to be carefully considered in the theory of optical transfer matrix: First is the light behavior at the interface between adjacent layers (interface matrix $\boldsymbol{I_{jk}}$); second is the light propagating in each layer (layer matrix $\boldsymbol{L_j}$). The light behavior at the interface between $j$ and $k=j+1$ layers can be described by a 2x2 matrix containing the complex Fresnel coefficients. The interface matrix $\boldsymbol{I_{jk}}$ can be expressed as:

$$I_{jk} = \begin{bmatrix} (\tilde{n}_j + \tilde{n}_k)/2\tilde{n}_j & (\tilde{n}_j - \tilde{n}_k)/2\tilde{n}_j \\ (\tilde{n}_j - \tilde{n}_k)/2\tilde{n}_j & (\tilde{n}_j + \tilde{n}_k)/2\tilde{n}_j \end{bmatrix}. \qquad \textbf{4.3}$$

The light propagating in layer $j$ can be described by the layer matrix $\boldsymbol{L_j}$ as:

$$L_j = \begin{bmatrix} \exp(-i\frac{2\pi\tilde{n}_j}{\lambda}\cdot d_j) & 0 \\ 0 & \exp(-i\frac{2\pi\tilde{n}_j}{\lambda}\cdot d_j) \end{bmatrix} = \begin{bmatrix} \exp(-ik_j\cdot d_j) & 0 \\ 0 & \exp(-ik_j\cdot d_j) \end{bmatrix}, \qquad \textbf{4.4}$$

in which, wave number $k_j = \frac{2\pi\tilde{n}_j}{\lambda}$. From layer matrix $\boldsymbol{L_j}$, it is clear that the real part of complex refraction ($n_j$) is response for the phase propagation and image part of complex refraction ($\kappa_j$) is related to the light absorption. The optical electric field in the ambient (subscript 0) is related to that in the substrate (subscript $m+1$) by the total transfer matrix $\boldsymbol{S}$:

$$\begin{bmatrix} E_0^+ \\ E_0^- \end{bmatrix} = S\begin{bmatrix} E_{m+1}^+ \\ E_{m+1}^- \end{bmatrix}, \qquad \textbf{4.5}$$

in which the total optical transfer matrix $\boldsymbol{S}$ is the product of all interface and layer matrices as:

$$S = \begin{bmatrix} S_{11} & S_{12} \\ S_{21} & S_{22} \end{bmatrix} = \left(\prod_{v=1}^{m} I_{(v-1)v}L_v\right)I_{m(m+1)}. \qquad \textbf{4.6}$$

The electric field at a distance $x$ within layer $j$ (Figure 4.2) can be expressed as:

$$E_j(x) = E_j^+(x) + E_j^-(x). \qquad \textbf{4.7}$$

To express $E_j(x)$ in term of known quantities, Eq 4.6 is split into two partial transfer matrices $S_j^{'}$ and $S_j^{''}$ as in Figure 4.2, $S = S_j^{'}L_jS_j^{''}$. These two matrices can be expressed as:

$$S_j^{'} = \begin{bmatrix} S_{j11}^{'} & S_{j12}^{'} \\ S_{j21}^{'} & S_{j22}^{'} \end{bmatrix} = \left( \prod_{v=1}^{j-1} I_{(v-1)v} L_v \right) I_{(j-1)j}, \quad \textbf{4.8}$$

$$S_j^{''} = \begin{bmatrix} S_{j11}^{''} & S_{j12}^{''} \\ S_{j21}^{''} & S_{j22}^{''} \end{bmatrix} = \left( \prod_{v=j+1}^{m} I_{(v-1)v} L_v \right) I_{m(m+1)}. \quad \textbf{4.9}$$

The electric field in layer *j* can be expressed by the partial system as:

$$\begin{bmatrix} E_0^+ \\ E_0^- \end{bmatrix} = S_j^{'} \begin{bmatrix} E_j^{'+} \\ E_j^{'-} \end{bmatrix}, \quad \textbf{4.10}$$

$$\begin{bmatrix} E_j^{''+} \\ E_j^{''-} \end{bmatrix} = S_j^{''} \begin{bmatrix} E_{m+1}^+ \\ E_{m+1}^- \end{bmatrix}, \quad \textbf{4.11}$$

in which, $E_j^{'+}$ and $E_j^{'-}$ refer to the left boundary *(j-1)j* in layer *j*. $E_j^{''+}$ and $E_j^{''-}$ refer to the right boundary *j(j+1)* in layer *j*. After algebraic manipulation, Eq. 4.7 can be rewritten as:

$$E_j(x) = E_j^+(x) + E_j^-(x) = t_j^+ \left[ e^{ik_j x} + r_j^{''} e^{ik_j(2d_j - x)} \right] E_0^+, \quad \textbf{4.12}$$

in which, $E_0^+$ is the electric field of the incident light from the ambient.

$$t_j^+ = [S_{j11}^{'} + S_{j12}^{'} r_j^{''} e^{2ik_j d_j}]^{-1}, \quad \textbf{4.13}$$

$$r_j^{''} = S_{j21}^{''} / S_{j11}^{''}. \quad \textbf{4.14}$$

For the detailed derivation, please refer to [64].

After determining the distribution of optical electric field $E_j(x)$ in layer *j* as Eq.4.12, the light intensity at a distance *x* within layer *j* of the device can be expressed as:

$$I_j(x,\lambda) = T_j I_0(\lambda) \left[ e^{-\alpha_j x} + \rho_j^{''2} \cdot e^{-\alpha_j(2d_j - x)} + 2\rho_j^{''} \cdot e^{-\alpha_j d_j} \cdot \cos\left(\frac{4\pi n_j}{\lambda}(d_j - x) + \delta_j^{''}\right) \right], \quad \textbf{4.15}$$

where $I_0(\lambda)$ is the intensity of the incident light, $T_j = (n_j / n_0)\left|t_j^+\right|^2$ is the internal intensity transmittance, and $\rho_j^{''}$ and $\delta_j^{''}$ are the absolute value and the argument of the complex reflection coefficient for the second subsystem given by Eq 4.14. $n_j$ is the real part of refractive index, and $\alpha_j$ is the absorption coefficient as $\alpha_j = 4\pi\kappa_j / \lambda$.

The first term of Eq 4.15 on the right hand side originates from the optical electric field propagating in the positive *x* direction $E_j^+(x)$, the second term from the field propagating in the negative *x* direction $E_j^-(x)$, and the third term is due to optical interference of the first two terms. The third term becomes especially important when the thickness of thin film is comparable with the light wavelength ($e^{-\alpha_j d_j}$ is not negligible). As the thickness of active layer is much larger than the light wavelength ($d_j >> \lambda$, $e^{-\alpha_j d_j} << 1$), second term and third term will be approximately zero and only the first term dominates. Mathematically, when $d_j >> \lambda$,

$$I_j(x) = T_j I_0 \left[ e^{-\alpha_j x} + \rho_j^{''2} \cdot e^{-\alpha_j (2d_j - x)} + 2\rho_j^{''} \cdot e^{-\alpha_j d_j} \cdot \cos\left(\frac{4\pi n_j}{\lambda}(d_j - x) + \delta_j^{''}\right) \right] \approx T_j I_0 e^{-\alpha_j x} \propto I_0 e^{-\alpha_j x} \quad \textbf{4.16}$$

which is Beer-Lambert Law type absorption for bulk materials.

Once the distribution of light intensity in the active layer is determined, the rate of energy dissipated per unit volume Q can be determined as:

$$Q(x,\lambda) = \alpha(\lambda) I(x,\lambda). \quad \textbf{4.17}$$

Then, the density of photon absorbed in the active layer is:

$$n(x) = \int_{350}^{800} \frac{\lambda}{hc} Q(x,\lambda) d\lambda. \quad \textbf{4.18}$$

where *h* is Planck's constant. The integration is performed from 350nm to 800nm because glass absorbs strongly below 350nm and active layer of P3HT/PCBM seldom absorbs light beyond 800nm due to the relative high bandgap of conjugated polymer (~2eV).

### 4.1.2 Solar Spectrum

The energy flow within the sun results in a surface temperature of around 5800K, so the radiation spectrum from the sun is similar to 5800K blackbody radiation. The radiation power density of black body radiation can be expressed as:

$$I(\lambda,T)=\frac{2\pi hc^2}{\lambda^5}\cdot\frac{1}{\exp(hc/\lambda kT)-1}, \qquad \textbf{4.19}$$

in which, $\lambda$ is wavelength, $h$ is plank's constant, $c$ is light velocity in vacuum and $kT$ is thermal energy. The radiation power density of the sun on the external atmosphere of the earth (without considering absorption of the earth atmosphere) is:

$$I(\lambda,5800)=\frac{2\pi hc^2}{\lambda^5}\cdot\frac{1}{\exp(hc/\lambda k*5800K)-1}\cdot(\frac{r_s}{d_{SE}})^2, \qquad \textbf{4.20}$$

in which, $r_s$ is radius of the sun and $d_{SE}$ is the distance between the sun and the earth. $r_s$=6.96*$10^8$m, $d_{SE}$=1.496*$10^{11}$m.

For the characterization of ordinary OSCs on the earth, the incident spectrum AM 1.5 global is always used because the earth atmosphere absorbs incident light with certain wavelength, which results in the deviation of solar spectrum on the earth from 5800K black body radiation, as indicated in Figure 4.3. In the following study, we will use AM 1.5 global spectrum (red curve, certificated by the National Renewable Energy Laboratory), in which there are some distinct features corresponding to the specific absorption of the earth atmosphere.

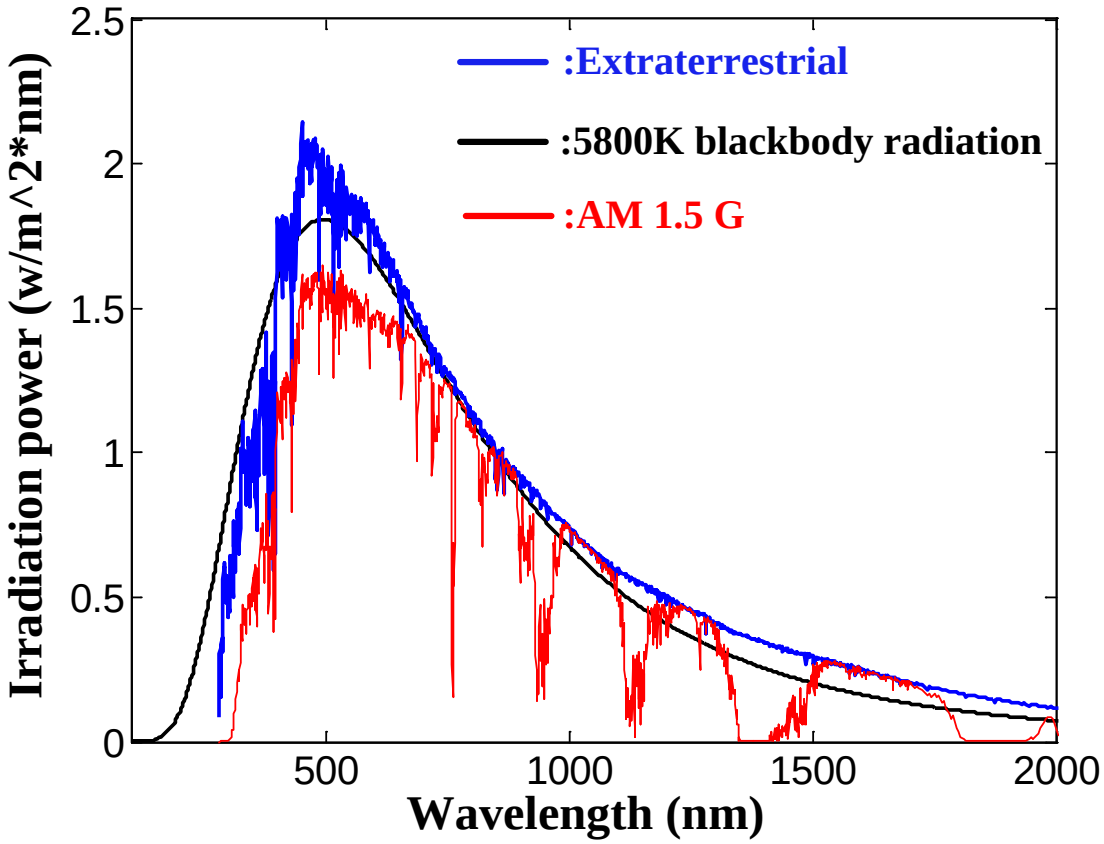


**Figure 4.3** Solar spectrum. Blue curve is extraterrestrial measurement data, black is calculation based on 5800K blackbody radiation, and red curve represents AM 1.5G spectrum [65].

### 4.1.3 Thickness-Dependent Performance of P3HT/PCBM Solar Cells

The configuration of OSCs is: Glass/ITO (120nm)/PEDOT:PSS (30nm) /P3HT_PCBM/Al(100nm). The real part and imaginary part of complex refraction for different materials are shown in Figure 4.4 [66].

First, we used Eq 4.15-4.18 to calculate the photon absorption in P3HT/PCBM layer as a function of thickness for two different incident wavelengths (350nm, 500nm). There are mainly three observations in Figure 4.5. First, when the thickness of active layer is small (<500nm), there exists strong oscillation features arising from the interference effect as discussed above, while the oscillation gradually diminished when the thickness of active layer increases up to 800nm; Second, the oscillation period for the incident light with 350nm wavelength is shorter (peak to peak oscillation is about 100nm) compared with 550nm incident light (peak to peak oscillation is about 135nm), because enhanced interference distance (*d*) for a single thin film should be quarter wavelength as $d=1/4*\lambda$; Third, the light absorption with 550nm wavelength (red curves in Figure 4.5) is more sufficient compared with the absorption of 350 nm due to higher absorption coefficient of P3HT/PCBM at 550nm as shown in Figure 4.4b.

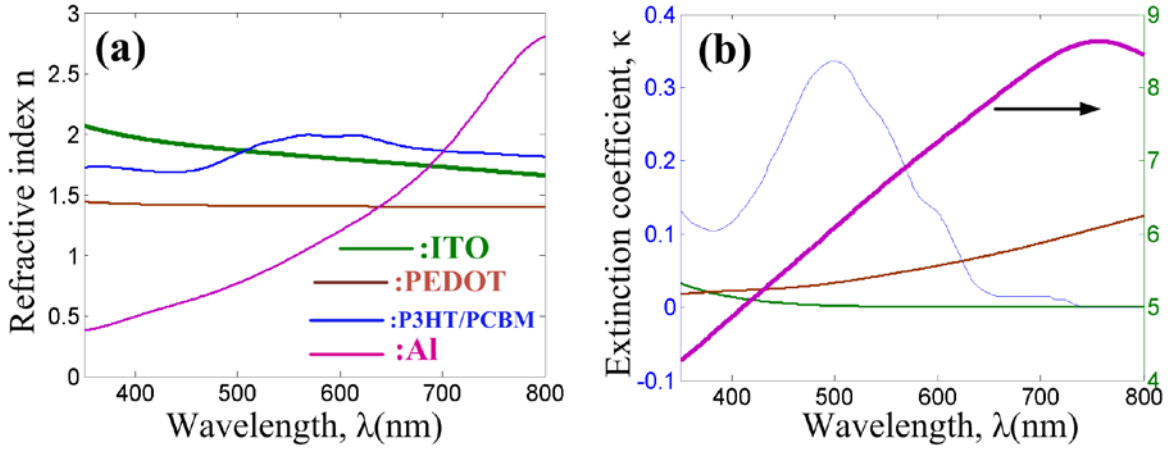


**Figure 4.4** The optical constants of materials used in simulation: (a) refractive indices *n*, real part of complex index of refraction. (b) extinction coefficients, imaginary part of complex index of refraction [66].

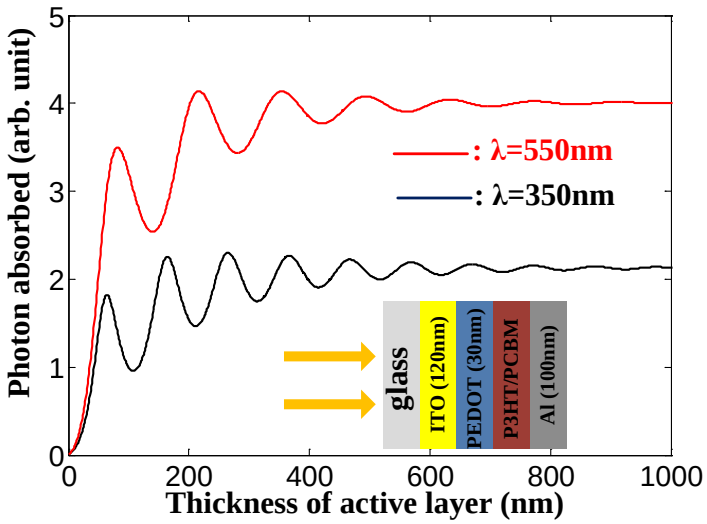


**Figure 4.5** Calculated photons absorbed in P3HT/PCBM active layer versus the thickness of active layer for incident light with different wavelength (350nm, 500nm).

Then, the photon absorption versus thickness of active layer (P3HT/PCBM) was calculated for AM 1.5G solar spectrum as shown in Figure 4.6. It is clear that there does exist optical interference effect if optical transfer matrix method (red curve) is used and as the

result, the absorption is enhanced at certain thickness compared with exponential decay of incident intensity calculated by Beer-Lambert theory (black curve). The inset of Figure 4.6 shows that the absorbed photon calculated by both methods (optical transfer matrix & Beer-Lambert theory) converged when the thickness of active layer increases up to 1000nm, as we discussed before (Eq 4.16). The simulation in Figure 4.6 indicates that the optimal thickness of active layer is around 90nm for P3HT/PCBM OSCs, which is in coincidence with our experimental results in Figure 4.1, which shows that P3HT/PCBM device with 88nm thickness has the best performance.

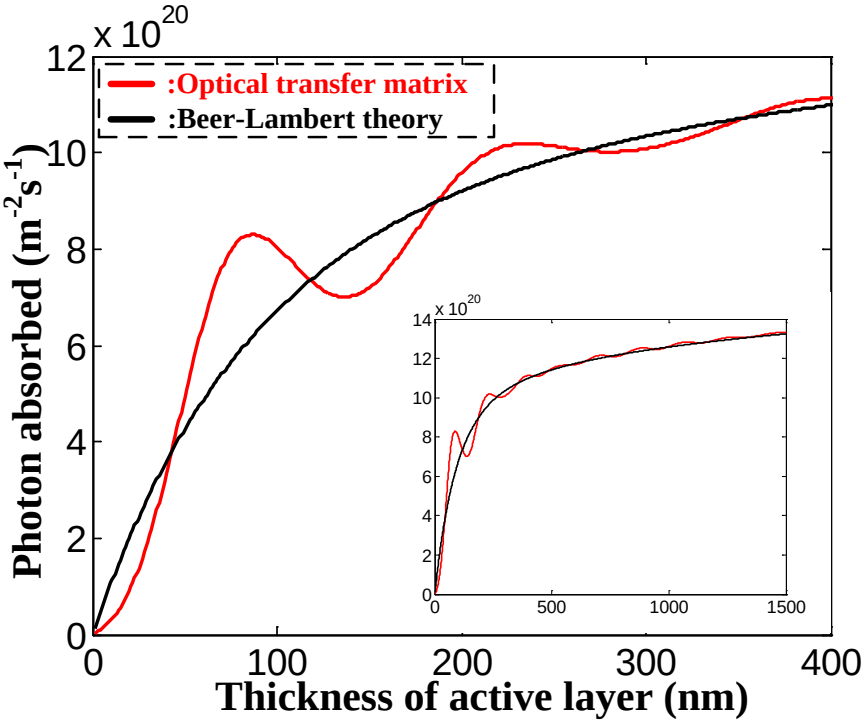


**Figure 4.6** Calculated photons absorbed of AM1.5G solar spectrums in P3HT/PCBM active layer versus the its thickness based on optical transfer matrix (red curve, Eq 4.15) and Beer-Lambert theory (black curve), describing exponential decay of light intensity as $I(x)=I_0*\exp(-\alpha*x)$.

To clearly see the interference effect from the aspect of the optical electric field, let us focus on the first peak in Figure 4.5. The optical electric field for 87nm thickness device (first peak) at 500nm incident light is calculated based on both optical transfer matrix and Beer-Lambert theory as shown in Figure 4.7. The incident optical electric field is $E_0$ at 500nm. The electric field is bigger than incident field $E_0$ due to the enhanced interference. However, the electric field in the active layer is underestimated if Beer-Lambert method is used.

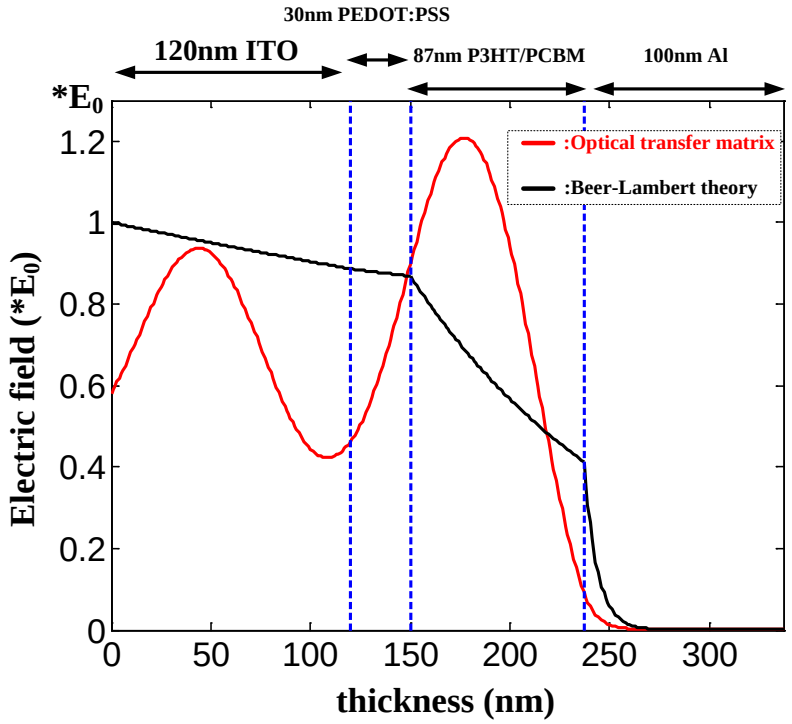


**Figure 4.7** Distribution of optical electric field in ITO/PEDOT:PSS/P3HT:PCBM/Al OSCs. Wavelength of incident light is 500nm and electric field is $E_0$. The thickness of active layer is 87nm. Optical transfer matrix theory is used in red curve and black curve is based on Beer-Lambert theory.

After determining the optical electric field and photon absorption under AM 1.5G solar spectrum in the thin-film OSCs using optical transfer matrix, we are able to optimize the thickness of OSCs by simulating *J-V* curves for devices with different thickness and then extracting parameters such as $J_{sc}$, $V_{oc}$, fill factor (*FF*) and PCE as a function of the thickness of the active layer. The simulation results are shown in Figure 4.8 for P3HT/PCBM solar cell devices with different post-treatments: as-casted (black curve), thermal annealed at 70$^{o}$C (blue curve) and annealed at 140$^{o}$C for half hour (red curve), respectively. It is well known that thermal annealing of P3HT/PCBM improves the crystallization of P3HT and hence increases the carrier mobility as indicated in Table 4.1 [32]. Thickness dependent PCE is shown in Figure 4.8a. There are two observations: First, PCE increases with the increase of carrier mobility, irrespective of the thickness of the active layer; Second, with the increase of carrier mobility, the thickness at which PCE get maximum value increased as indicated by the arrow in the inset because high carrier mobility can guarantee sufficient carrier extraction when increasing the thickness. $J_{sc}$ is shown in Figure 4.8b. The blue dashed curve represents the maximum $J_{sc}$ assuming the internal quantum efficiency is 100%, which is calculated by the optical transfer matrix discussed above. For red curve, it is clear that when the thickness is smaller than 150nm, charge collection is efficient comparing with the maximum current density. However, $J_{sc}$ is much smaller for slower carrier mobility because of increased recombination loss and hence the insufficient carrier extraction. $V_{oc}$ in Figure 4.8c are almost the same, which is mainly determined by the difference between HOMO of donor (P3HT) and LUMO of acceptor (PCBM). The fill factor is shown in Figure 4.8d. Therefore, compared with the other two devices, the increased performance of the device annealed at

140°C is mainly due to the increased carrier mobility, which can be observed from the increased $J_{sc}$ and $FF$.

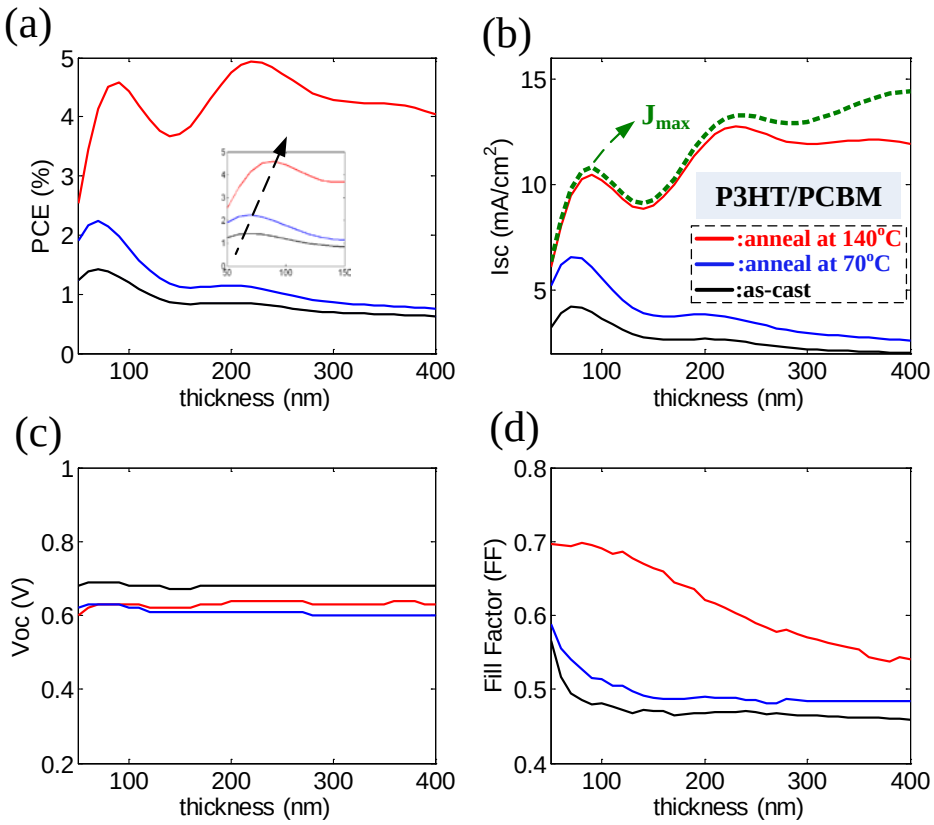


**Figure 4.8** Thickness dependent power conversion efficiency PCE (a), short circuit current $J_{sc}$ (b), open circuit voltage $V_{oc}$ (c) and fill factor (d) for P3HT/PCBM solar cells as prepared (black curve), annealed at 70°C (blue curve) and annealed at 140°C (red curve), respectively.

**Table 4.1** Carrier mobility for the simulation in Figure 4.8.

| Device | $\mu_n$ ($cm^2$/Vs) | $\mu_p$ ($cm^2$/Vs) |
|---|---|---|
| as-cast | $2*10^{-4}$ | $4*10^{-8}$ |
| annealed at 70°C | $1*10^{-3}$ | $1*10^{-6}$ |
| annealed at 140°C | $2.5*10^{-3}$ | $3*10^{-4}$ |

## 4.2 LOWERING BANDGAP OF CONJUGATED POLYMER

The simulation in Figure 4.8 indicates that increasing the carrier mobility and optimizing the thickness of active layer are two efficient methods to improve the performance of OSCs. However, the mobility for the annealed P3HT/PCBM device at 140$^{o}$C almost reached theoretical maximum value in their pristine phase [32] and therefore, there is not too much space to increase the mobility. Moreover, for the device annealed at 140$^{o}$C, at the optimal thickness (100nm), the extraction of photoexcited carrier is efficient (Figure 4.8b) and recombination loss is negligible (Figure 4.8d, FF>65%). The theoretical maximum PCE of P3HT/PCBM is no more than 5% as indicated in Figure 4.8a and unfortunately, there is not too much space to further increase PCE based on P3HT/PCBM devices.

In order to be commercialized, PCE of OSCs should be increased up to 10%. Therefore, besides increasing carrier mobility and optimizing the thickness of the active layer, we should explore other method to further improve the performance of OSCs. Shockley had already calculated that the optimal bandgap for the solar cell is around 1.5ev in 1961 [6]. High bandgap in P3HT (~2eV) prevents the absorption of the solar spectrum beyond 650nm (Figure 4.4b). Therefore, lowering the bandgap of conjugated polymer seems like a feasible and promising alternative to enhance the light absorption and further increase PCE of OSCs.

As a candidate for new low-bandgap conjugated polymer materials, PCPDTBT (the chemical structure is in Figure 1.3) is receiving more and more attention recently due to its ideal bandgap, excellent absorption and excellent electrical properties [21]. The optical bandgap of PCPDTBT is about $E_g$~1.5eV, which can extend the absorption into infrared region (~850nm) as shown by blue curve in Figure 4.9a. Because of insufficient absorption of the solar spectrum with the wavelength between 400nm to 600nm for PCPDTBT/$PC_{60}BM$, $PC_{70}BM$ is used as acceptor materials to increase the absorption from 400nm to 600nm wavelength, which is clear by comparing the blue and red curves. Based on the extinction coefficient in Figure 4.9a, the thickness-dependent maximum absorptions are calculated based on the optical transfer matrix. The result is shown in Figure 4.9b, which clearly validates that lowering the bandgap is an effective way to increase light absorption.

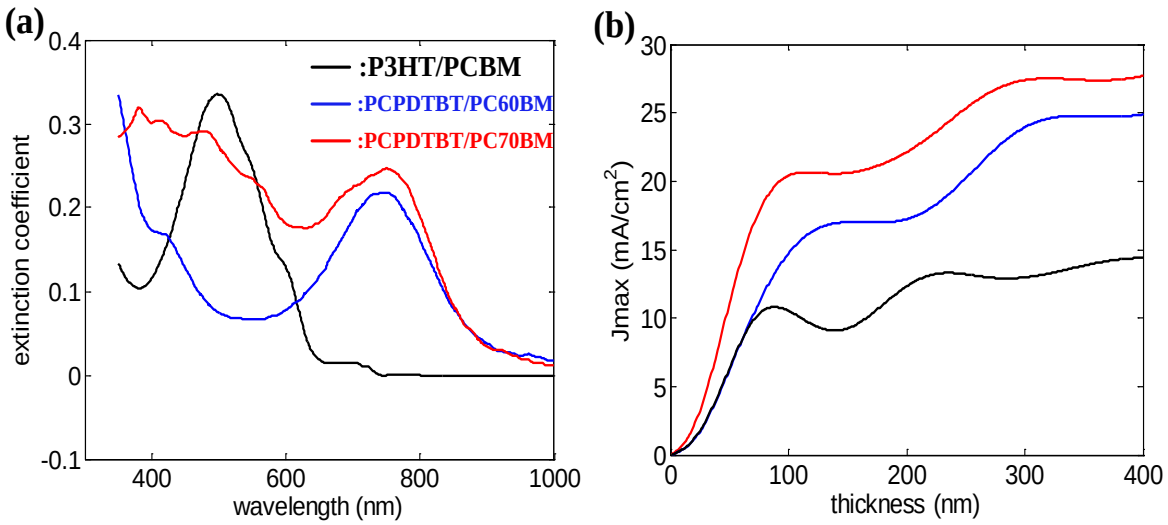


**Figure 4.9** (a) extinction coefficient of P3HT/PCBM (black), PCPDTBT/PC60BM (blue) and PCPDTBT/PC70BM (red) as a function of light wavelength. (b) thickness dependent maximum photocurrent under AM1.5 spectrum for P3HT/PCBM (black), PCPDTBT/PC60BM (blue) and PCPDTBT/$PC_{70}BM$ (red).

To further verify that lowering the bandgap of conjugated polymer is an effective method to increase light absorption, the light wavelength dependent absorbance is calculated as shown in Figure 4.10. The thickness of active layer is fixed at 100nm, which is a reasonable value for OSCs. It is clear that lowering the bandgap of conjugated polymer (PCPDTBT/$PC_{60}BM$, blue curve) extends the light absorption of P3HT/PCBM (black curve) from 700nm to 900nm wavelength. Compared with $PC_{60}BM$, $PC_{70}BM$ is able to enhance the light absorption from 400nm to 600nm wavelength (red curve).

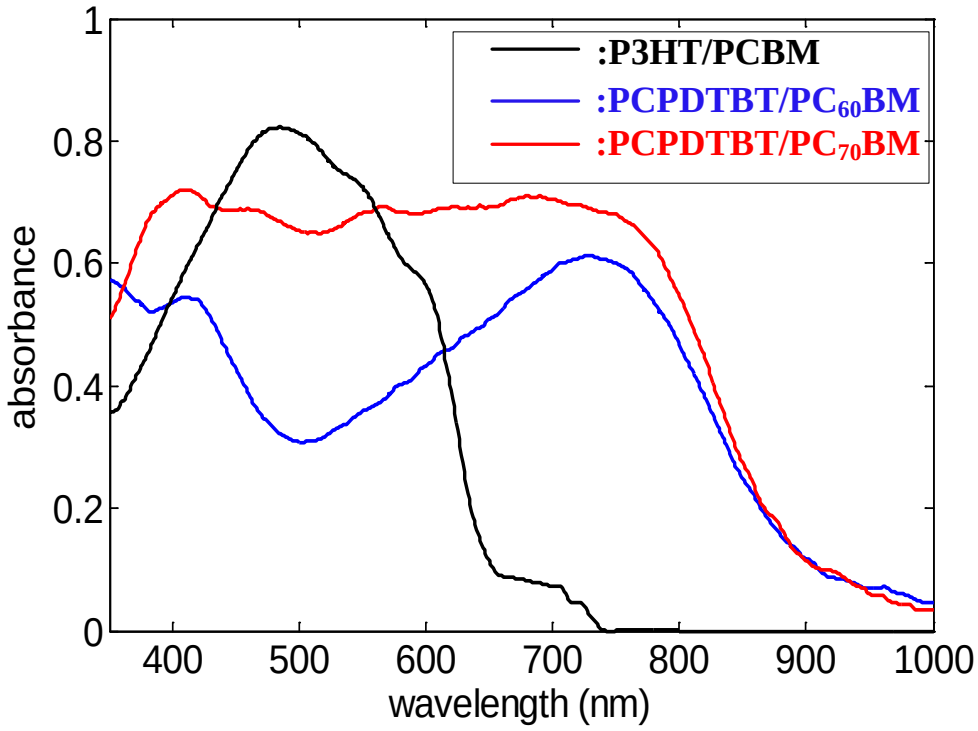


**Figure 4.10** Light wavelength dependent absorption with active layer of 100nm thickness for P3HT/PCBM (black), PCPDTBT/PC60BM (blue), and PCPDTBT/PC70BM (red).

We tried the similar procedure to optimize the performance of OSCs as shown in Figure 4.11. The solid line is for PCPDTBT/$PC_{70}BM$ with actual mobility while the dashed line represents the maximum electron mobility in pure $PC_{70}BM$ phase and hole mobility in pure PCPDTBT phase. The value of mobility can be found in Table 4.2. The increased mobility results that the PCE increases from 3.8% to 5.5%, which is still far below 10%. Therefore, increasing the carrier mobility is not an effective method to optimize PCPDTBT/$PC_{70}BM$ solar cells because the recombination loss in this type device is very high, which can be seen from the relatively small fill factor (for the device with ideal maximum mobility, FF=50% at optimal performance). The lifetime in the simulation is 0.3 $\mu s$, which is two orders smaller than the optimized lifetime of P3HT/PCBM solar cells (50 $\mu s$) [67].

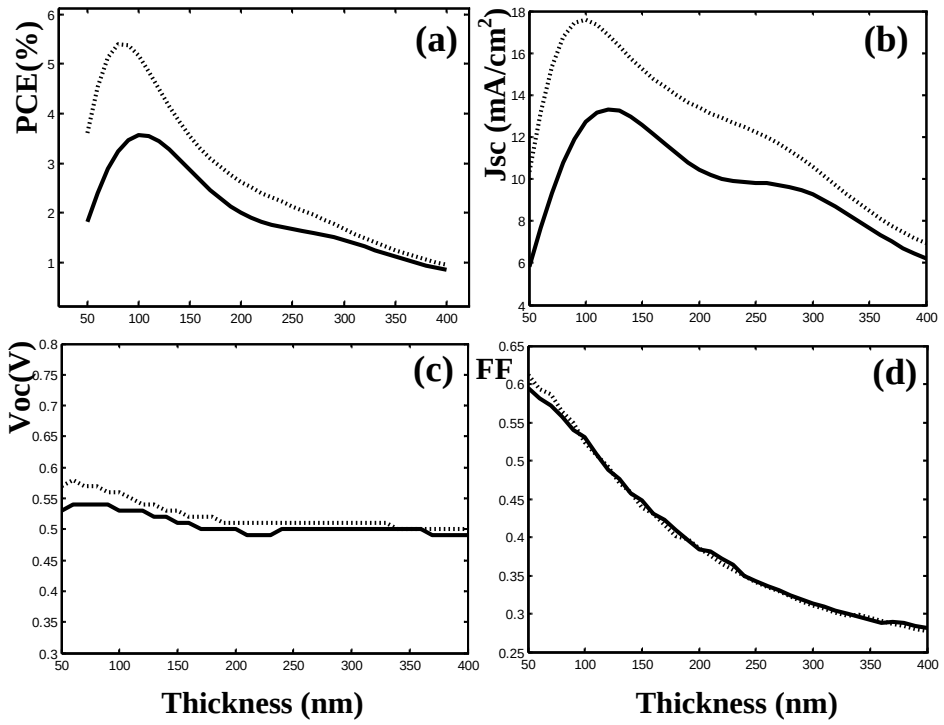


**Figure 4.11** Thickness dependent power conversion efficiency (a), short circuit current (b), open circuit voltage (c), and fill factor (d) for PCPDTBT/$PC_{70}BM$ with actual carrier mobility (solid line) and ideal maximum carrier mobility (dashed line) [68, 69].

**Table 4.2** Carrier mobility for the simulation of PCPDTBT/PCBM solar cells.

| mobility | $\mu_n$ ($cm^2$/Vs) | $\mu_p$ ($cm^2$/Vs) |
|---|---|---|
| actual value | $3*10^{-4}$ | $8*10^{-4}$ |
| maximum value | $5.5*10^{-4}$ | $2*10^{-3}$ |

Therefore, instead of increasing the carrier mobility, we simulated the effect of reducing recombination loss as shown in Figure 4.12. The black curve is for the actual recombination loss (life time is 0.3$\mu s$) right now. The reduced recombination with life time of 3$\mu s$ and 30$\mu s$ are represented by blue curve and red curve, respectively. The lifetime of red curve is comparable to P3HT/PCBM. The simulation indicates that decreasing the recombination loss is an effective

way to optimize the performance of OSCs. As shown in Figure 4.12a, if the recombination loss could be reduced as similar to P3HT/PCBM solar cells, PCE could be increased up to 10% at around 100nm thickness. The reduced recombination can increase $J_{sc}$ as shown in Figure 4.12b as well as fill factor in Figure 4.12d as we expected. It is necessary to point out that the reduced recombination can also increase $V_{oc}$ as we discussed before. Therefore, for PCPDTBT/PCBM solar cells, reducing the recombination loss is an effective way to optimize its performance. Right now, researchers found that adding some additive besides PCPDTBT/PCBM will increase the nanomorphology and hence reduced the recombination loss. However, the reduction of recombination loss is not so significant and the fill factor of PCPDTBT/PCBM solar cells is only about 55% [70]. It is imperative to find new method to improve the nanomorphology in order to decrease the recombination loss and hence optimize the performance of OSCs.

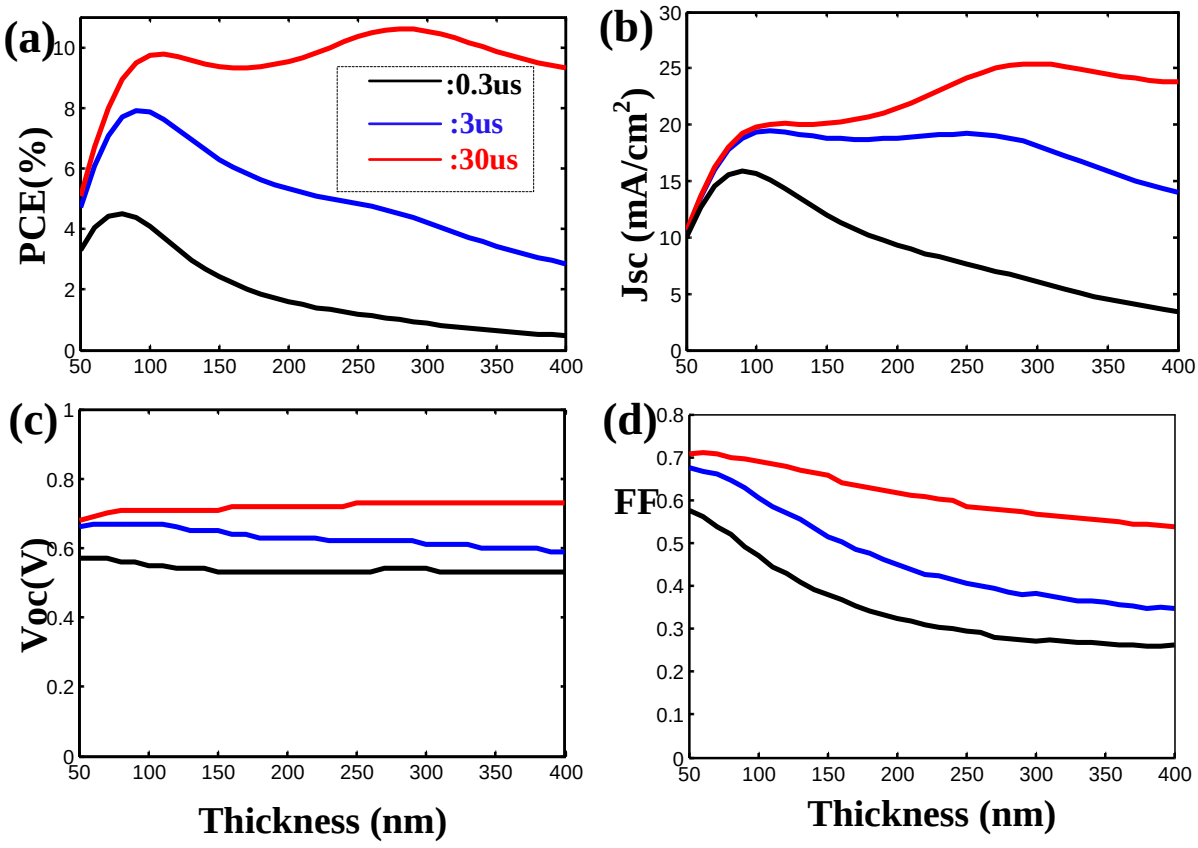


**Figure 4.12** Thickness dependent power conversion efficiency (a), short circuit current (b), open circuit voltage (c), and fill factor (d) for PCPDTBT/PC70BM with life time of 0.3$\mu s$ (black curve), 3$\mu s$ (blue curve) and 30$\mu s$ (red curve). The simulation indicates that reducing recombination loss is an effective method to increase performance of PCPDTBT/PCBM solar cells.

## 4.3 BALANCING CARRIER TRANSPORT IN OSCS

It is well known that electron mobility in the fullerene derivatives (acceptor) is faster compared with hole mobility in the conjugated polymer (donor) even after thermal annealing [32], which results the unbalanced carrier transport [18]. The unbalanced carrier transport is detrimental to

extraction of photoexcited carriers and hence limits PCE, which is simulated in Figure 4.13. It is clear that $J_{sc}$ and fill factor are all reduced (dash line) compared with the situation of balanced carrier transport (solid line) because of the unbalanced carrier transport.

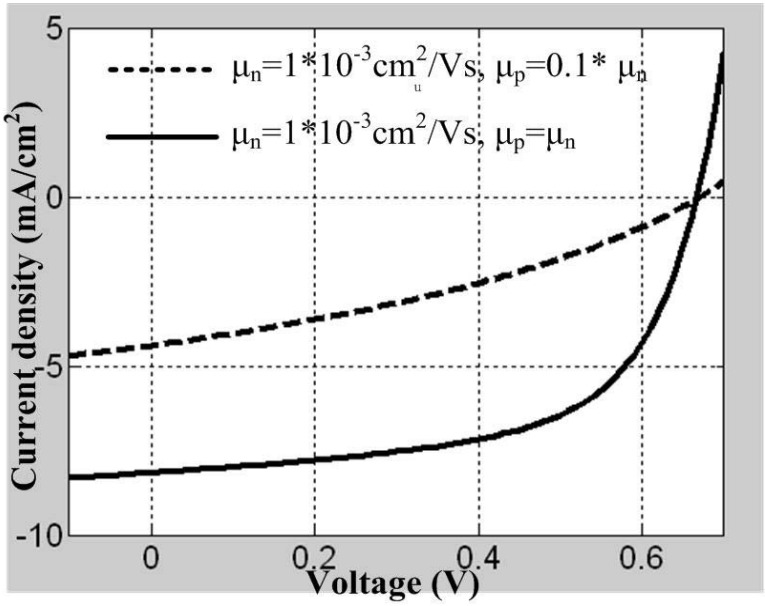


**Figure 4.13** Simulation of the detrimental effect due to unbalanced carrier transport. Dash line represents the situation where hole mobility is one order slower than electron mobility and solid line is for the balanced carrier transport where electron and hole mobility is the same.

For OSCs with the disordered nanomorphology, low carrier mobility is a main factor to limit the power conversion efficiency. If one kind of carriers (electrons in acceptor phase) has much larger mobility compared with the other (holes in donor phase), the slower carriers (holes) can not be fully extracted, resulting space charge limited current. The effect of space charge is simulated in Figure 4.14 and the parameters are the same as in Figure 4.8. The carrier density of electrons and holes versus position are calculated at short circuit current (applied voltage is zero). It is clear that if electron and hole has similar mobility (solid line), the extraction of electrons and

holes is balanced. However, if hole mobility is one order smaller compared with electron mobility, there is space charge (holes) near the anode which can not be fully extracted. There are two detrimental effects of this space charge near the anodes: First, the space charge will reduce the built-in electric field and thus impede the efficient carrier extraction; Second, the space charge near the anode will increase the carrier recombination between the active layer and the electrode and hence significantly decreases the performance of OSCs.

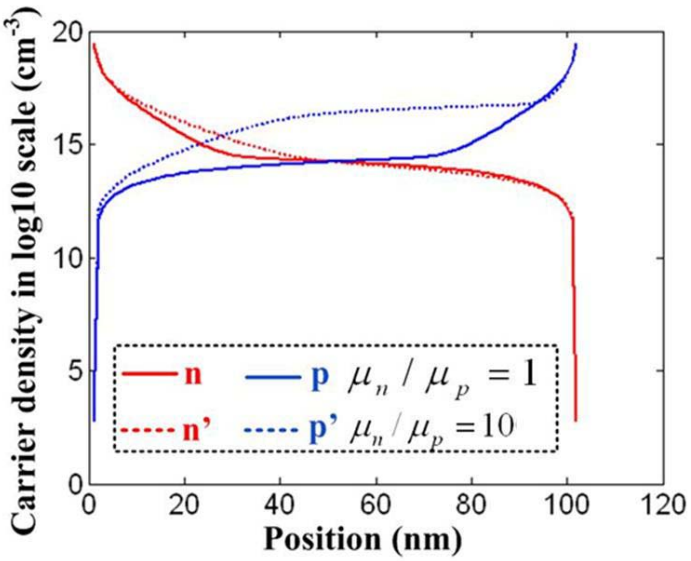


**Figure 4.14** Space charge due to unbalanced carrier transport in OSCs. The parameters are: thickness of the active layer 100nm, effective density of state $N_c = N_v = 2.8*10^{19}cm^{-3}$, electron mobility $\mu_n=1*10^{-3}cm^2/Vs$.

The simulation above indicates that balancing the carrier transport is a feasible way to optimize the performance of OSCs. In the followed chapter, single-walled carbon nanotubes (SWCNTs) were introduced in BHJ OSCs to improve the balance of carrier transport and hence increase the power conversion efficiency.

## 4.4 SUMMARY

Using the developed simulation tool in Chapter 2 and the determined monomolecular recombination loss in Chapter 3, we have investigated several methods to optimize the performance of OSCs. First, the thickness of active layer has been optimized due to the tradeoff between light absorption and photoexcited carrier extraction. Because OSCs are thin-film devices, optical transfer matrix is used to exactly determine the light absorption in the active layers. However, for P3HT/PCBM devices, with the optimized thickness and carrier mobility, PCE is still only 5%, which can not be commercialized. Then, the simulation results indicate that lowering the band gap of conjugated polymer is a promising alternative to further optimize the performance of OSCs because of the enhanced light absorption compared with P3HT. However, the nanomorphology of OSCs with low bandgap materials need to be further optimized to decrease the recombination loss. It is expected from the simulation that PCE can significantly boost up to 10%, if the recombination loss could be reduced as low as P3HT/PCBM devices. Moreover, unbalanced carrier transport is also investigated and the simulation indicates that increasing the hole mobility is a feasible way to optimize the performance of OSCs.

# 5.0 SINGLE-WALLED CARBON NANOTUBE ENHANCED OSCS

Considering the most important factor to limit PCE is the intrinsic slow carrier mobility (hopping and tunneling) in the disordered organic materials, single-walled carbon nanotubes (SWCNTs) are experimentally introduced in OSCs to increase the carrier mobility through the ballistic pathway provided by SWCNTs.

When SWCNTs are blended together with regioregular poly 3-hexylthiophene (P3HT) and 6,6-phenyl $C_{61}$-butyric acid methyl ester (PCBM) for the fabrication of OSCs, sufficient exciton dissociation is achieved at P3HT/PCBM interface, and meanwhile, free carriers transport through a ballistic pathway provided by SWCNTs with much lower resistance instead of hopping between the disordered organic materials. In this way, it is expected that the introduction of SWCNTs can optimize the performance of OSCs.

However, it has been observed that too much SWCNT decreased the performance of OSCs. Unfortunately, there is no convincing explanation based on theoretical analysis. In order to further optimize the performance of OSCs incorporated with SWCNTs, it is imperative to explore how SWCNTs exactly work in OSCs. In the following, different effects of semiconducting and metallic SWCNTs in BHJ OSCs have been experimentally investigated.

## 5.1 MATERIALS AND FABRICATION METHOD

The schematic structure of SWCNTs enhanced OSCs is shown in Figure 5.1. SWCNTs (1-2nm in diameter, 0.5-2um in length and 90% in purity, as indicated in Figure 5.2) as received from Sigma were dissolved in chloroform. After sonicated for 2 hours, SWCNTs were introduced to PCBM in chloroform and sonicated for another hour in order to blend SWCNTs and PCBM uniformly. Then P3HT in chloroform were added to the blended PCBM and SWCNTs solution. After stirring for 2 hour, the solution was left to settle down inside inert atmosphere for about 48 hours to allow remaining impurities and some bundled SWCNTs to sedimentate out. Therefore, the actual concentration of SWCNTs should be much lower than their nominal values. The active layer was spun on ITO glass (8Ω/square) coated with PEDOT:PSS with around 20nm thickness. Four kinds of devices (50:50 wt.-% P3HT/PCBM) with different weight ratio of SWCNTs to P3HT (nominal 0%, 1%, 3% & 5%) were fabricated and the thickness of active layers remains the same (100nm) for all devices. Finally, Aluminum (Al) was coated on top as cathode by thermal evaporation using a shadow mask at vacuum of $10^{-6}$ mbar and the area of the device was $10mm^2$, which was determined by the overlap between ITO and Al. It should be pointed out that the value of concentration is not accurate because after preparing the active layer solution, they are moved to a vacuum box for two days in order to deposit insoluble carbon nanotubes on the bottom. The real device is shown in Figure 5.3.

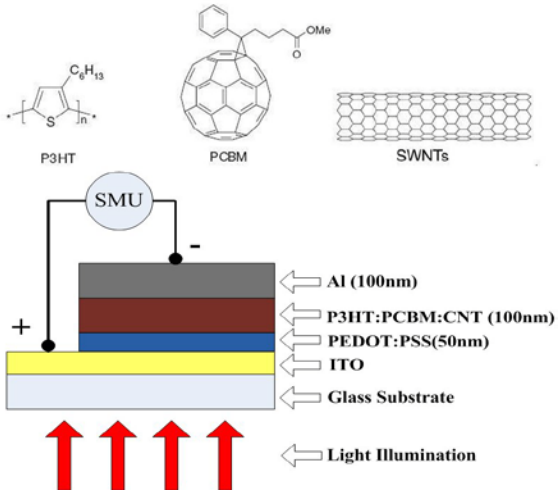


**Figure 5.1** Chemical structure of P3HT, PCBM and SWCNTs (top) and the schematic of a PV device (bottom).

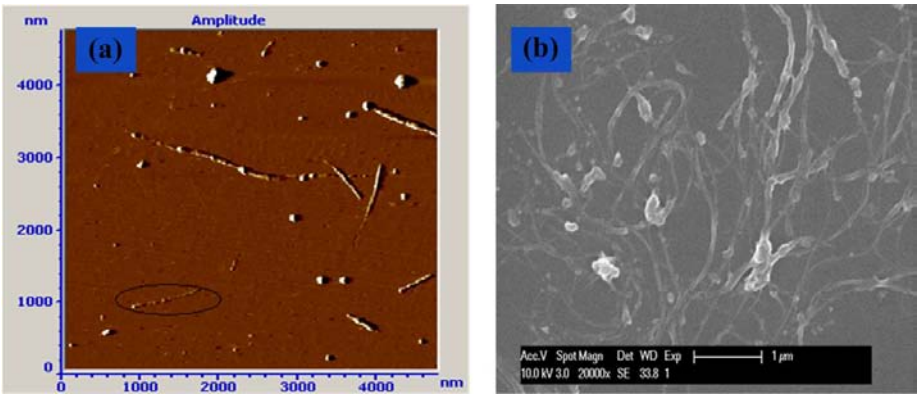


**Figure 5.2** SWCNTs investigated by (a) AFM image and (b) SEM image. Some SWCNTs have diameter about 1-2nm as shown in the black circle. Diameter of other SWCNTs is about 5nm, which is bundled SWCNTs.

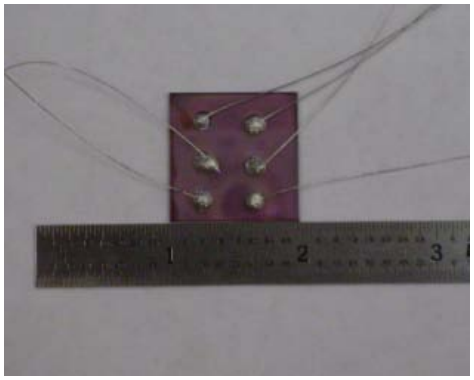

**Figure 5.3** Solar cell devices.

## 5.2 *J-V* OF SWCNTS ENHANCED OSCS UNDER ILLUMINATION

The current-voltage (*J-V*) characteristics of those four devices were measured under the same illumination intensity of $100 mW/cm^2$ and the results are shown in Figure 5.4. For the device with nominal 5% SWCNTs, it is short circuit as the actual concentration of SWCNTs exceeds the percolation threshold. Therefore, the performance of this device will not be further analyzed. It is observed that, in comparison with the device without SWCNTs, $J_{sc}$ for the device with nominal 1% SWCNTs increased around 30%. However, for the device with nominal 3% SWCNTs, $J_{sc}$, $V_{oc}$ as well as fill factor are all decreased. In order to optimize the performance of OSCs incorporated with SWCNTs, it is imperative to explore the underlying reason to cause the decreased performance.

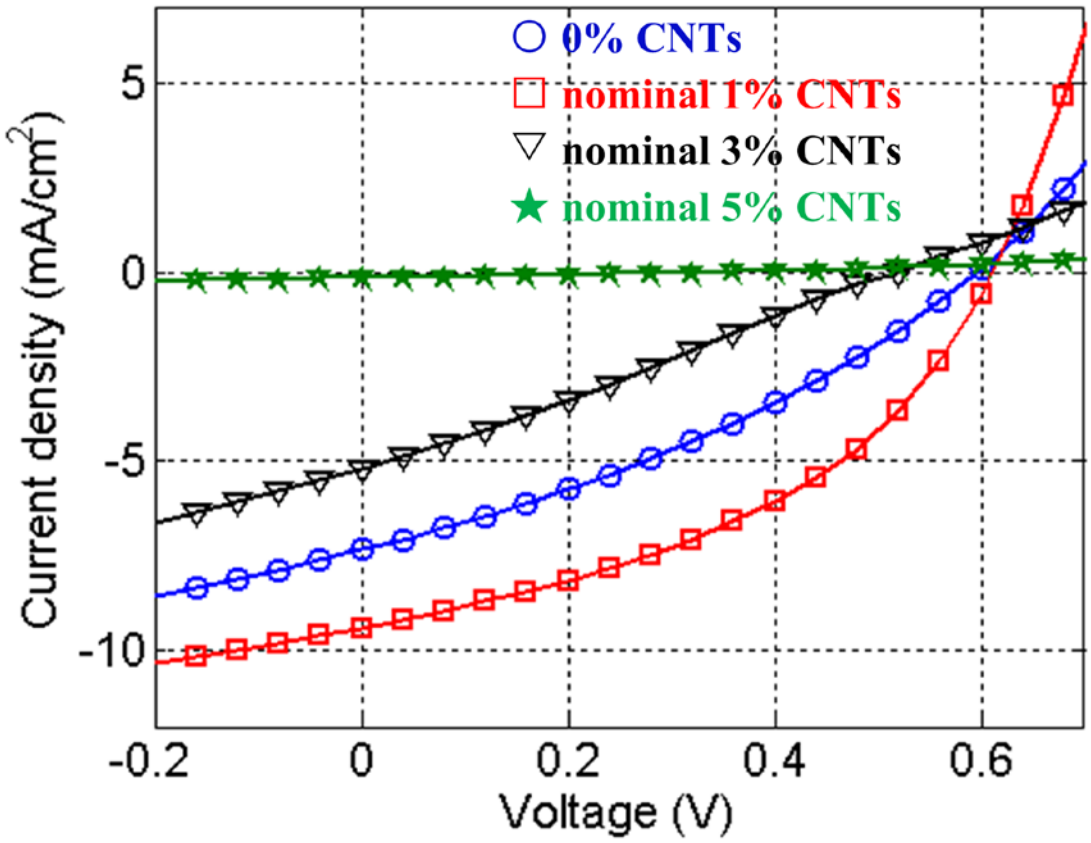


**Figure 5.4** *J-V* characteristics of OSCs with same thickness (100nm) and different concentration of SWCNTs under illumination intensity of 100mW/cm$^2$.

Both theoretical and rigorous simulation have proved that, for the situation with non-negligible recombination loss (fill factor is less than 50%) as in Fig.5.4, the fact that α in $J_{ph} \propto I^{\alpha}$ equals one indicates that monomolecular recombination is dominant; while α decreases monotonically from unit with the increase of bimolecular recombination. For the detail of intensity dependent photocurrent, please refer to Section 3.2. The dependence of photocurrent $J_{ph}$ on light intensity $I$ measured by subtracting dark current from the respective current-voltage curves at three different applied voltages (0V, 0.2V and 0.4V) is presented in Figure 5.5. For devices with 0% and nominal 1% SWCNTs, $\alpha$ close to unit at any bias voltage means that

the bimolecular recombination for these two devices is negligible. But for the device with nominal 3% SWCNTs, $\alpha$ =0.88 0.83 and 0.69 at 0V, 0.2V and 0.4V respectively indicates the strong bimolecular recombination in the device with higher concentration of SWCNTs.

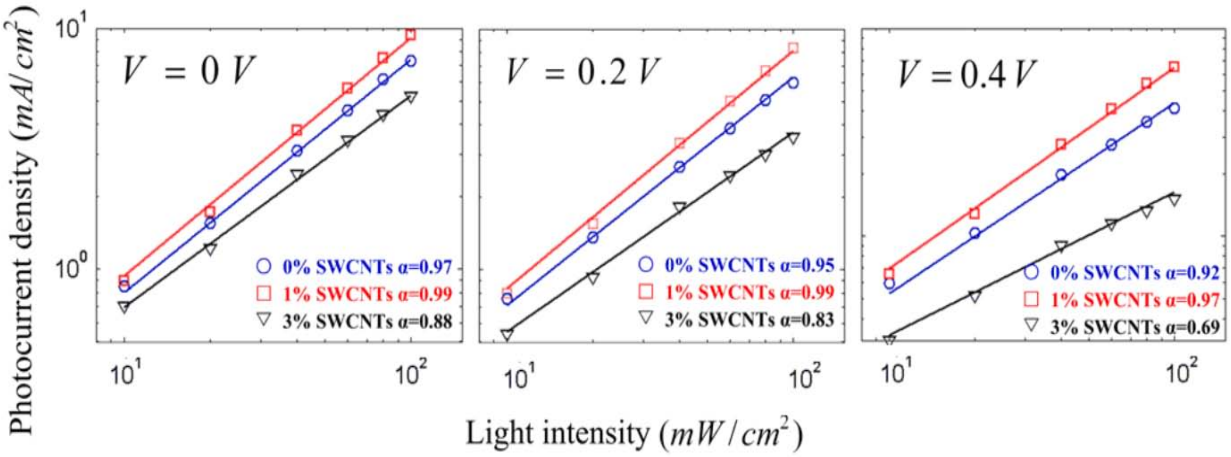


**Figure 5.5** Intensity dependence of the photocurrent for three devices at different applied voltages.

In general, SWCNTs are grown as mixed bundles of semiconducting and metallic tubes according to different chirality [71]. Even though only about 1/3 is metallic, the detrimental effect of metallic SWCNTs in the active layer of OSCs is not negligible. Due to the presence of metallic SWCNTs, some photoexcited free electrons in PCBM phase and holes in P3HT phase will recombine directly in metallic SWCNTs in the form of bimolecular recombination instead of being totally extracted by external circuit as shown in the schematic diagram (Figure 5.6). Therefore, it is reasonable to conclude that the degraded performance of the device with high concentration of SWCNTs (nominal 3%) is attributed to the abundance of metallic SWCNTs in the active layer.

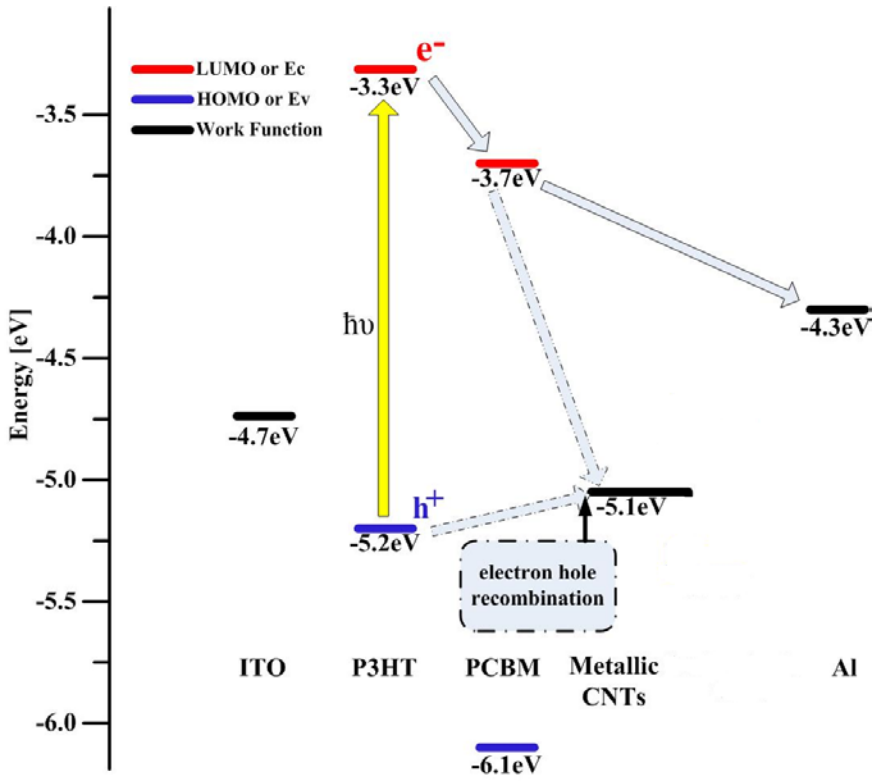


**Figure 5.6** Schematic energy diagram to show that the presence of metallic SWCNTs causes serious bimolecular recombination of photoexcited electrons from PCBM and holes from P3HT.

To verify that introduction of semiconducting SWCNTs can improve the electrical conductivity, the carrier mobility is investigated under illumination. Figure 5.7 presents the reverse bias dependence of photocurrent for devices with 0% and nominal 1% SWCNTs under illumination intensity of $100 mW/cm^2$ (only these two devices are analyzed because both have negligible bimolecular recombination, which makes them comparable). $J_{ph}$ is plotted as a function of the effective applied voltage across the devices $V_{FB}-V$ ,where $V_{FB}$ is flat band voltage, at which $J_{ph}=0$ (Figure 2.3). As shown in Figure 5.7, at small effective potential, implying a small electric field in the device, the photocurrent is extraction limited and linearly increased with the voltage as described by [72]:

$$J_{ph} = qG(u_e\tau_e + u_h\tau_h)\frac{V_0 - V}{L}, \quad \textbf{5.1}$$

where $q$ is the electron charge, $G$ is the generation rate of electron hole pairs, $u_e$ ( $u_h$ ) is electron (hole) mobility and $\tau_e$ ( $\tau_h$ ) is the lifetime of electron (hole). When the electric field increased to certain value at which carrier drift length $\omega = \mu\tau E$ exceeds the device thickness $L$, all the photoexcited free charge carriers are extracted at the contacts. The photocurrent is then photoexcitation limited and saturated as $J_{ph} = qGL$ [73, 74]. At turning point from linear to saturation region, carrier drift length $\omega$ is equal to the thickness of active layer $L$ [74], i.e. $L = \omega = \mu\tau E$. Therefore, mobility can be expressed as

$$\mu = \frac{L}{\tau E} = \frac{L^2}{\tau(V_0 - V)}. \quad \textbf{5.2}$$

It is reasonable to assume that the carrier life time $\tau$ is the same for devices with 0% and nominal 1% SWCNTs because the intensity dependence measurement demonstrates that the bimolecular recombination is negligible for both devices. The fabrication process guarantees that the thickness of the active layer $L$ is also the same. According to Eq 5.2, for fixed $\tau$ and $L$, carrier mobility $\mu$ is reversely proportional to $V_0 - V$ at the turning point. As shown in Figure 5.7, compared with high voltage of turning point ($V_B = 0.41V$) of the device without SWCNTs, lower voltage of turning point ($V_A = 0.19V$) of device with nominal 1% SWCNTs shows that average carrier mobility is doubled ($\frac{\mu_A}{\mu_B} = \frac{V_B}{V_A} = \frac{0.41}{0.19}$) after the introduction of SWCNTs into the active layer.

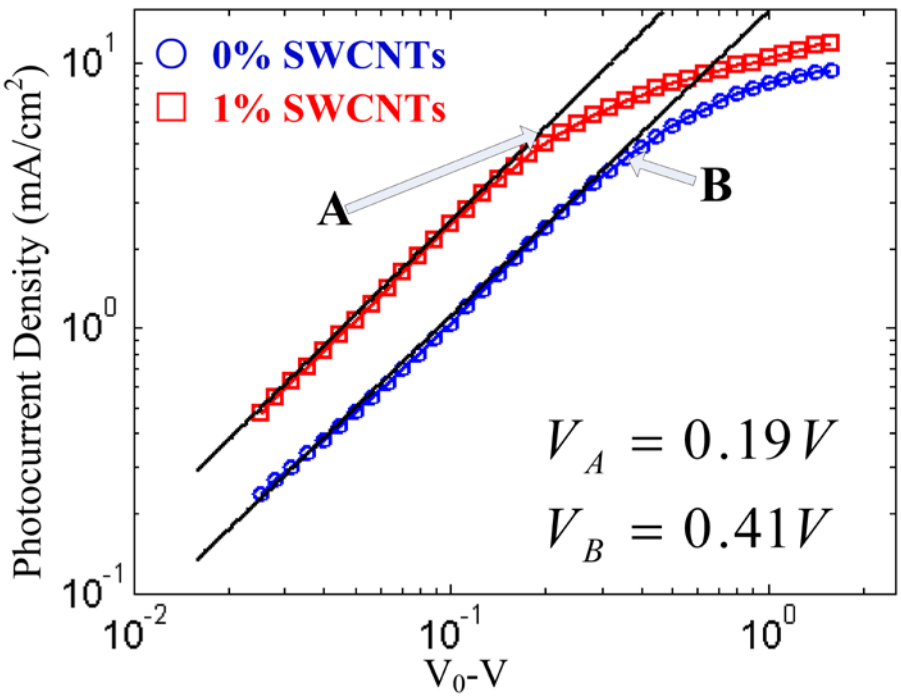


**Figure 5.7** $J_{ph}$ of devices with 0% and 1% SWCNTs as a function of effective applied voltage at illumination intensity of 100mW/cm$^2$.

## 5.3 *J-V* OF SWCNTS ENHANCED OSCS IN THE DARK

For illumination measurement above, carriers come from photoexcitation and then are extracted by the external circuit; while for dark measurement carriers are from the injection through external circuit and the device behaves a diode. For both situations, there are electrons and holes in the active layer which transport between two electrodes. Due to the presence of metallic SWCNTs in the active layer, the electron and hole will recombine in the metallic SWCNTs in the form of bimolecular recombination, whatever the electrons and holes come from either photoexcitation (under illumination) or from injection (in the dark).

Figure 5.8 shows *J-V* characteristics in the dark for three devices with nominal 0%, 1% and 3% SWCNTs. All devices show typical diode behavior without light illumination. For the device with nominal 3% SWCNTs, the forward current is decreased compared with other two devices because electron and hole, injecting from the external circuit, will recombine together in the metallic SWCNTs in the form of bimolecular recombination as discussed above. Then, dark *J-V* data were fitted to the standard diode current voltage relation, $J_F = J_s * \exp(\frac{qV}{nkT})$ to determine the ideality factor $n$ and saturation current density $J_s$. $q$ is unit electronic charge, $V$ is the forward bias voltage, $kT$ is thermal energy. According to [30, 75], carrier recombination results in the increase of ideality factor $n$. The fitting results at room temperature ($kT$=0.0256$eV$) are shown in Table 5.1.

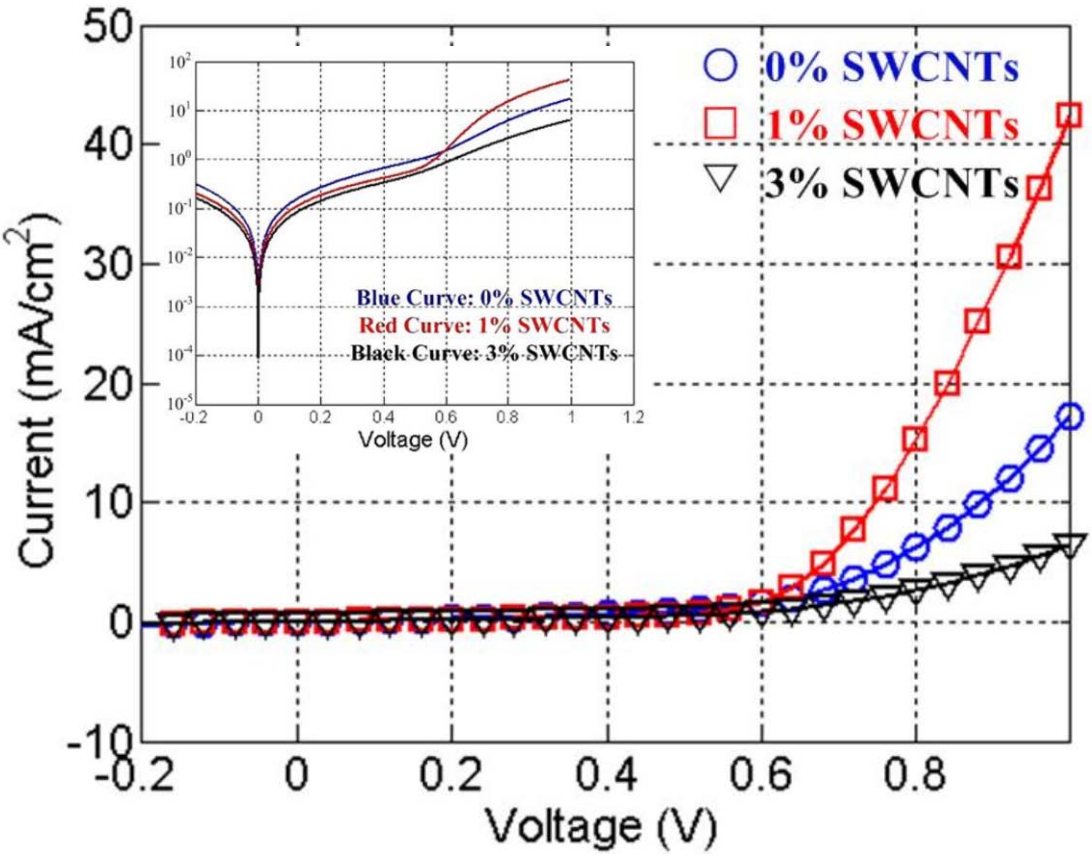


**Figure 5.8** Dark *J-V* characteristics of OSCs with different concentration of SWCNTs. The inset is the logarithm scale of *J-V* to show that all curves go through (V=0, J=0) point, which indicates that the capacitance effect is negligible in our solar cell devices.

**Table 5.1** Fitting parameters of dark *J-V* curves based on the ideal diode equation.

| | 0% SWCNTs | 1% SWCNTs | 3% SWCNTs |
|---|---|---|---|
| Ideality factor (*n*) | 3.2 | 3.09 | 6.51 |
| Saturation Current $J_s$ ($mA/cm^2$) | $3.707*10^{-4}$ | $10*10^{-4}$ | $247*10^{-4}$ |

The ideality factors of 0% SWCNTs device (*n*=3.2) and 1% SWCNTs device (*n*=3.09) are almost same, which indicates the recombination of carriers for these two devices are comparable. This is in coincidence with the conclusion from Figure 5.5 ($\alpha$ is almost same for

0% and 1% SWCNTs, indicating the bimolecular recombination is comparable in the illumination situation). However, for 3% SWCNTs, the ideality factor is much larger (twofold higher than that of devices with 0% and 1% SWCNTs). Therefore, the decreased forward current of 3% SWCNTs device is attributed to the increased ideality factor, which arises from the increased carrier recombination in metallic SWCNTs.

After investigation of ideal factor *n*, let us focus on the saturation current $J_s$. According to [30],

$$J_s = \frac{qD_p p_{n0}}{L_p} + \frac{qD_n n_{p0}}{L_n}, \quad \textbf{5.3}$$

in which, $L_p$ and $L_n$ are diffusion length, which can be expressed as

$$L_{p(n)} = \sqrt{D_{p(n)}\tau_{p(n)}}. \quad \textbf{5.4}$$

$D_{p(n)}$ is the diffusion coefficient and according to Einstein relation

$$D_{p(n)} = (kT/q)\mu_{p(n)}. \quad \textbf{5.5}$$

Based on Eq 5.3-5.5, saturation current density $J_s$ is related to carrier mobility and high mobility results in high saturation current density. According to Table 5.1, with increasing concentration of SWCNTs, $J_s$ increases as well because the introduction of SWCNTs improves the carrier mobility. However, the device with 3% SWCNTs (highest mobility) did not have the best performance because even though the carrier mobility increased, the carrier recombination also increased (high ideality factor) and the carrier recombination dominates the performance of the device with 3% SWCNTs.

The bimolecular recombination is negligible for both devices of 0% and nominal 1% SWCNTs, so dark *J*-*V* curves of these two devices are comparable. Because the presence of semiconducting SWCNTs provides a ballistic pathway which has lower resistance compared

with carrier hopping in the device without SWCNTs [76, 77], introduction of SWCNTs with low concentration (nominal 1%) into the device improved the electrical conductivity of the active layer as demonstrated by the enhanced forward current under the same applied voltage compared with the device without SWCNTs.

## 5.4 SUMMARY

The experiments show that the introduction of SWCNTs with small weight-ratio into BHJ OSCs can improve the performance as we expected; However, it has been observed that excessive SWCNTs decreased the performance of OSCs. The different effects of semiconducting SWCNTs and metallic SWCNTs have been investigated by *J-V* characterization both under illumination and in the dark. It is found that on one hand, the presence of semiconducting SWCNTs provides additional ballistic pathways for carriers to be extracted directly instead of slow hopping between disordered organic materials, which improve the performance of OSCs; on the other hand, metallic SWCNTs cause the electron and hole recombine, which decrease the efficiency of PV devices. This calls for a critical need to enrich the semiconducting ones in bulk SWCNTs either from fabrication or from post-fabrication process.

# 6.0 ELECTRICAL CHARACTERIZATION OF SWCNTS IN OSCS BY KELVIN PROBE FORCE MICROSCOPY

Introducing carbon nanotubes in BHJ OSCs has shown the ability to improve PCE because carbon nanotubes can provide ballistic pathways for carriers to transport with smaller electrical resistance instead of slow hopping and tunneling in disordered organic materials [76-78]. However, the fundamental question, whether carbon nanotubes work as donor (hole rich) or acceptor (electron rich) in BHJ OSCs, remains controversial in the literature [77]. Some assumed that nanotubes worked as acceptor materials and photoexcited electrons transported into nanotubes [78]; While others claimed that nanotubes were donor materials and became hole-rich after photoexcitation [79]; Until now, direct measurement is not available to support either side. Therefore, to further optimize the device performance, there is a critical need to fully understand the electrical role of SWCNTs in OSCs.

We assume that instead of acceptor materials, SWCNTs are donor materials to transport photoexcited holes in P3HT/PCBM OSCs. There are three macroscopic observations that can support our opinion.

- The first observation is based on the experiment results in [80]. When nanotubes are placed between active layer (P3HT/PCBM) and cathode (Al), the performance degrades according to illumination *J-V* measurement; while the efficiency increased when SWCNTs was coated between PEDOT:PSS and active layer. From this observation, it is

assumed that carbon nanotubes can not act as acceptor materials. (Aluminum as cathode, which is connected with SWCNTs, extracts electron)

- For P3HT/PCBM BHJ OSCs, the electron mobility in the PCBM phase is about 1 orders higher than the hole mobility in P3HT phase [18, 32]. If nanotubes were acceptor materials, the electron mobility would increase further and the difference between electron and hole mobility would also increase, which would result in unbalanced carrier transport and hence worse performance [18]. However, Figure 5.4 demonstrates that the fill factor (FF) and $J_{sc}$ of 0% SWCNT device is 32.7% and 7.6mA/cm$^2$ while for nominal 1% CNTs device, $FF = 42.4\%$ and $J_{sc} = 9.8 mA/cm^2$ ($V_{oc}$ is almost same). If carbon nanotubes worked as acceptor materials, the unbalanced charge transport can not result in the improvement of the performance as discussed in Section 4.3. It should be pointed out that the decreased performance of nominal 3% SWCNTs device is due to the carrier recombination.
- The unbalanced carrier transport is detrimental for carrier extraction in PVs, especially for OSCs due to the low carrier mobility. For OSCs, if one kind of carriers has much larger mobility compared with the other, the slower carriers can not be fully extracted as quickly as fast carriers, which will result in the space charge limited photocurrent [74]. For space charge limited photocurrent, $J_{ph} \propto (V_0 - V)^{1/2}$. However, there does not exist such region as that the slope of log($J_{ph}$) vs ($V_0$-$V$) is 0.5 in Figure 5.7, which means the introduction of nanotubes to the OSCs did not unbalance the charge transport. We believe: Even though individual SWCNTs are known to possess an extremely high carrier mobility (around 10000cm$^2$/Vs), when SWCNTs are blended with P3HT/PCBM, the mobility of SWCNTs decreased compared with individual ones because of the random

network of SWCNTs (however, it is still higher than carrier mobility in P3HT and PCBM phase).

The analysis above indicates that SWCNTs in OSCs is donor materials to transport holes. However, the argument so far is based on macroscopic evidences and might not be convincing. Therefore, in the following, Scanning Kelvin Probe Force Microscopy (KPFM) will be employed to locally investigate the electrical role of SWCNTs in P3HT/PCBM BHJ solar cells. For a comprehensive review of KPFM on organic thin film, refer to [81].

## 6.1 INTRODUCTION TO KELVIN PROBE FORCE MICROSCOPY

Atomic force microscope (AFM) [82] uses a piezo scanner to move a silicon (Si) or silicon nitride (SiN) cantilever with a sharp tip (radius is about 10nm) across the sample surface in a raster scan manner. AFM topographical images have lateral resolution down to nanometer scale and normal resolution down to atomic level, which can determine roughness, grain size, and features of the sample at nanometer scale. Comparing to scanning electron microscopy (SEM) and transmission electron microscopy (TEM), AFM can operate in ambient condition as well as in the liquid without destroying the sample, which offers the advantages of in-situ characterization and easy operation. Besides its capability of imaging high-resolution topography, AFM can also be used to study surface properties including electrical and magnetic characterizations at nanometer scale by its derivatives (also called advanced modes) such as current AFM (C-AFM) [83], electrostatic force microscopy (EFM) [84], scanning capacitance microcopy (SCM) [85], scanning spread resistance microscopy (SSRM) [86] and scanning

Kelvin probe force microscopy (KPFM) [87], *etc*. These advanced modes can perform simultaneous characterization of morphological and physical properties with high spatial resolution. Among all these advanced AFM modes, KPFM is probably the most complicated but most useful one, especially in the area of OSCs [88, 89]. It combines AFM and classical Kelvin probe technology and has ability to quantitatively map the surface potential difference between the sample and AFM tip at nanometer scales.

### 6.1.1 Classical Kelvin Probe Technique

The classical Kelvin Probe is a non-contact, non-destructive device to measure the contact potential difference ($V_{CPD}$) between the tip and the sample, based on the electrostatic force between them. $V_{CPD}$ between two different materials depends on work function, electric dipole at interface, adsorption layers and doping concentration in semiconductors [87]. The physics principle of classical Kelvin Probe technique is shown in Figure 6.1.

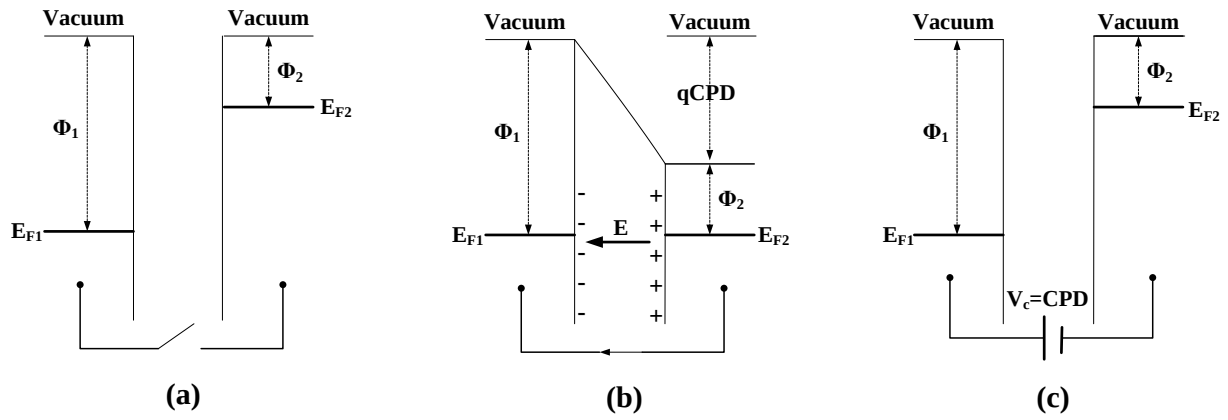


**Figure 6.1** Schematic diagram to show the physics principle of classical Kelvin Probe technique. (a) two materials with different work function ($\Phi_1$, $\Phi_2$) and Fermi level ($E_{F1}$, $E_{F2}$). (b) When these two materials are electrically contacted, electrons will move from material 2 with higher Fermi level ($E_{F2}$) to materials 1 with lower Fermi level ($E_{F1}$), until two Fermi levels are aligned. The charges present in these two materials cause electrostatic field (E) and the contact potential difference $V_{CPD}$ between these two materials. (c) if an external potential $V_c$ is applied between these two materials until the electrostatic force is nullified, the applied potential $V_c$ equals to the contact potential difference between these two materials as $V_c=V_{CPD}$.

In reality, a mechanical oscillation is introduced in the capacitor consisting of two materials (Kelvin Probe tip and the sample) with different work functions as shown in Figure 6.2. The capacitance ($C$) is reversely proportional to the distance between these two materials ($d$) as: $C \propto 1/d$ . Due to the introduced mechanical oscillation, the distance $d$ is:

$$d = d_0 + d_1 \cos(\omega_1 t), \qquad \textbf{6.1}$$

in which, $d_0$ is the initial distance between these two materials and $d_1 \cos(\omega_1 t)$ is the introduced mechanical oscillation. The current introduced by this oscillation can be expressed as:

$$i(t) = \frac{d}{dt}(CV) = \frac{dC}{dt}V, \qquad \textbf{6.2}$$

in which, the voltage on the capacitor ($V$) is:

$$V = V_{CPD} - V_c \,. \qquad \textbf{6.3}$$

If the applied voltage $V_c$ is tuned to nullify the current *i(t)* in the circuit of Figure 6.2, the contact potential difference can be obtained as: $V_{CPD}=V_c$.

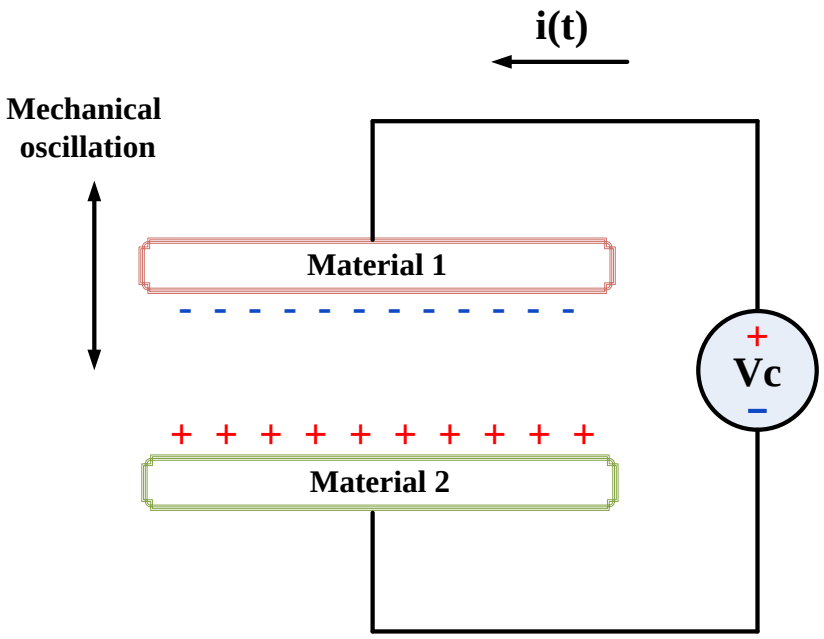


**Figure 6.2** Schematic to show how to obtain the contact potential difference $V_{CPD}$ in the classical Kelvin Probe.

### 6.1.2 Work Principle of Scanning Kelvin Probe Force Microscopy

KPFM is able to measure $V_{CPD}$ at nanometer scale. Instead of Van der Waals force, KPFM is based on the long range electrostatic interaction between a conductive AFM tip and the sample surface. When a voltage $V$ is applied between the sample and the tip (usually the sample is grounded and the voltage is placed on the AFM tip), the total energy ($U$) stored in the capacitor formed by the tip, substrate and the air gap is [90]:

$$U = -\frac{1}{2}CV^2. \quad \textbf{6.4}$$

By assuming $V$ is irrelevant to $z$, the electrostatic force can be expressed as

$$F = \frac{1}{2}\frac{\partial C}{\partial z}V^2. \quad \textbf{6.5}$$

$$V = V_{cp} + V_{dc} + V_{ac}, \quad \textbf{6.6}$$

where $V_{cp}$ is the contact potential difference between the tip and the sample, $V_{dc}$ and $V_{ac}$ are applied AC and DC voltage to the AFM tip respectively. The voltage ($V$) between the AFM tip and the sample can be modified as:

$$V = (V_{cp} + V_{dc}) + V_{ac}\sin(\omega_e \times t), \quad \textbf{6.7}$$

in which $\omega_e$ is the frequency of AC voltage on the tip. Combining Eq. 6.2 and 6.4, electrostatic force can be expressed as

$$\begin{aligned} F &= \frac{1}{2}\frac{\partial C}{\partial z}[(V_{cp} + V_{dc}) + V_{ac}\sin(\omega_e \times t)]^2 \\ &= \frac{1}{2}\frac{\partial C}{\partial z}[(V_{cp} + V_{dc})^2 + 2(V_{cp} + V_{dc}) * V_{ac}\sin(\omega_e \times t) + (V_{ac}\sin(\omega_e \times t))^2] \\ &= \frac{1}{2}\frac{\partial C}{\partial z}\left\{[(V_{cp} + V_{dc})^2 + \frac{1}{2}V_{ac}^2] + 2(V_{cp} + V_{dc}) * V_{ac}\sin(\omega_e \times t) + [-\frac{1}{2}V_{ac}^2\cos(2(\omega_e \times t))]\right\} \end{aligned} \quad \textbf{6.8}$$

Focus on the second term of the electrostatic force,

$$F_{\omega_e} = \frac{\partial C}{\partial z}(V_{cp} + V_{dc}) * V_{ac}\sin(\omega_e \times t), \quad \textbf{6.9}$$

which is the electrostatic force with the electric driving frequency ($\omega_e$). If a close loop is applied to adjust $V_{dc}$ such as the signal of first order frequency ($\omega_e$) is nullified, $V_{cp}$=-$V_{dc}$. Moreover, for the common used AFM coated with metal, the work function of the metal is well known. From the value of $V_{cp}$, the work function of substrate can be obtained at nanometer scale [91].

There are basically two methods to implement KPFM. The first is called dual-path lift-up scan mode, in which the electrostatic force is nullified by coupling a DC voltage $V_{dc}= -V_{cp}$ signal to the probe when the probe is being lifted to a small height (10nm-20nm) above the sample surface and then following the exact profile of the surface acquired by the previous scan. In this case, electrical driving frequency ($\omega_e$) can be set at the mechanical resonant frequency ($\omega_m$) to achieve high sensitivity; Second method is single scan, in which the photo detector records the combination of the tip oscillation both at $\omega_m$ and $\omega_e$ as shown in Figure 6.3. In such case, $\omega_e$ must be set to a different value than $\omega_m$. “Lock in 1” amplifier as shown in Figure 6.3 isolates the oscillation signal at $\omega_m$ and compares the oscillation amplitude with the set point value. The feedback loop of “Z servo” follows the topography of the sample to maintain the oscillation amplitude at the set point, and therefore, acquires the surface topography. At the same time, “Lock in 2” amplifier extracts the oscillation signal at $\omega_e$. The feedback loop of “KFM servo” applies a DC voltage ($V_{dc}$) to the AFM tip to nullify the electrostatic force at $\omega_e$. According to Eq. 6.9, if the signal at $\omega_e$ is nullified ($V_{cp}$=-$V_{dc}$), the surface potential can be precisely acquired. In summary, by using two different driving signals and two separated feedback loops, topography and surface potential can be simultaneously mapped at nanometer scales using single-scan mode SKPM.

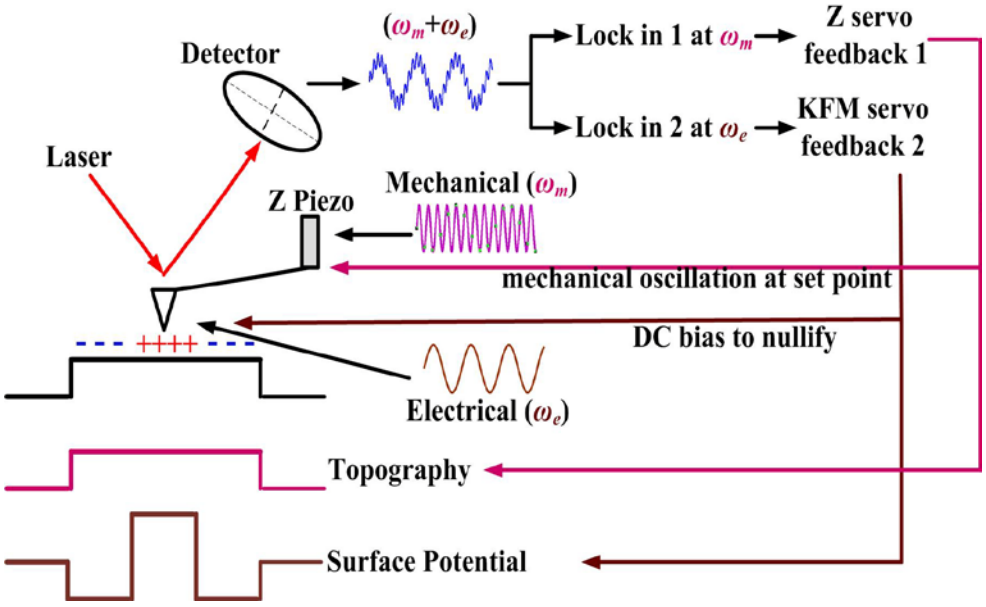


**Figure 6.3** Mechanism of KPFM in single scan mode based on Agilent 5500 AFM with Mac III controller.

Figure 6.4 demonstrates the capability of "KPFM servo" to nullify the electrical oscillation $F(\omega_e)$. *X* axis is the tuning frequency in unit of kHz and *y* axis represents $F(\omega_e)$ signal in unit of volt. In Figure 6.4a where "KPFM servo" is off, oscillation amplitude at $\omega_e$=10.234kHz is 0.186V. This is called electrostatic force microscopy (EFM) without nullifying $F(\omega_e)$. When "KPFM servo" is turned on in Figure 6.4b, it is clear that $F(\omega_e)$ is almost fully nullified. The oscillation amplitude at $\omega_e$ (3mV) is comparable with the electrical oscillation noise of the system, which is about 1.6mV.

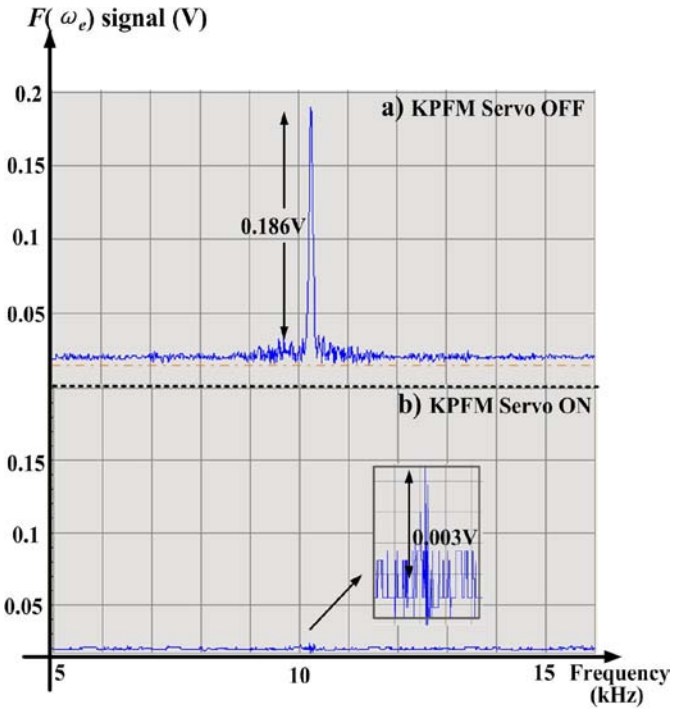


**Figure 6.4** F($\omega_e$) signal when KPFM servo off (a) and on (b).

Dual scan and single scan KPFM are compared in Table 6.1. Considering the small feature of SWCNTs with diameter only about 1nm, single-scan mode KPFM is chosen due to the higher spatial resolution compared with dual scan mode.

**Table 6.1** Comparison between single-scan and dual-scan KPFM.

| | Single Scan | Dual Scan |
|---|---|---|
| Speed | Fast | Slow |
| Spatial resolution | High | Low |
| $\omega_e$ | $\omega_e \neq \omega_m$ | $\omega_e = \omega_m$ |
| Sensitivity | Low | High |
| Crosstalk | Need to be minimized | Low |

## 6.2 INVESTIGATION AND MINIMIZATION OF CROSSTALK IN KPFM

For the single-scan KPFM, topography and surface potential are acquired simultaneously. Therefore, there is inevitably crosstalk, which might cause the significant deviation of surface potential and topography from their actual value. We have done a comprehensive study to minimize the crosstalk between the topography and surface potential image. The experimental investigation shows that the crosstalk is almost negligible if the electrical frequency in the second lock-in ($\omega_e$) is carefully tuned such that it is neither a multiple nor a factor of the mechanical frequency in the first lock-in ($\omega_m$).

In our KPFM studies, the mechanical drive frequency ($\omega_m$) was determined by the first flexural resonant frequency of the cantilever. The AFM tip (Veeco SCM-PIT, k=2.8N/m, coated with Pt/Ir) has a nominal $\omega_m$ about 75kHz. The electrical drive frequency ($\omega_e$) was set around 10kHz. However, the exact value of $\omega_e$ needs to be carefully tuned in order to eliminate the crosstalk between the oscillation signals at $\omega_m$ and at $\omega_e$. Intuitively, the cross-talk should be significantly reduced if the electrical frequency in the second lock-in ($\omega_e$) is neither set at a multiple nor at a factor of the mechanical frequency in the first lock-in ($\omega_m$). For example, if $\omega_m$=80kHz, we choose $\omega_e$ =10.234kHz instead of 10kHz to avoid crosstalk.

To verify our hypothesis, we set up the following experiment to study cross-talk between topography and surface potential images: A square-wave test voltage from an external function generator (peak to peak voltage of 0.6V and frequency of 4Hz) was applied to a cleaned ITO glass substrate and KPFM was employed to the ITO glass surface while setting scan size to zero. With this set-up, we can simulate an absolute flat surface with periodic potential when the scanning rate is a factor of the frequency of the square wave. Ideally, the surface potential signal should change periodically because of the applied square wave voltage, while there should be no

topography feature as the scan size was set to zero. In reality, the feature in the topography image represents the crosstalk from surface potential image to the topography image. In our experiment, the mechanical drive frequency ($\omega_m$) is set at 80kHz. Figure 6.5a and 6.5b are topography and surface potential image acquired when $\omega_e$ was set to 10kHz, which is a factor of $\omega_m$. Figure 6.5a' and 6.5b' are the topography and surface potential image when $\omega_e$=10.234kHz, which is not a factor of $\omega_m$. All other parameters, such as scan rate (0.5Hz), proportional gain (P gain), integral gain (I gain) for two feedback loops and the amplitude of AC bias to the tip, are kept the same for both situations. In Figure 6.5a, it is observed that there exists non-ignorable crosstalk from SP signal to the topography because $\omega_e$ was a factor of $\omega_m$. The crosstalk in Figure 6.5a is about 1.3nm, which is comparable to the diameter of SWCNTs. When we set $\omega_e$=10.234kHz to avoid being a factor of $\omega_m$, the crosstalk from SP signal to the topography was significantly reduced from 1.3nm (Figure 6.5a) to 0.15nm (Figure 6.5a'), which is about one order smaller than the diameter of SWCNTs. Therefore, if $\omega_e$ is not a factor of $\omega_m$, the crosstalk from SP signal to the topography is negligible compared to the feature size studied herein (SWCNTs). It is necessary to mention that the scan rate is set to 0.5Hz and frequency of square wave is 4Hz, which is a multiplier of scan rate. Ideally, surface potential pattern should be like a vertical strip. However, in SP images, strips are tilted due to the different timing synchronies between the frequency of external square wave voltage source (from the function generator) and internal scan rate (from AFM).

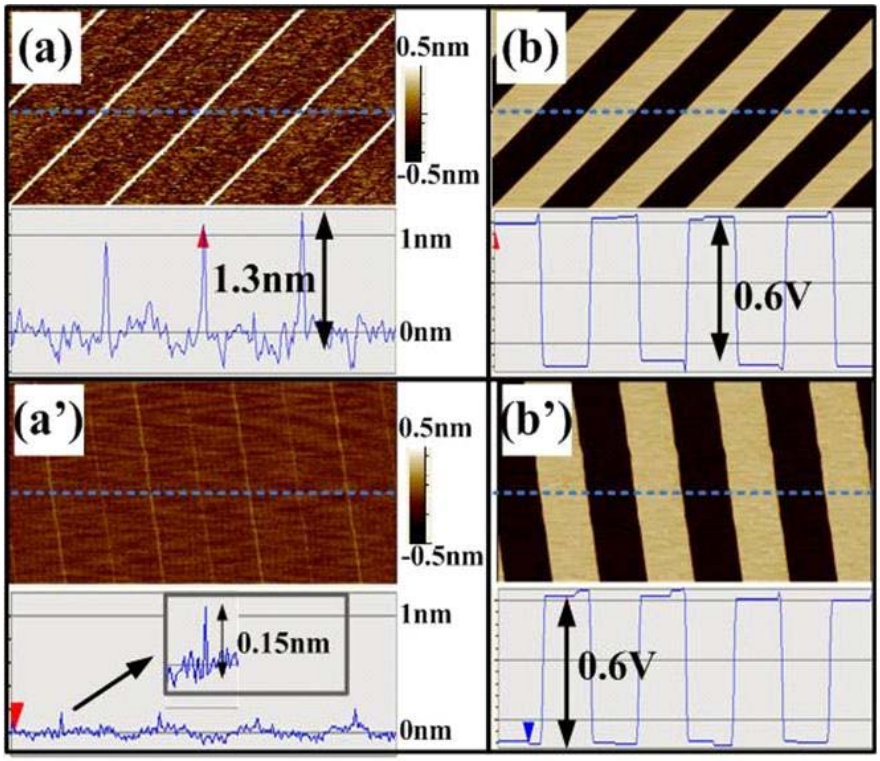


**Figure 6.5** Investigation of crosstalk from surface potential to topography. Comparison of the crosstalk between the situations in which $\omega_e$ is a factor of $\omega_m$ (a, b) and $\omega_e$ is not a factor of $\omega_m$ (a', b'). a & a' represent the crosstalk from surface potential to topography.

Every time before KPFM study of SWCNTs, the above testing experiment (square wave voltage applied to ITO surface with zero scan size) was always performed for two reasons: first, to fine tune the KPFM control feedback parameters (P gain and I gain for the second feedback loop); second, to make sure the parameters we chose such as $\omega_e$, $\omega_m$, scan rate, I gain, P gain for both two feedback loops will not induce large crosstalk between topography and surface potential image.

The above experiment verifies that the crosstalk from SP signal to the topography is negligible in our KPFM study of SWCNTs if electric driving frequency ($\omega_e$) was carefully chosen. It is also necessary to investigate the crosstalk from topography signal to SP signal. The

following experiment was set up to explore the crosstalk from topography to SP signal: a grating (depth 200nm) was scanned in tapping mode by using the KPFM tip, where no electric oscillation ($\omega_e$) was applied to AFM tip. “Lock in 1” extracts the topography signal as usual tapping mode AFM; while at the same time, “Lock in 2” acquired the signal at 10.234kHz, which is electrical driving frequency in KPFM mode. The difference between this experiment and KPFM is that there are neither electrical oscillation (AC signal) nor electric bias (DC signal) applied to the conductive AFM tip in this experiment even though the signal at electric drive (10.234kHz) is also acquired. Therefore, the crosstalk from topography to SP signal can be ideally simulated. The signal in “lock in 2” arises from the nonlinear interaction between the AFM tip and the sample. The experiment result is shown in Figure 6.6. It is clear that the cross talk from topography to SP is only about 0.007 V, which is negligible.

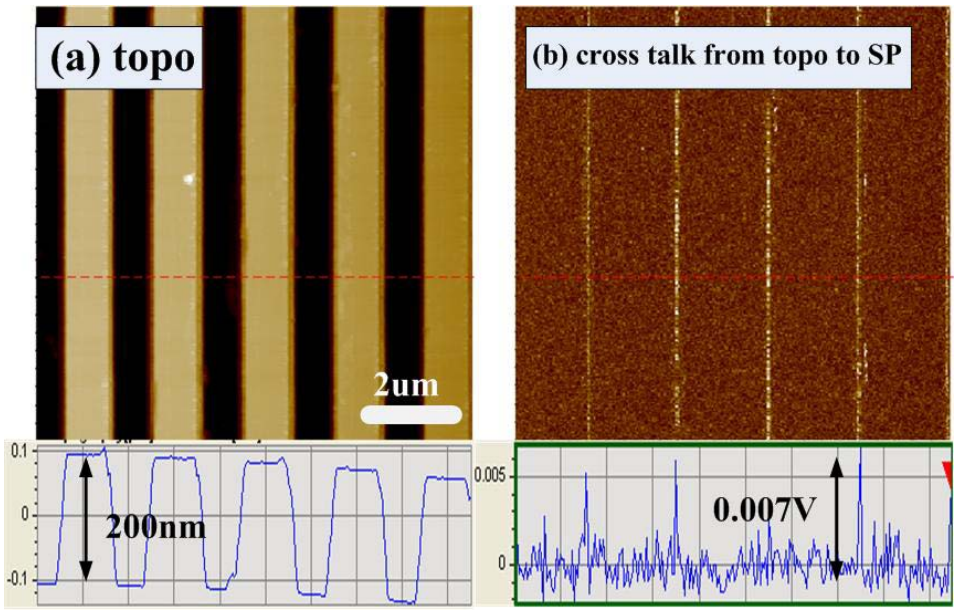


**Figure 6.6** Investigation of crosstalk from topography to SP image. (a) the topography of a grating with 200nm depth. (b) the signal extracted at $\omega_e$ without electric drive at $\omega_e$, which indicates the crosstalk from topography (a) to surface potential (b).

At this stage, it is safe to conclude that the crosstalk between topography and surface potential image (crosstalk from surface potential to topography as well as from topography to surface potential) is negligible in our experiments.

## 6.3 KPFM OF SWCNTS ON OSCS

KPFM has been utilized to analyze MDMO-PPV/PCBM OSCs because it is feasible to detect the relative large PCBM clusters (in size larger than 100nm) from the blending [92, 93]. However, KPFM has rarely been used to study P3HT/PCBM OSCs due to the difficulty to differentiate PCBM from P3HT because of the uniform distribution of these two materials in sub nanometer scale. Wu, *et al.* [79] used KPFM to study the film blending with P3HT and multi-wall carbon nanotubes. However, it was hard to distinguish nanotubes from P3HT because nanotubes were imbedded in the polymer and might not be exposed at the sample surface to the AFM tip. In order to tackle this problem, SWCNTs were carefully coated on top of active layer in our experiment as shown in the schematic diagram (Figure 6.7). Thus, it is feasible to differentiate SWCNTs from other materials and characterize their electrical properties by KPFM.

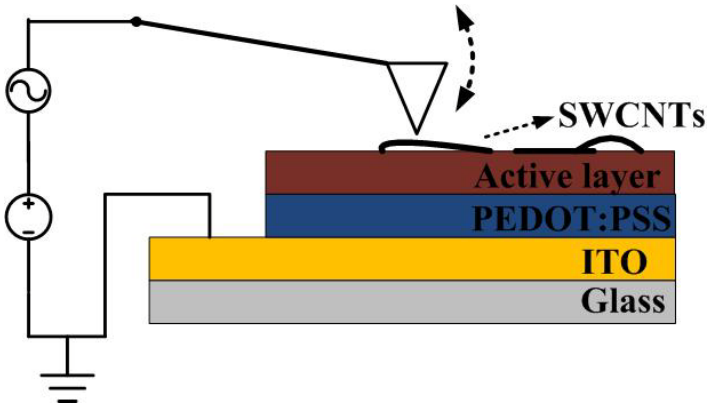


**Figure 6.7** Schematic of KPFM of SWCNTs on top of active layer.

In our study, KPFM was first applied to investigate SWCNTs on top of P3HT film as shown in Figure 6.8. The fabrication procedure followed our previous study as in [52] except that instead of Aluminum, SWCNTs were carefully coated on top of P3HT in order to expose both P3HT and SWCNTs to the AFM tip. The topography in the dark (Figure 6.8a) and under illumination (not shown here) are almost the same except for some thermal drift. The sample was illuminated by a halogen lamp with intensity of 90mW/cm$^2$ calibrated by a thermal power meter. The surface potential (SP) images are shown in Figure 6.8b (in the dark) and Figure 6.8c (under illumination). Figure 6.8d indicates SP values of cross sections both in the dark and under illumination. Figure 6.8e is the band schematic diagram to show the heterojunction between P3HT and SWCNTs. SP images show that the width of SWCNTs is about 90nm, which is much larger than the actual diameter of SWCNTs. There are two factors which might account for the enlarged diameter of SWCNTs. First, due to the coating of conductive layer on the AFM tip, the radius of KPFM tip is around 25nm, which is larger than that of bare silicon tip ($\leqslant$10nm). Second, long-range electrostatic force also limits the spatial resolution of KPFM image [90, 94]. Comparing Figure 6.8b and 6.8c, SP contrast between SWCNTs and P3HT slightly decreased from 0.14V in the dark to 0.08V under illumination. The decreased SP contrast under

illumination indicates the transport of photoexcited carriers from active layer (P3HT) to SWCNTs, which can be explained with the help of the schematic band diagram (type I heterojunction) in Figure 6.8e. In the dark, SP of P3HT is higher than that of SWCNTs, which implied the direction of local electric field (E) is from P3HT to SWCNTs (refer to the relative vacuum level). As indicated by the arrow in Figure 6.8e, holes can move to SWCNTs after light absorption by P3HT, which is energy favored; While electrons tend to remain in P3HT because the energy barrier $\triangle$E in the conduction band. The reduced SP contrast under illumination is attributed to the induced electric field by both photoexcited electrons in P3HT and holes in SWCNTs, which has opposite direction as the local electric field in the dark. KPFM study of SWCNTs on top of P3HT clearly verifies that SWCNTs work as donor in P3HT/SWCNTs OSCs.

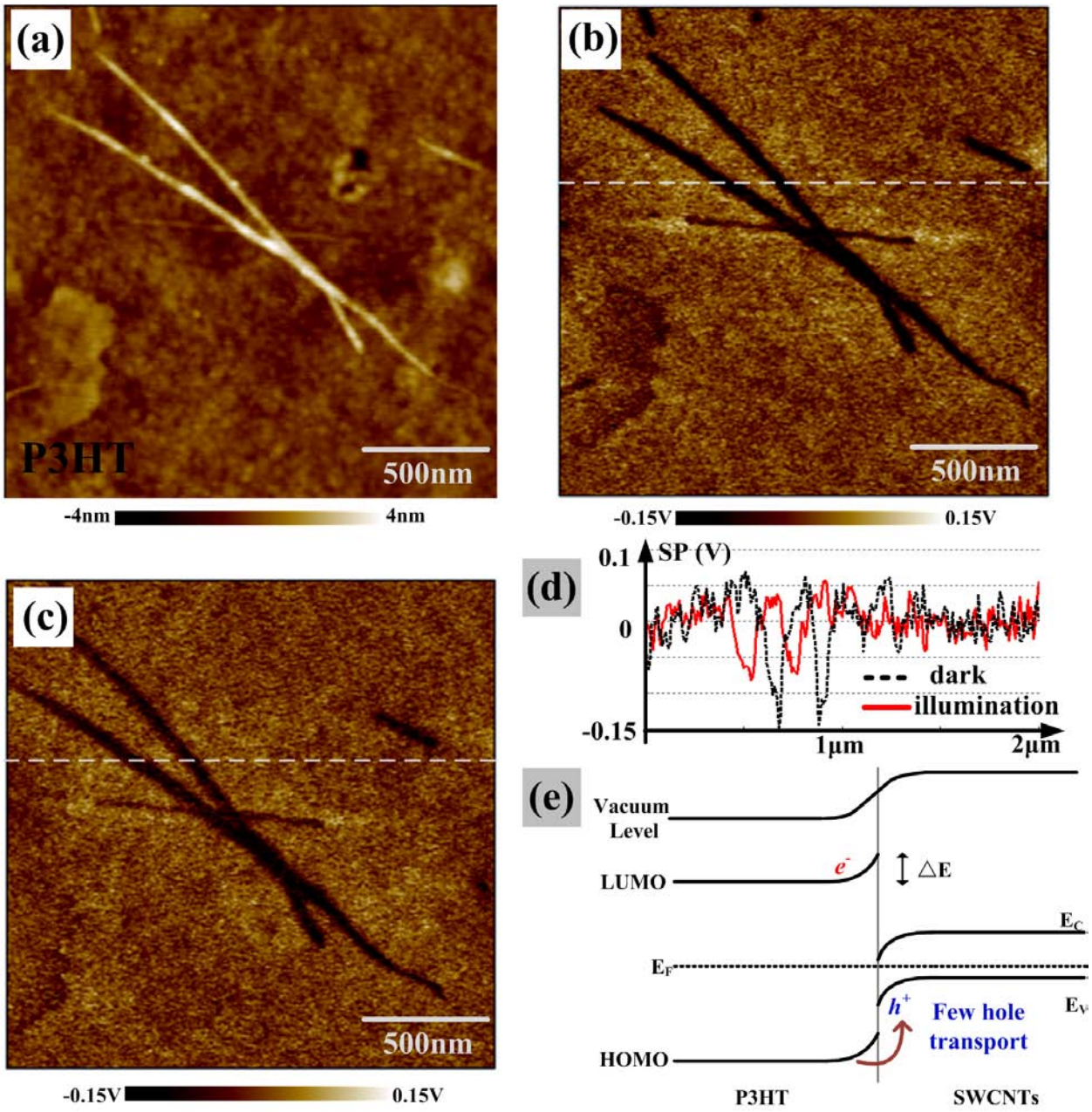


**Figure 6.8** (a) Topography of SWCNTs on top of P3HT in the dark. (b) SP image in the dark. (c) SP image under illumination. (d) SP values of the cross section indicated by the dash line in SP images. The position of SWCNTs shifts under illumination compared with in the dark because of thermal drift. (e) Band schematic diagram of type I heterojunction between P3HT and SWCNTs.

In order to explore electrical role of SWCNTs in P3HT/PCBM/SWCNTs OSCs, KPFM was again used to study SWCNTs on top of P3HT/PCBM blended film. Figure 6.9a is topography of SWCNTs on top of P3HT/PCBM blended film in the dark. The SP images in the dark (Figure 6.9b) and under illumination (Figure 6.9c) as well as their SP values of the cross section (Figure 6.9d) indicate that SP contrast between SWCNTs and P3HT/PCBM under illumination almost disappeared. Specifically, SP contrast decreases from 0.19V in the dark to 0.04V under illumination. Compared with SWCNTs on P3HT in Figure 6.8, decrease of SP contrast between SWCNTs and P3HT/PCBM under illumination is more significant because more holes transport from active layer (P3HT/PCBM) to SWCNTs and as a result, the induced electric field by photoexcited electrons and holes is much stronger to make the band flatten [95]. The heterojunction band schematic diagram in Figure 6.9e indicates photoexcited charge transport. When SWCNTs were coated on top of P3HT/PCBM blending, photoexcited excitons are effectively separated to free carriers at the interface between blended P3HT and PCBM due to BHJ configuration [25]. While for SWCNTs on top of P3HT, only small amount of excitons located at interface between P3HT and SWCNTs can be separated to free carriers considering the exciton diffusion length is only about 10nm. For SWCNTs on top of P3HT film, insufficient holes transport can not change SP contrast between P3HT and SWCNTs (Figure 6.8d) as much as for SWCNTs on top of P3HT/PCBM film (Figure 6.9d), which can explain that the low efficiency of conjugate polymer/SWCNTs solar cells is attributed to insufficient exciton dissociation [77]. The comparison between Figure 6.8 and 6.9 also demonstrates that BHJ is very important for photoexcited exciton to be separated to free electrons and holes, as we discussed before.

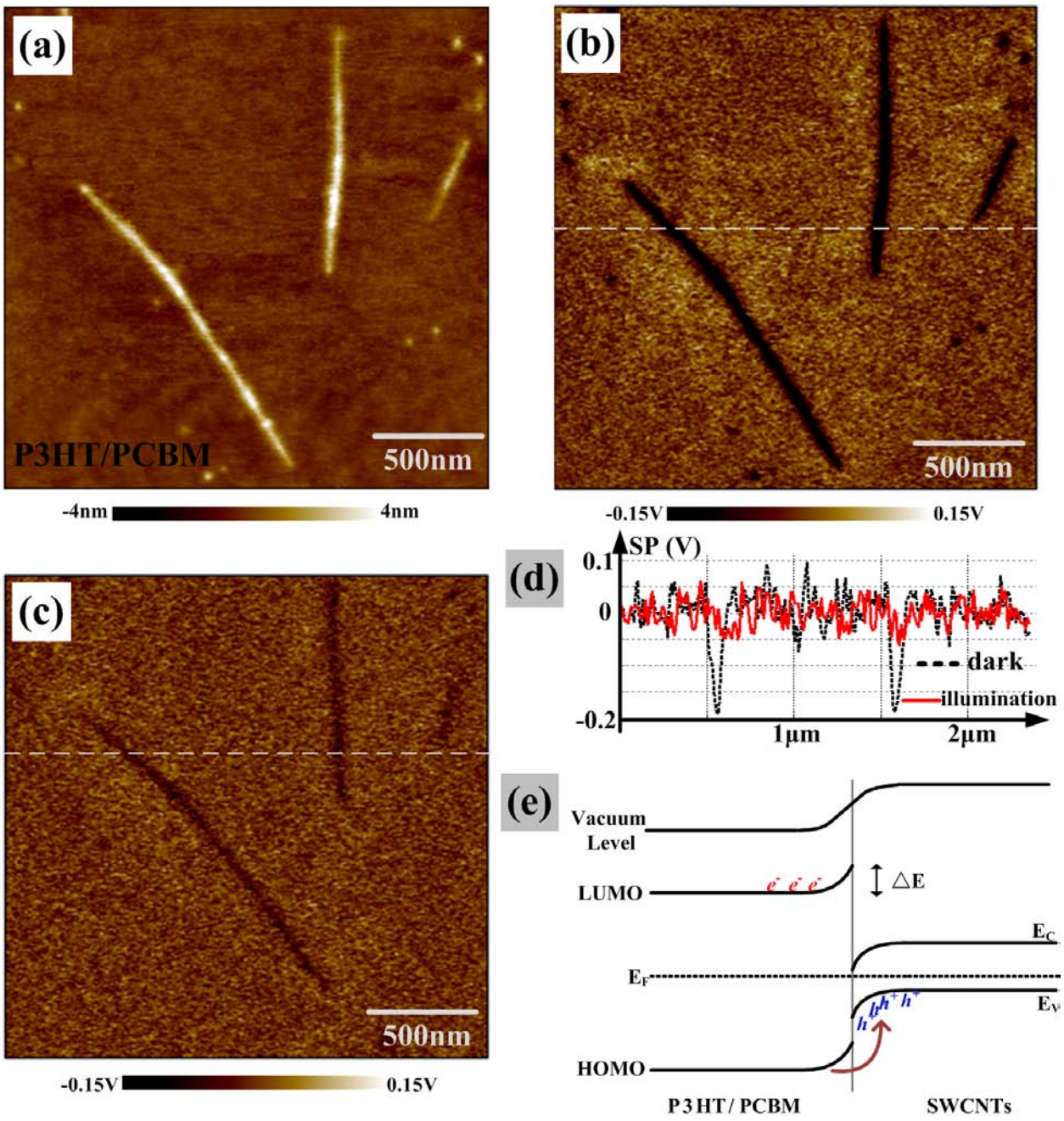


**Figure 6.9** (a) Topography of SWCNTs on top of P3HT/PCBM in the dark. (b) SP image in the dark. (c) SP image under illumination. (d) SP values of the cross section. (e) Band schematic diagram of type I heterojunction between P3HT/PCBM and SWCNTs.

KPFM study on P3HT/PCBM/SWCNTs also demonstrates that photoexcited holes are present in SWCNTs and thus SWCNTs work as donor, which is coincident with the macroscopic fact that introducing SWCNTs in P3HT/PCBM BHJ solar cells is able to increase PCE due to the increased hole mobility. For blended P3HT/PCBM solar cells, the electron mobility in PCBM is about one order higher than the mobility of holes in P3HT [18]. If nanotubes were acceptor to transport electrons, the electron mobility would increase and hence the mobility difference between electron and hole would further increase, which could result in much more unbalanced carrier transport [18]. Therefore, the improved performance of P3HT/PCBM/SWCNTs solar cells at least proves that the introduction of SWCNTs increases hole mobility, which means SWCNTs work as donors more than as acceptors.

To further verify that the improved performance of P3HT/PCBM/SWCNTs OSCs is attributed to the increased hole mobility because of the introduction of SWCNTs, KPFM of SWCNTs on PEDOT:PSS was performed. Figure 6.10a is the topography of SWCNTs on top of PEDOT:PSS in the dark. SP images in the dark (Figure 6.10b) and under illumination (Figure 6.10c) are almost the same, indicated by the cross-section value in Figure 6.10d because of absence of light absorption. There is a dust near SWCNTs in topography image while it is not detectable in SP image, which also demonstrates that the topography and SP signal are well separated and there is no interference between them, as we discussed in Section 6.2. Different from SWCNTs on top of P3HT/PCBM film where SP value of SWCNTs is smaller compared with the substrate, SP of SWCNTs is larger than that of PEDOT:PSS, which indicates the direction of local electric field at the interface is from SWCNTs to PEDOT:PSS (refer to the relative vacuum level in Figure 6.10e). The band schematic diagram in Figure 6.10e shows that transports of photoexcited holes from SWCNTs to PEDOT:PSS are energetically favored.

Therefore, photoexcited holes can transport effectively from active layer (P3HT/PCBM) to SWCNTs, to PEDOT:PSS and then be extracted by anode. SWCNTs work as a bridge to extract photoexcited holes.

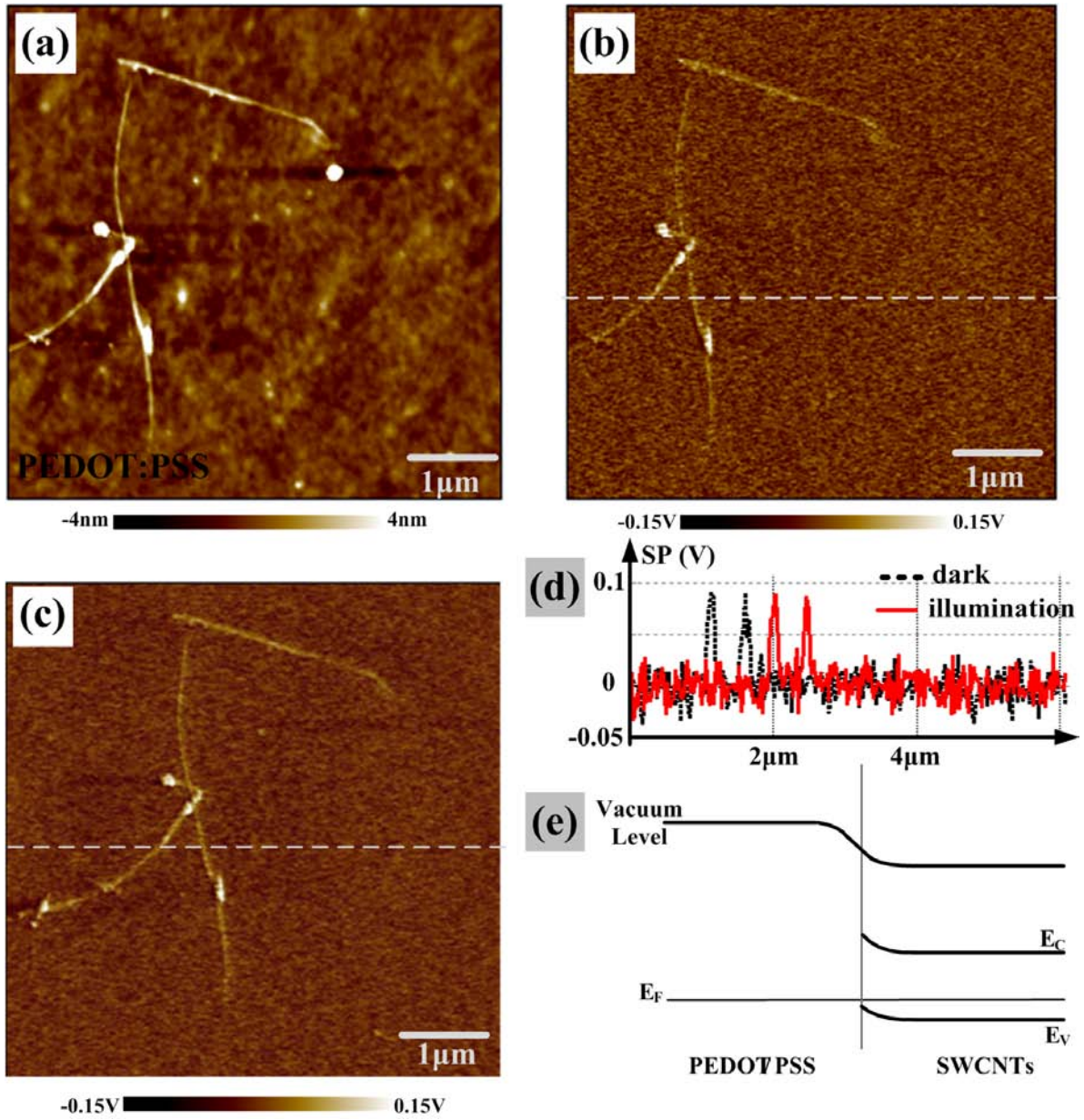


**Figure 6.10** (a) Topography of SWCNTs on top of PEDOT:PSS in the dark. (b) SP image in the dark. (c) SP image under illumination. (d) SP values of the cross section. (e) Schematic diagram to show contact between PEDOT:PSS and SWCNTs.

## 6.4 KPFM OF ZINC OXIDE NANOWIRE ON OSCS

The electric role (donor materials) of SWCNTs in P3HT/PCBM OSCs has been investigated by both macroscopic observations as well as KPFM. The electric role of Zinc Oxide (ZnO) nanowires in P3HT/PCBM OSCs was also investigated. Because the valence band of ZnO nanowires is much lower compared with HOMO of P3HT as indicated in Figure 6.11, it is well known that ZnO is acceptor materials and should be electron rich after photoexcitation.

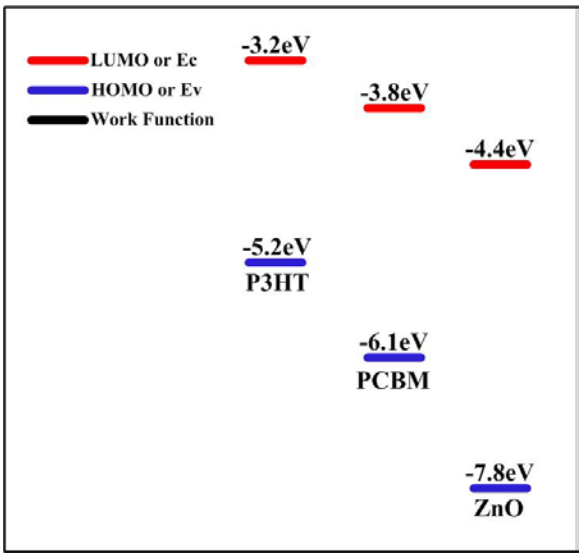


**Figure 6.11** Schematic of energy band structure of P3HT, PCBM and ZnO.

Figure 6.12 is Scanning Electron Microscopy (SEM) of ZnO nanowires as prepared (Figure 6.12a) and coated on P3HT/PCBM (Figure 6.12b). The length is about 2um and width is about hundreds nanometer. It is necessary to mention that the size of ZnO nanowires is not uniform. The KPFM of ZnO nanowires on P3HT/PCBM is shown in Figure 6.13. From the topography (a), the length is about 2um and width is about 150nm, which is in coincident with SEM image. Comparing the SP image in the dark (b) and under illumination (c), it is clear that

photoexcited electrons are present in ZnO nanowires after photo absorption by the active layer because ZnO is a well-known acceptor material as indicated in Figure 6.11.

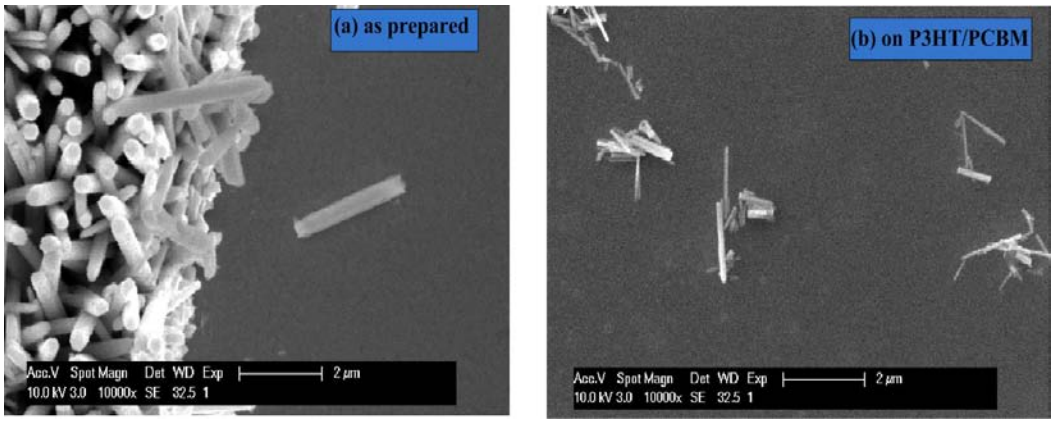


**Figure 6.12** SEM image of vertical ZnO nanowires on substrate as prepared (a) and on P3HT/PCBM active layer (b).

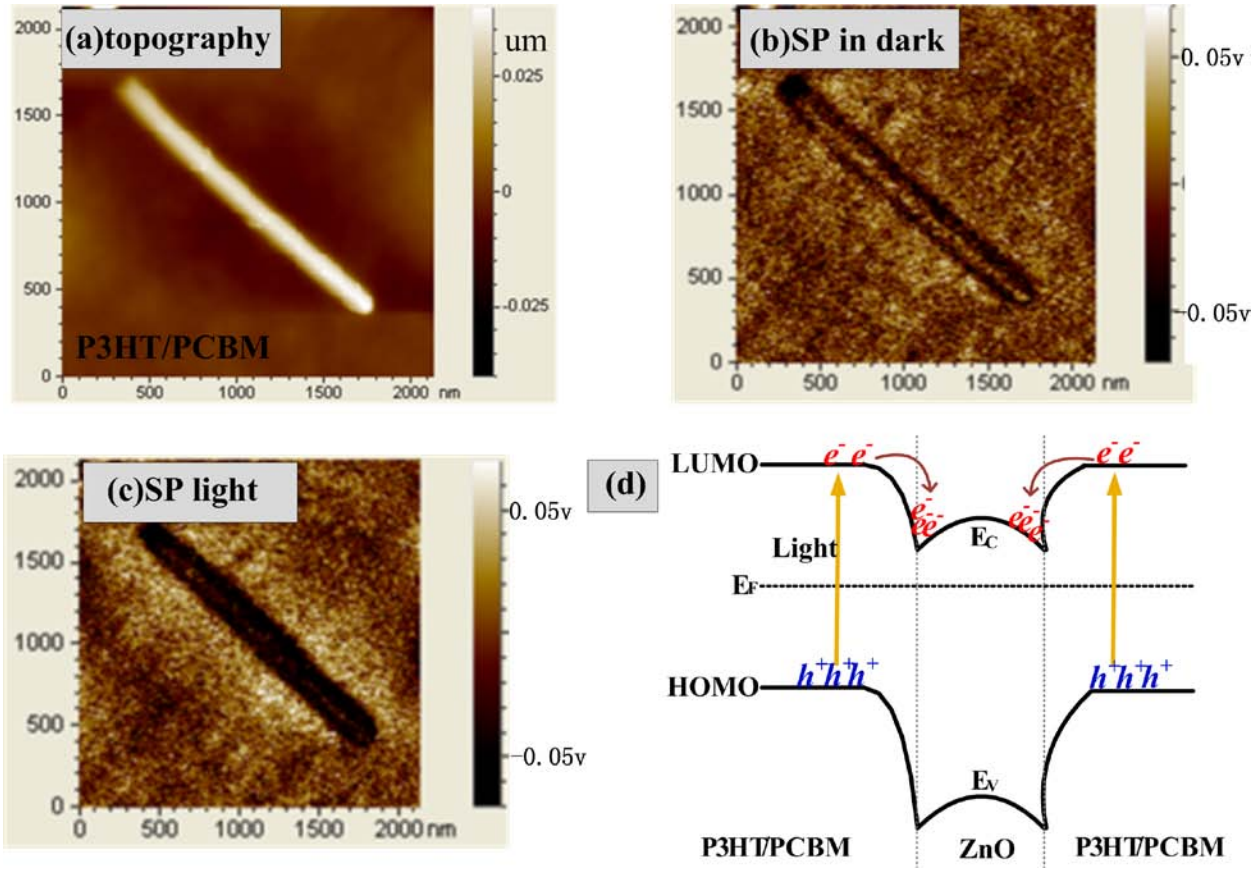


**Figure 6.13** The KPFM of ZnO nanowire on P3HT/PCBM. (a) topography, (b) SP image in the dark, (c) SP image under illumination. (d) Band schematic diagram to show type II heterojunction between P3HT/PCBM and ZnO nanowires.

## 6.5 SUMMARY

The electrical role of SWCNTs in P3HT/PCBM OSCs has been experimentally investigated by KPFM. By comparing the surface potential contrast between SWCNTs and active layers in the dark and under illumination, it is confirmed that SWCNTs are donor materials to transport photoexcited holes. This microscopic observation is in coincidence with the macroscopic results

that introducing of SWCNTs is able to balance the carrier transport between electron and holes and hence improve the performance of OSCs. It is necessary to point out that the cross talk between surface potential signal and topography signal should be minimized in the single-scan mode KPFM.

# 7.0 CONCLUSION AND FUTURE WORK

## 7.1 MAJOR ACCOMPLISHMENTS

This Ph.D dissertation is focused on both theoretical modeling/simulation and experimental characterization of BHJ OSCs to optimize their performance. The major accomplishments are listed as follows:

**1.** After numerically solving the coupled Poisson and Continuity equations by Gummel iteration, we have successfully developed the simulation tool to predict the operation of BHJ OSCs (*J-V* curves).

**2.** Then, the recombination loss has been investigated by simulating intensity dependent *J-V* curves for both annealed and non-annealed P3HT/PCBM cells. It is found that instead of bimolecular recombination, monomolecular recombination dominates the performance of BHJ OSCs.

**3.** Based on the developed simulation tool and the determined loss mechanism, we have investigated the optimization of OSCs in three different aspects as:

- Thickness optimization. For the thin film device, the interference effect has been considered by optical transfer matrix.
- Lowering bandgap of conjugated polymer. Considering the relative large bandgap of regular conjugated polymer (~2eV), we have theoretically investigated the

effect of lowering bandgap of conjugated polymer and have found that conjugated polymer with low bandgap increased the absorption of infrared light.

- Balancing carrier transport in BHJ OSCs because the fast transport of electrons in acceptor (fullerene) and the slow transport of holes in conjugated polymer result in the space charge, which is detrimental to the carrier extraction.

**4.** As for experiments, considering the slow carrier mobility in the disordered organic materials, we have introduced SWCNTs in the active layer to increase carrier mobility. It is observed that small portion of SWCNTs improve the performance but large portion of SWCNTs is detrimental. The investigation on *J*-*V* curves, both under illumination and in the dark, have proved that the improved performance in P3HT/PCBM/SWCNTs device is attributed to the increased carrier mobility as the semiconducting SWCNTs provide ballistic pathways for carriers directly to the electrodes in contrast to the normal hopping conduction in the disordered organic devices. However, for OSCs with large concentration of SWCNTs, metallic SWCNTs cause electron-hole pair recombination, and as a result degrade the device performance.

**5.** The electrical role of SWCNTs in OSCs is locally investigated by scanning Kelvin Probe Force Microscopy. By comparing the surface potential (SP) contrast between dark and illumination, it is concluded that instead of acceptor, SWCNTs work as donor materials to transport photoexcited holes.

## 7.2 FUTURE WORK

### 7.2.1 Determination of Boundary Condition by KPFM

The determination of boundary condition is critical to solve the coupled Poisson and continuity equations and to predict the behavior of OSCs. An ohmic contact at both electrodes is always assumed as in Chapter 2. Under this approximation, $V_{oc}$ is mainly determined by the difference between HOMO of the donor and LUMO of the acceptor [34]. However, it is realized that not only the energy band structure of donor/acceptor, but also the interface between the active layer and electrodes affect $V_{oc}$ of OSCs [96, 97]. Even for ohmic contact, there is still a voltage drop at the interface between the active layer and electrodes due to the band bending [98]. Therefore, it is desirable to precisely determine the boundary condition through direct measurement of the interface potential.

KPFM is a good candidate to serve this purpose. Using single scan mode KPFM, we have identified the electrical role of SWCNT in OSCs as a donor material in Chapter 6. In the future, KPFM can be used to investigate the boundary condition between the active layer and the electrodes as shown in Figure 7.1. The difficulty of this future work is to flatten the cross-section of the device. There are two possible methods to prepare such sample: (1) breaking a device to expose the cross-section and then followed by polishing; (2) directly cutting a device to expose the cross-section. The latter method is the same as in preparation of TEM samples but, in this device, the ITO has to be on a plastic surface instead of glass. Using the measurement data from KPFM, we can obtain the correct boundary condition for our simulation study and further to optimize the performance of OSCs.

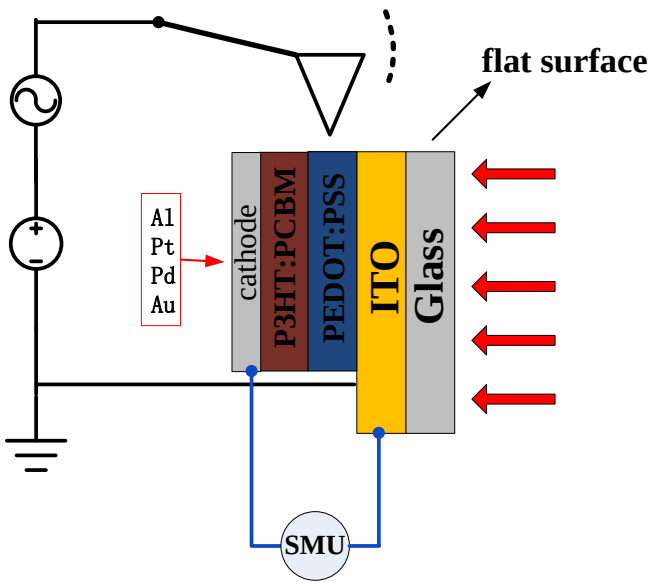


**Figure 7.1** Schematic diagram to show the investigation of boundary condition of OSCs by KPFM.

### 7.2.2 Nanomorphology Investigation by Monte-Carlo Simulation

As discussed in Section 3.3, nanomorphology is strongly related to the macroscopic parameters such as carrier mobility, effective bandgap and generalized Einstein relation. In the future, the simulation tool can be significantly improved by combining the Monte-Carlo simulation with the device modeling (Poisson and continuity equations). Monte-Carlo simulation will relate macroscopic parameters with the nanomorphology. Then, these morphology-related parameters will be considered in the device modeling. In this way, it is able to predict the best morphology to optimize the performance of OSCs.

After determination of the boundary condition by KPFM (Section 7.2.1) and investigation of nanomorphology by Monte-Carlo simulation (Section 7.2.2), the comprehensive

simulation tool is able to optimize the performance of OSCs regarding the thickness of active layer, the electrode/buffer materials, and the nanomorphology as shown in Figure 7.2.

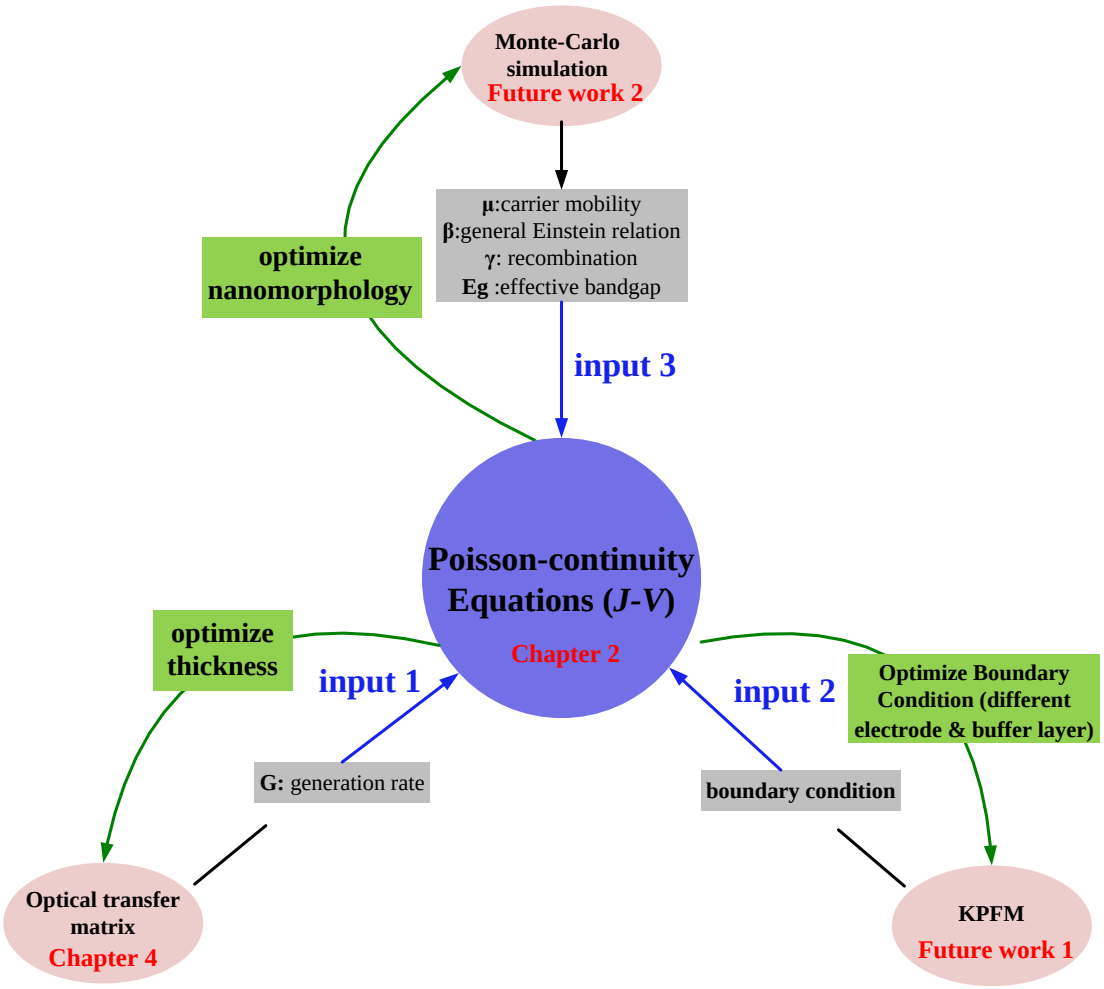


**Figure 7.2** The schematic diagram showing comprehensive simulation tool to optimize the performance of OSCs.

### 7.2.3 Corrugated Surface

It has been theoretically proved that V-shape active layer can increase the light absorption [99]. In the future, we want to manipulate the flat active layer to corrugated shape as shown in Figure 7.3. There are mainly two advantages of this configuration: First, light absorption is enhanced because light bounces back and forth many times in the active layer; Second, the carrier extraction is improved because carrier transport length $L_t$ is smaller than the light absorption length $L_a$ as shown in Figure 7.3.

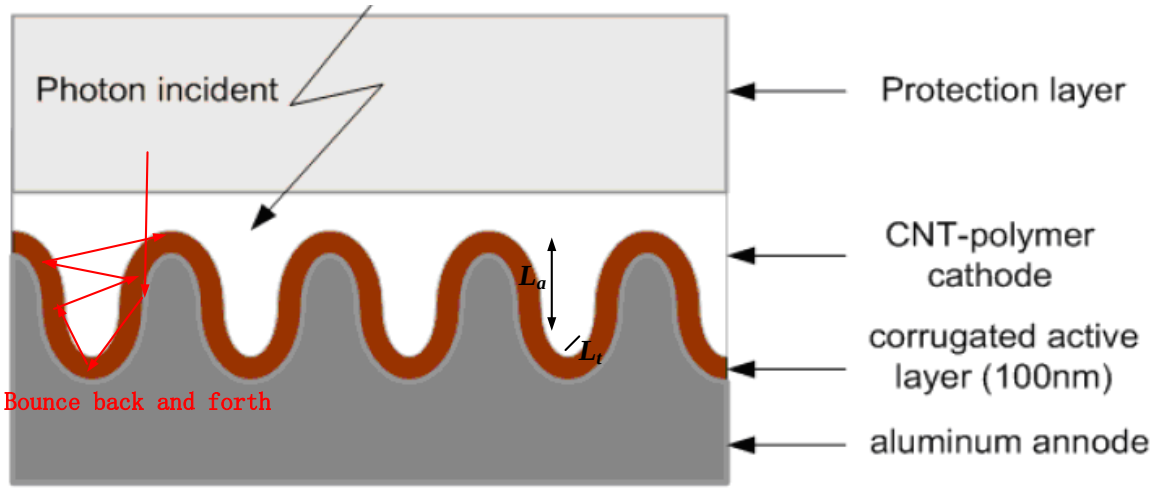


**Figure 7.3** Schematic of the proposed corrugated surface to enhance light absorption and to improve carrier transport.

We investigated OSCs with corrugated configuration and the simulation results are shown in Figure 7.4. For the device with corrugated surface (blue curve), the transport length $L_t$ is fixed at 80nm and x axis (thickness) represents absorption length $L_a$. It is clear that for the

device with corrugated surface, with the increase of absorption length $L_a$, PCE also increases due to the increased light absorption and fixed carrier loss arising from the fixed transport length $L_t$ at 80nm.

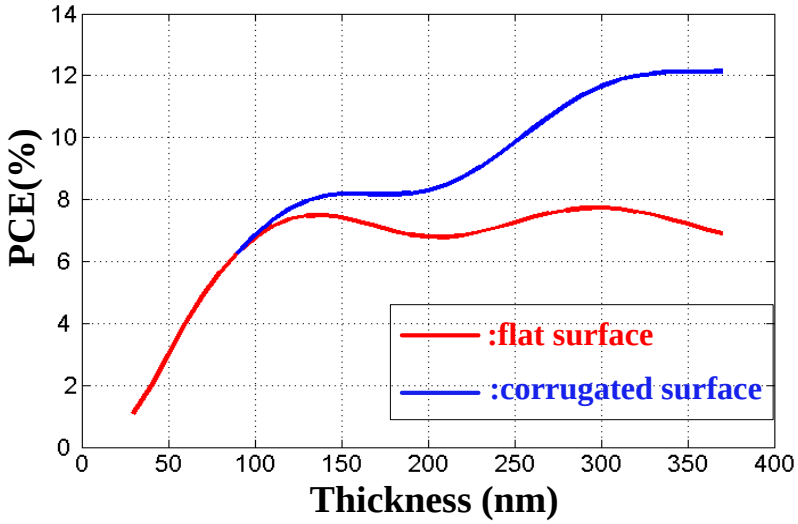


**Figure 7.4** Simulation of thickness dependent PCE for OSCs with flat surface (red curve) and with corrugated surface (blue curve).

Even though OSCs is still not commercially available due to some disadvantages such as low PCE and short lifetime, it is still promising to generate green electricity at lower cost compared with silicon based solar cells and thereby help to preserve our environment in the near future. We believe the contribution of this Ph.D dissertation and the success of our future work will provide major advancement down the road for commercialization of OSCs.

# APPENDIX A

## INTENSITY DEPENDENT PHOTOCURRENT

In the following, we will prove the statement in Section 3.2: When monomolecular recombination is negligible, $\alpha$ equals one when bimolecular recombination loss is much smaller compared with the carrier extraction. With the increase of bimolecular recombination, $\alpha$ monotonically decreases from one.

If bimolecular recombination dominates, Eq. 3.9 can be expressed as

$$G = r_b \cdot n^2 + P \cdot n . \qquad \textbf{A1}$$

$$\frac{d(\ln n)}{d(\ln G)} = \frac{G/n}{dG/dn} = \frac{r_b \cdot n + P}{2r_b \cdot n + P} \equiv \alpha . \qquad \textbf{A2}$$

Solving the differential equation Eq.A2, it is obtained that

$$\ln(n) = \alpha \cdot \ln(G) + c_0 \Rightarrow n = \exp(c_0) \cdot G^{\alpha} = c_1 \cdot G^{\alpha} , \qquad \textbf{A3}$$

in which, $c_0$ $c_1$ are constant with $\exp(c_0)=c_1$. Because photocurrent $J_{ph}$ is proportional to carrier density $n$ and generation rate $G$ is proportional to light intensity $I$, it is derived that:

$$J_{ph} \propto I^{\alpha} , \qquad \textbf{A4}$$

in which, $\alpha$ was defined in Eq.A2 as:

$$\alpha \equiv \frac{r_b \cdot n + P}{2r_b \cdot n + P} = \frac{(r_b \cdot n / P) + 1}{2(r_b \cdot n / P) + 1}. \qquad \textbf{A5}$$

Therefore, $\alpha$ is a monotonic function of $r_b \cdot n / P$. If bimolecular recombination loss is negligible compared with carrier extraction ($r_b \cdot n^2 << P \cdot n$), $\alpha$ equals one. With the increase of bimolecular recombination rate, $\alpha$ monotonically decreases from the unit, which is in coincident with the simulation results in Figure 3.5.

## APPENDIX B

## EINSTEIN RELATION

Einstein relation only for electrons is discussed in this appendix. Einstein relation for holes can be similarly investigated and therefore it will not be mentioned here.

In order to derive Einstein relation in the ordered solid-state materials, let us first look at Eq.2.6, which is

$$J_n = -qn(x)\mu_n * \partial\varphi(x)/\partial x + qD_n * \partial n(x)/\partial x \ . \qquad \textbf{B1}$$

At equilibrium: $J_n$=0 $\rightarrow$ $D_n/\mu_n = -nF/(dn/dx)$, **B2**

electric field: $F = -\partial\varphi(x)/\partial x$

Electron is Fermion with spin 1/2, which obeys Fermi-Dirac statistics as:

$$n(E) = \frac{1}{1+\exp(\frac{E-E_F}{kT})} \qquad \textbf{B3}$$

in which *n(E)* is the possibility of electron to occupy the energy level *E*, $E_F$ is Fermi energy, *kT* is thermal energy. If materials are not extremely heavy doped for the non-degenerated situation, Boltzmann approximation is a good approximation of Fermi-Dirac statistics (Eq.B3). The Boltzmann distribution can be expressed as:

$$n(E) = \exp(\frac{E_F - E}{kT}) \ . \qquad \textbf{B4}$$

Therefore, the electron density of solid state materials at position *x* is:

$$n(x) = \int_{Ec}^{\infty} g(E) * \exp(\frac{E_F - E}{kT}) dE = N_C \exp(\frac{E_c(x) - E_f}{kT}) \ . \qquad \textbf{B5}$$

in which, $g(E) \propto (E\text{-}E_c)^{1/2}$

Combing Eq. B2 and B5, we can get:

$$D_n / \mu_n = -nF / (dn / dx) = \frac{-nF}{n * \partial E_c(x) / \partial x} * kT = kT / q \ . \qquad \textbf{B6}$$

This is classical Einstein relation for solid-state materials in the non-degenerated situation. However, Eq.B5 is invalid for disordered materials because the DOE is Gaussian distribution, which can be expressed as:

$$g(E) \propto (1/\sigma) * \exp(-E^2 / 2\sigma^2) \qquad \textbf{B7}$$

Combining Eq.B2, B4 and B7, the generalized Einstein relation for disordered materials can be expressed as [35]:

$$D_n / \mu_n = \beta * (kT / q) \ , \qquad \textbf{B8}$$

in which $\beta(\sigma)$ is a parameter related to the degree of disorder ($\sigma$) in the OSCs. $\beta$ can be expressed as [35]:

$$\beta(\sigma) = \frac{\int_{-\infty}^{\infty} \exp\left[-\left(\frac{E - E_0}{\sigma}\right)^2\right] * \frac{1}{1 + \exp(E - \varepsilon)} dE}{\int_{-\infty}^{\infty} \exp\left[-\left(\frac{E - E_0}{\sigma}\right)^2\right] * \frac{\exp(E - \varepsilon)}{[1 + \exp(E - \varepsilon)]^2} dE} \qquad \textbf{B9}$$

## BIBLIOGRAPHY


[1] J. Houghton, Global warming, *Reports on Progress in Physics* **68**, 1343-1403 (2005).

[2] P. W. M. Blom, V. D. Mihailetchi, L. J. A. Koster, and D. E. Markov, Device physics of polymer : fullerene bulk heterojunction solar cells, *Advanced Materials* **19**, 1551-1566 (2007).

[3] A. E. Becquerel, *C. R. Acad. Sci* **9**, 145 (1839).

[4] D. M. Chapin, C. S. Fuller, and G. L. Pearson, A New Silicon p-n Junction Photocell for Converting Solar Radiation into Electrical Power, *Journal of Applied Physics* **25**, 676-677 (1954).

[5] J. Zhao, A. Wang, M. A. Green, and F. Ferrazza, 19.8% efficient ``honeycomb'' textured multicrystalline and 24.4% monocrystalline silicon solar cells, *Applied Physics Letters* **73**, 1991-1993 (1998).

[6] W. Shockley and H. J. Queisser, Detailed Balance Limit of Efficiency of p-n Junction Solar Cells, *Journal of Applied Physics* **32**, 510-519 (1961).

[7] M. A. Green, K. Emery, Y. Hisikawa, and W. Warta, Solar cell efficiency tables (Version 30), *Progress in Photovoltaics* **15**, 425-430 (2007).

[8] K. A. Bertness, R. K. Sarah, D. J. Friedman, A. E. Kibbler, C. Kramer, and J. M. Olson, 29.5%-efficient GaInP/GaAs tandem solar cells, *Applied Physics Letters* **65**, 989-991 (1994).

[9] G. F. Nenmark, Defects in wide band gap II-VI crystals, *Materials Sciences and Engineering* **21**, 1-46 (1997).

[10] A. Shah, P. Torres, R. Tscharner, N. Wyrsch, and H. Keppner, Photovoltaic technology: The case for thin-film solar cells, *Science* **285**, 692-698 (1999).

[11] B. Jayesh and Y. Yang, Polymer electroluminescent devices processed by inkjet printing: I. Polymer light-emitting logo, *Applied Physics Letters* **72**, 2660-2662 (1998).

[12] S. S. Kim, S. I. Na, J. Jo, G. Tae, and D. Y. Kim, Efficient polymer solar cells fabricated by simple brush painting, *Advanced Materials* **19**, 4410-4415 (2007).

[13] V. Doojin, K. Seok-Soon, J. Jang, O. Seung-Hwan, N. Seok-In, K. Juhwan, and K. Dong-Yu, Fabrication of organic bulk heterojunction solar cells by a spray deposition method for low-cost power generation, *Applied Physics Letters* **91**, 81102-81104 (2007).

[14] H. Kallmann and M. Pope, Photovoltaic Effect in Organic Crystals, *The Journal of Chemical Physics* **30**, 585-586 (1959).

[15] C. W. Tang, Two-layer organic photovoltaic cell, *Applied Physics Letters* **48**, 183-185 (1986).

[16] G. Yu, J. Gao, J. C. Hummelen, F. Wudl, and A. J. Heeger, Polymer Photovoltaic Cells: Enhanced Efficiencies via a Network of Internal Donor-Acceptor Heterojunctions, *Science* **270**, 1789-1791 (1995).

[17] W. L. Ma, C. Y. Yang, X. Gong, K. Lee, and A. J. Heeger, Thermally stable, efficient polymer solar cells with nanoscale control of the interpenetrating network morphology, *Advanced Functional Materials* **15**, 1617-1622 (2005).

[18] G. Li, V. Shrotriya, J. Huang, Y. Yao, T. Moriarty, K. Emery, and Y. Yang, High-efficiency solution processable polymer photovoltaic cells by self-organization of polymer blends, *Nat Mater* **4**, 864-868 (2005).

[19] J. Y. Kim, K. Lee, N. E. Coates, D. Moses, T.-Q. Nguyen, M. Dante, and A. J. Heeger, Efficient Tandem Polymer Solar Cells Fabricated by All-Solution Processing, *Science* **317**, 222-225 (2007).

[20] N. Blouin, A. Michaud, and M. Leclerc, A low-bandgap poly(2,7-carbazole) derivative for use in high-performance solar cells, *Advanced Materials* **19**, 2295-2300 (2007).

[21] D. Muhlbacher, M. Scharber, M. Morana, Z. G. Zhu, D. Waller, R. Gaudiana, and C. Brabec, High photovoltaic performance of a low-bandgap polymer, *Advanced Materials* **18**, 2884-2889 (2006).

[22] C. K. Chiang, C. R. Fincher, Y. W. Park, A. J. Heeger, H. Shirakawa, E. J. Louis, S. C. Gau, and A. G. MacDiarmid, Electrical Conductivity in Doped Polyacetylene, *Physical Review Letters* **39**, 1098 (1977).

[23] J. H. Burroughes, D. D. C. Bradley, A. R. Brown, R. N. Marks, K. Mackay, R. H. Friend, P. L. Burns, and A. B. Holmes, Light-emitting diodes based on conjugated polymers, *Nature* **347**, 539-541 (1990).

[24] B. A. Gregg and M. C. Hanna, Comparing organic to inorganic photovoltaic cells: Theory, experiment, and simulation, *Journal of Applied Physics* **93**, 3605-3614 (2003).

[25] C. J. Brabec, N. S. Sariciftci, and J. C. Hummelen, Plastic solar cells, *Advanced Functional Materials* **11**, 15-26 (2001).

[26] A. Pivrikas, N. S. Sariciftci, G. Juska, and R. Osterbacka, A review of charge transport and recombination in polymer/fullerene organic solar cells, *Progress in Photovoltaics* **15**, 677-696 (2007).

[27] K. M. Coakley and M. D. McGehee, Conjugated Polymer Photovoltaic Cells, *Chem. Mater.* **16**, 4533-4542 (2004).

[28] S. H. Park, A. Roy, S. Beaupre, S. Cho, N. Coates, J. S. Moon, D. Moses, M. Leclerc, K. Lee, and A. J. Heeger, Bulk heterojunction solar cells with internal quantum efficiency approaching 100%, *Nat Photon* **3**, 297-302 (2009).

[29] L. J. A. Koster, E. C. P. Smits, V. D. Mihailetchi, and P. W. M. Blom, Device model for the operation of polymer/fullerene bulk heterojunction solar cells, *Physical Review B* **72**, 085205 (2005).

[30] S.M.SZE, *Physics of Semiconductor Devices*, 1981.

[31] V. D. Mihailetchi, L. J. A. Koster, J. C. Hummelen, and P. W. M. Blom, Photocurrent generation in polymer-fullerene bulk heterojunctions, *Physical Review Letters* **93**, 216601 (2004).

[32] V. D. Mihailetchi, H. X. Xie, B. de Boer, L. J. A. Koster, and P. W. M. Blom, Charge transport and photocurrent generation in poly (3-hexylthiophene): Methanofullerene bulk-heterojunction solar cells, *Advanced Functional Materials* **16**, 699-708 (2006).

[33] X. Yang, J. Loos, S. C. Veenstra, W. J. H. Verhees, M. M. Wienk, J. M. Kroon, M. A. J. Michels, and R. A. J. Janssen, Nanoscale Morphology of High-Performance Polymer Solar Cells, *Nano Letters* **5**, 579-583 (2005).

[34] C. J. Brabec, A. Cravino, D. Meissner, N. S. Sariciftci, T. Fromherz, M. T. Rispens, L. Sanchez, and J. C. Hummelen, Origin of the open circuit voltage of plastic solar cells, *Advanced Functional Materials* **11**, 374-380 (2001).

[35] Y. Roichman and N. Tessler, Generalized Einstein relation for disordered semiconductors---implications for device performance, *Applied Physics Letters* **80**, 1948-1950 (2002).

[36] K. Maturova, S. S. van Bavel, M. M. Wienk, R. A. J. Janssen, and M. Kemerink, Morphological Device Model for Organic Bulk Heterojunction Solar Cells, *Nano Letters* **9**, 3032-3037 (2009).

[37] H. K. Gummel, A self-consistent iterative scheme for one-dimensional steady state transistor calculations, *Electron Devices, IEEE Transactions on* **11**, 455-465 (1964).

[38] D. L. Scharfetter and H. K. Gummel, Large-signal analysis of a silicon Read diode oscillator, *Electron Devices, IEEE Transactions on* **16**, 64-77 (1969).

[39] A. M. Winslow, Numerical solution of the quasilinear poisson equation in a nonuniform triangle mesh, *Journal of Computational Physics* **1**, 149-172 (1966).

[40] D. W. Sievers, V. Shrotriya, and Y. Yang, Modeling optical effects and thickness dependent current in polymer bulk-heterojunction solar cells, *Journal of Applied Physics* **100**, 114509-7 (2006).

[41] T. M. Clarke and J. R. Durrant, Charge Photogeneration in Organic Solar Cells, *Chemical Reviews* **110**, 6736-6767 (2010).

[42] L. J. A. Koster, V. D. Mihailetchi, and P. W. M. Blom, Bimolecular recombination in polymer/fullerene bulk heterojunction solar cells, *Applied Physics Letters* **88**, 52104-52106 (2006).

[43] R. A. Street, Carrier mobility, structural order, and solar cell efficiency of organic heterojunction devices, *Applied Physics Letters* **93**, 133308-133311 (2008).

[44] M. Hallermann, E. Da Como, J. Feldmann, M. Izquierdo, S. Filippone, N. Martin, S. Juchter, and E. von Hauff, Correlation between charge transfer exciton recombination and photocurrent in polymer/fullerene solar cells, *Applied Physics Letters* **97**, 23301-23303 (2010).

[45] R. A. Street and M. Schoendorf, Interface state recombination in organic solar cells, *Physical Review B* **81**, 205307 (2010).

[46] L. Onsager, Initial Recombination of Ions, *Physical Review* **54**, 554 (1938).

[47] C. L. Braun, Electric field assisted dissociation of charge transfer states as a mechanism of photocarrier production, *The Journal of Chemical Physics* **80**, 4157-4161 (1984).

[48] C. Deibel, A. Wagenpfahl, and V. Dyakonov, Origin of reduced polaron recombination in organic semiconductor devices, *Physical Review B* **80**, 075203 (2009).

[49] G. J. Adriaenssens and V. I. Arkhipov, Non-Langevin recombination in disordered materials with random potential distributions, *Solid State Communications* **103**, 541-543 (1997).

[50] A. Pivrikas, G. Juska, A. J. Mozer, M. Scharber, K. Arlauskas, N. S. Sariciftci, H. Stubb, and R. Osterbacka, Bimolecular Recombination Coefficient as a Sensitive Testing

Parameter for Low-Mobility Solar-Cell Materials, *Physical Review Letters* **94**, 176806 (2005).

[51] M. M. Mandoc, L. J. A. Koster, and P. W. M. Blom, Optimum charge carrier mobility in organic solar cells, *Applied Physics Letters* **90**, 133504-133506 (2007).

[52] L. Liu, W. E. Stanchina, and G. Li, Effects of semiconducting and metallic single-walled carbon nanotubes on performance of bulk heterojunction organic solar cells, *Applied Physics Letters* **94**, 233309-233311 (2009).

[53] W. U. Huynh, J. J. Dittmer, N. Teclemariam, D. J. Milliron, A. P. Alivisatos, and K. W. J. Barnham, Charge transport in hybrid nanorod-polymer composite photovoltaic cells, *Physical Review B* **67**, 115326 (2003).

[54] J. K. J. van Duren, X. N. Yang, J. Loos, C. W. T. Bulle-Lieuwma, A. B. Sieval, J. C. Hummelen, and R. A. J. Janssen, Relating the morphology of poly(p-phenylene vinylene)/methanofullerene blends to solar-cell performance, *Advanced Functional Materials* **14**, 425-434 (2004).

[55] C. Deibel and A. Wagenpfahl, Comment on "Interface state recombination in organic solar cells", *Physical Review B* **82**, 207301 (2010).

[56] R. A. Street, Reply to "Comment on `Interface state recombination in organic solar cells' ", *Physical Review B* **82**, 207302 (2010).

[57] L. J. A. Koster, V. D. Mihailetchi, and P. W. M. Blom, Ultimate efficiency of polymer/fullerene bulk heterojunction solar cells, *Applied Physics Letters* **88**, 93511-93513 (2006).

[58] C. G. Shuttle, B. ORegan, A. M. Ballantyne, J. Nelson, D. D. C. Bradley, and J. R. Durrant, Bimolecular recombination losses in polythiophene: Fullerene solar cells, *Physical Review B* **78**, 113201 (2008).

[59] Q. Gu, E. A. Schiff, S. Grebner, F. Wang, and R. Schwarz, Non-Gaussian Transport Measurements and the Einstein Relation in Amorphous Silicon, *Physical Review Letters* **76**, 3196 (1996).

[60] S. V. Rakhmanova and E. M. Conwell, Mobility variation with field in conducting polymer films, *Synthetic Metals* **116**, 389-391 (2001).

[61] H. Bassler, Charge Transport in Disordered Organic Photoconductors - a Monte-Carlo Simulation Study, *Physica Status Solidi B-Basic Research* **175**, 15-56 (1993).

[62] C. Groves, R. A. Marsh, and N. C. Greenham, Monte Carlo modeling of geminate recombination in polymer-polymer photovoltaic devices, *The Journal of Chemical Physics* **129**, 114903 (2008).

[63] P. Schilinsky, C. Waldauf, and C. J. Brabec, Recombination and loss analysis in polythiophene based bulk heterojunction photodetectors, *Applied Physics Letters* **81**, 3885-3887 (2002).

[64] L. A. A. Pettersson, L. S. Roman, and O. Inganas, Modeling photocurrent action spectra of photovoltaic devices based on organic thin films, *Journal of Applied Physics* **86**, 487-496 (1999).

[65] http://rredc.nrel.gov/solar/spectra/, (2000).

[66] Y. M. Nam, J. Huh, and W. H. Jo, Optimization of thickness and morphology of active layer for high performance of bulk-heterojunction organic solar cells, *Solar Energy Materials and Solar Cells* **94**, 1118-1124 (2010).

[67] V. D. Mihailetchi, H. X. Xie, B. de Boer, L. M. Popescu, J. C. Hummelen, P. W. M. Blom, and L. J. A. Koster, Origin of the enhanced performance in poly(3-hexylthiophene): [6,6]-phenyl C-61-butyric acid methyl ester solar cells upon slow drying of the active layer, *Applied Physics Letters* **89**, 12107-12109 (2006).

[68] M. Lenes, M. Morana, C. J. Brabec, and P. W. M. Blom, Recombination-Limited Photocurrents in Low Bandgap Polymer/Fullerene Solar Cells, *Advanced Functional Materials* **19**, 1106-1111 (2009).

[69] D. J. D. Moet, M. Lenes, M. Morana, H. Azimi, C. J. Brabec, and P. W. M. Blom, Enhanced dissociation of charge-transfer states in narrow band gap polymer:fullerene solar cells processed with 1,8-octanedithiol, *Applied Physics Letters* **96**, 213506-213508 (2010).

[70] J. Peet, J. Y. Kim, N. E. Coates, W. L. Ma, D. Moses, A. J. Heeger, and G. C. Bazan, Efficiency enhancement in low-bandgap polymer solar cells by processing with alkane dithiols, *Nature Materials* **6**, 497-500 (2007).

[71] M. S. Strano, C. A. Dyke, M. L. Usrey, P. W. Barone, M. J. Allen, H. Shan, C. Kittrell, R. H. Hauge, J. M. Tour, and R. E. Smalley, Electronic Structure Control of Single-Walled Carbon Nanotube Functionalization, *Science* **301**, 1519-1522 (2003).

[72] K. C. Kao and W. Hwang, *Electrical transport in solids with particular reference to organic semiconductors*, vol. 14: Pergamon Press, 1970.

[73] M. G. Alvin and R. Albert, Double Extraction of Uniformly Generated Electron-Hole Pairs from Insulators with Noninjecting Contacts, *Journal of Applied Physics* **42**, 2823-2830 (1971).

[74] V. D. Mihailetchi, J. Wildeman, and P. W. M. Blom, Space-charge limited photocurrent, *Physical Review Letters* **94**, 126602 (2005).

[75] C. Waldauf, M. C. Scharber, P. Schilinsky, J. A. Hauch, and C. J. Brabec, Physics of organic bulk heterojunction devices for photovoltaic applications, *Journal of Applied Physics* **99**, 104503 (2006).

[76] C. Li, Y. H. Chen, Y. B. Wang, Z. Iqbal, M. Chhowalla, and S. Mitra, A fullerene-single wall carbon nanotube complex for polymer bulk heterojunction photovoltaic cells, *Journal of Materials Chemistry* **17**, 2406-2411 (2007).

[77] S. Berson, R. de Bettignies, S. Bailly, S. Guillerez, and B. Jousselme, Elaboration of P3HT/CNT/PCBM composites for organic photovoltaic cells, *Advanced Functional Materials* **17**, 3363-3370 (2007).

[78] E. Kymakis and G. A. J. Amaratunga, Single-wall carbon nanotube/conjugated polymer photovoltaic devices, *Applied Physics Letters* **80**, 112-114 (2002).

[79] M.-C. Wu, Y.-Y. Lin, S. Chen, H.-C. Liao, Y.-J. Wu, C.-W. Chen, Y.-F. Chen, and W.-F. Su, Enhancing light absorption and carrier transport of P3HT by doping multi-wall carbon nanotubes, *Chemical Physics Letters* **468**, 64-68 (2009).

[80] S. Chaudhary, H. Lu, A. M. Muller, C. J. Bardeen, and M. Ozkan, Hierarchical Placement and Associated Optoelectronic Impact of Carbon Nanotubes in Polymer-Fullerene Solar Cells, *Nano Letters* **7**, 1973-1979 (2007).

[81] V. Palermo, M. Palma, and P. Samor, Electronic Characterization of Organic Thin Films by Kelvin Probe Force Microscopy, *Advanced Materials* **18**, 145-164 (2006).

[82] G. Binnig, C. F. Quate, and C. Gerber, Atomic Force Microscope, *Physical Review Letters* **56**, 930 (1986).

[83] A. Olbrich, B. Ebersberger, and C. Boit, Conducting atomic force microscopy for nanoscale electrical characterization of thin $SiO_2$, *Applied Physics Letters* **73**, 3114-3116 (1998).

[84] P. Girard, Electrostatic force microscopy: principles and some applications to semiconductors, *Nanotechnology* **12**, 485-490 (2001).

[85] R. C. Barrett and C. F. Quate, Charge storage in a nitride-oxide-silicon medium by scanning capacitance microscopy, *Journal of Applied Physics* **70**, 2725-2733 (1991).

[86] C. Shafai, D. J. Thomson, M. Simard-Normandin, G. Mattiussi, and P. J. Scanlon, Delineation of semiconductor doping by scanning resistance microscopy, *Applied Physics Letters* **64**, 342-344 (1994).

[87] M. Nonnenmacher, M. P. O'Boyle, and H. K. Wickramasinghe, Kelvin probe force microscopy, *Applied Physics Letters* **58**, 2921-2923 (1991).

[88] S. C. P. Liam, G. R. Obadiah, and S. G. David, Electrical Scanning Probe Microscopy on Active Organic Electronic Devices, *Advanced Materials* **21**, 19-28 (2009).

[89] M. Chiesa, L. Burgi, J.-S. Kim, R. Shikler, R. H. Friend, and H. Sirringhaus, Correlation between Surface Photovoltage and Blend Morphology in Polyfluorene-Based Photodiodes, *Nano Letters* **5**, 559-563 (2005).

[90] D. Brunel, D. Deresmes, and T. Melin, Determination of the electrostatic lever arm of carbon nanotube field effect transistors using Kelvin force microscopy, *Applied Physics Letters* **94**, 223508-223510 (2009).

[91] L. Liu and G. Li, Electrical characterization of single-walled carbon nanotubes in organic solar cells by Kelvin probe force microscopy, *Applied Physics Letters* **96**, 83302-83304 (2010).

[92] H. Hoppe, T. Glatzel, M. Niggemann, A. Hinsch, M. C. Lux-Steiner, and N. S. Sariciftci, Kelvin Probe Force Microscopy Study on Conjugated Polymer/Fullerene Bulk Heterojunction Organic Solar Cells, *Nano Letters* **5**, 269-274 (2005).

[93] K. Maturova, M. Kemerink, M. M. Wienk, D. S. H. Charrier, and R. A. J. Janssen, Scanning Kelvin Probe Microscopy on Bulk Heterojunction Polymer Blends, *Advanced Functional Materials* **19**, 1379-1386 (2009).

[94] H. O. Jacobs, P. Leuchtmann, O. J. Homan, and A. Stemmer, Resolution and contrast in Kelvin probe force microscopy, *Journal of Applied Physics* **84**, 1168-1173 (1998).

[95] C. S. Jiang, H. R. Moutinho, J. F. Geisz, D. J. Friedman, and M. M. Al-Jassim, Direct measurement of electrical potentials in GaInP2 solar cells, *Applied Physics Letters* **81**, 2569-2571 (2002).

[96] V. Coropceanu, J. Cornil, D. A. da Silva, Y. Olivier, R. Silbey, and J. L. Bredas, Charge transport in organic semiconductors, *Chemical Reviews* **107**, 926-952 (2007).

[97] K. Kawano, N. Ito, T. Nishimori, and J. Sakai, Open circuit voltage of stacked bulk heterojunction organic solar cells, *Applied Physics Letters* **88**, 73514-73516 (2006).

[98] V. D. Mihailetchi, P. W. M. Blom, J. C. Hummelen, and M. T. Rispens, Cathode dependence of the open-circuit voltage of polymer:fullerene bulk heterojunction solar cells, *Journal of Applied Physics* **94**, 6849-6854 (2003).

[99] S. B. Rim, S. Zhao, S. R. Scully, M. D. McGehee, and P. Peumans, An effective light trapping configuration for thin-film solar cells, *Applied Physics Letters* **91**, 243501-243503 (2007).